Spring 11-8-2014

Adaptive Concurrent Multiscale Method for Fracture of Material and Size Effect Problem

Mirmohammadreza Kabiri
University of Colorado at Boulder, mmr.kabiri@colorado.edu

Recommended Citation

Kabiri, Mirmohammadreza, "Adaptive Concurrent Multiscale Method for Fracture of Material and Size Effect Problem" (2014). *Civil Engineering Graduate Theses & Dissertations*. 113.
https://scholar.colorado.edu/cven_gradetds/113

Adaptive Concurrent Multiscale Method for Fracture of Material and Size Effect Problem

by

M. Kabiri

B.A., University of Mohaghegh Ardebili, 2007

M.S., University of Tehran, 2009

A thesis submitted to the
Faculty of the Graduate School of the
University of Colorado in partial fulfillment
of the requirements for the degree of
Doctor of Philosophy
Department of Civil, Environmental, and Architectural Engineering
2015

This thesis entitled:
Adaptive Concurrent Multiscale Method for Fracture of Material and Size Effect Problem
written by M. Kabiri
has been approved for the Department of Civil, Environmental, and Architectural Engineering

Prof. Franck J. Vernerey

Prof. Richard Regueiro

Date

The final copy of this thesis has been examined by the signatories, and we find that both the content and the form meet acceptable presentation standards of scholarly work in the above mentioned discipline.

Kabiri, M. (Ph.D., Civil Engineering)

Adaptive Concurrent Multiscale Method for Fracture of Material and Size Effect Problem

Thesis directed by Prof. Franck J. Vernerey

Abstract

An adaptive concurrent multiscale methodology (ACM^2) is introduced to enable strong interaction between both macroscopic and microscopic deformation fields. The method is formulated in finite element framework and is based on the balance between two sources of error, namely, numerical and homogenization errors. In finite element framework, the first type of error dictates element refinement in regions that are characterized by high deformation gradient, to improve the accuracy of numerical solution. In contrary, the second type of error indicates that the refining procedure should not exceed a critical level, that is determined by the size of the unit cell and represents the scale of material's microstructure. The method then aims at embedding unit cells in continuum region and through appropriate boundary conditions couple the deformation field in both regions. Upon this, the method is able to adequately combine different descriptions of material to assure accuracy with low computational cost. We will then show that our computational technique, in conjunction with the extended finite element method, is ideal to study the strong interactions between a macroscopic crack and the microstructure of heterogeneous media. In particular, the method enables an explicit description of micro-structural features near the crack tip, while a computationally inexpensive coarse scale continuum description is used in the rest of the domain. The present work also aim at investigating several examples of crack propagation in materials with random microstructures, and discussing the potential of the multiscale technique in relating microstructural details to material strength and toughness, and capturing the size effect.

Dedication

I would like to dedicate my thesis to my beloved parents, and sisters.

Acknowledgements

First, and foremost, I have to thank my adviser, Prof. Franck J. Vernerey, for his advising on this research; his dedication to my work is very much appreciated and I am continually inspired by his commitment to his research.

I would also like to show my gratitude to Prof. Alireza Doostan, Prof. Richard Regueiro, Prof. Yunping Xi, and Prof. Mark Stoykovich, for serving in my committee. Their suggestions and comments were critical to raise the quality of this work.

I would also like to thank my colleagues and friends at CU Boulder: Mehdi Farsad, Louis, Lan, Heyon, Valentin, Umut, Xavi, Eduard and Natasha for sharing their knowledge and ideas with me. My especial thanks also goes to Amin Mahdavi, Mahdi Soudkhah and Mohammad Hadigol for their extensive supports during my studies at University of Colorado at Boulder.

Most importantly, non of this could have happened without the support of my parents, Mirasadullah Kabiri and Zahra Shafiei, and my sisters, Shervin, Maryam and Mahshid.

Contents

Chapter

Appendix

Figures

Figure

Chapter 1

Introduction

In solid mechanics the size effect problem is defined as the effect of the characteristic size of structure on the mechanical properties and fracture behavior of heterogeneous material, such as material nominal strength, when geometrically similar structures with different sizes are compared. Understanding this problem is crucial for optimized design of large scale structures, such as reinforced structural concrete elements, concrete dams, ships made by composites or even in higher scale geotechnical structures such as tunnels. The size effect was first reported in the pioneering work of Griffith. In [108], Griffith performed several experiments on cylindrical glass specimens and observed that the nominal strength for slender specimens is higher than the nominal strength for bulk specimens. At early stage this problem was related, by scientists, to the stochastic accumulation of defects in the microstructure of glass. Therefore, this problem was considered as a probabilistic problem which is strongly related to the type of distribution of weak-links in the materials microstructure which had to be addressed by statisticians. Numerous studies were then focused on describing the problem using statistical models. The finishing touch of statistical theory of size effect is the work of Weibul in [123, 126, 125, 124]. Based on experimental observation, Weibul concluded that the size effect is highly dependent on the tail distribution of low strength values which is not adequately represented by existing distribution functions. He then proposed the Weibul distribution function to tackle the short coming of standard distribution functions. Although the size effect problem attracted mechanicians later, application of statistical theories for steel and ceramic has continued so far [98, 105, 107].

In general, the size effect problem is known to be a scaling problem which is fundamental to every physical system. In fluid mechanics, the scaling problem can be addressed by power law. For solids, however, the power law fails to predict the size effect due to the presence of characteristic length that is associated with the material microstructure. To explain this, let us consider a structure with characteristic size D. In [104], it is shown that the response of structure (such as nominal strength of material or deflection of a point on the structure), Y, can be written in terms of the size of the structure as $Y = f(D)$. Trivially, for a geometrically similar structure of size D', this function is written as $Y' = f(D')$. Since no characteristic length exists in the definition of response function, the scaling reads:

$$\frac{Y'}{Y} = \frac{f(D')}{f(D)} = f\left(\frac{D'}{D}\right) \tag{1.1}$$

Power law, then proposes that the one and only one solution for this functional equation is:

$$Y = f(D) = (D/c_1)^s \tag{1.2}$$

Where c_1 is a constant that has the unit of a length and s is another constant which is defined based on failure criteria. For example, in elasticity or theory of plasticity the failure of structure is formulated in terms of mechanical parameters, such as failure envelopes based on stress criteria. This means that failure in solid mechanics does not depend on the characteristic size of the structure, $i.e.$ $s = 0$ in (1.2).

Let us now investigate the value of s predicted by linear elastic fracture mechanics (LEFM) theory. In this theory it is assumed that the material is linear, elastic and the size of the fracture process zone (FPZ) in front of the crack is negligible compared to the size of physical domain. Also, the LEFM predicts a singular stress field at the crack tip which is characterized by the stress intensity factor, K. In the literature [109], it is shown that the stress intensity factor can be written as:

$$K = \sigma\sqrt{a\pi}.f(\frac{a}{D}) \tag{1.3}$$

Where σ is the far field stress, a is the crack length, D is the characteristic size of the structure and f is a function which depends on the geometry of specimen and is defined either analytically or numerically. Based on this theory the structure fails when the magnitude of stress intensity factor reaches the material's critical stress intensity factor. Let us now consider two geometrically similar specimens with different characteristic size, W_1 and W_2. Using above formula one can show that $\sigma_2^N/\sigma_1^N = \lambda^{-\frac{1}{2}}$, where $\lambda = D_2/D_1$, that is in (1.2) the unknown power is $s = -\frac{1}{2}$. Variations of $\log(\sigma^N)$ versus $\log(\lambda)$ based plasticity (strength) and LEFM theories are shown in Fig.1.1a, with straight lines. In addition, this figure qualitatively shows the extensive experimental test data reported by Walsh [121, 122]. As shown in this figure when the characteristic size of structure is relatively small, compared to the characteristic length of material's microstructure, the prediction of plasticity theory and experimental test data are in good agreement. LEFM theory, on the other hand, is valid when the structure size is relatively large. Nevertheless, the behavior of material between these to length scales follows a trend that is best described by a smooth transition between the prediction of plasticity and LEFM theories. In [114], Leicester showed that optimum value for s in (1.2) is equal to $\frac{1}{2}$, but his model fits only a certain part of experimental data. To better understand this phenomenon it is helpful to cite a basic idea of nonlinear fracture mechanics. Based on experimental observations a structure fails when a macroscopic crack is formed, due to accumulation of damage at the lower length scales, and started to propagate unstably. In fact, this theory suggests that a fracture process zone (FPZ) exists in front of the propagating crack tip, and its relative size, compared to the characteristic size of the

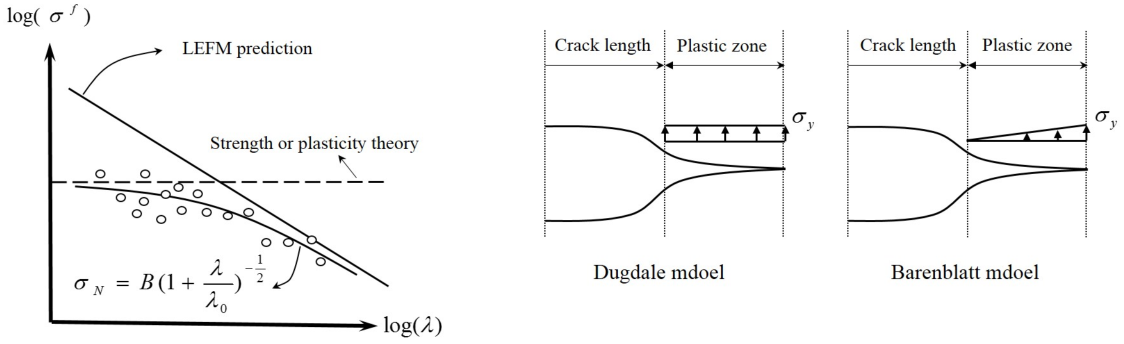

(*a*) (*b*)

Figure 1.1: *(a) Size effect on the nominal stress predicted by LEFM, plasticity and Crack band theory, (b) Dugdale and Barenblatt models used in Hillerborg [117].*

structure, defines the behavior of material.

The nonlinear fracture mechanics, then, assumes that the width of the FPZ is constant and proposes to define the length of the FPZ by equating the stored strain energy and the energy that is released due to the unstable crack propagation. Following this idea, for the first time, Irwin showed that for every material there exists a characteristic length l_0 which is written as:

$$l_0 = \frac{EG_f}{\sigma_0^2} \tag{1.4}$$

where σ_0 is nominal stress, G_f is fracture energy per unit length of crack and E is the elastic modulus. Many theories were then derived based on this concept. For example, Dugdale [106] and Barenblatt [100, 99] formulated two different models inspired by plastic FPZ model. In these models the fracture process zone is replaced by a cohesive crack. The crack is characterized by a stress-displacement relation which defines the acting stress along its faces, and its length can be calculated following the aforementioned concept. Fig. 1.1b, shows the variation of the acting stress along the faces of the cohesive crack, which represents the FPZ, in these models.

Nevertheless, the capstone for modeling the size effect problem was laid by the crack band theory in [112, 113, 115, 103, 102, 101, 104]. The underlying concepts of this method can be explained by understanding the real nature of the fracture of quasi brittle materials. For this we focus on the failure of a structure, that is characterized by a preexisting crack. We also assume this structure is made of normal strength concrete, which is known as a quasi brittle material, and extensively used in real structures (*e.g.* dams). Also the structure is under monotonically increasing loading until it reaches failure. Basically, prior to the failure some micro cracks emerge in the FPZ, in front of the crack, in order to release the stored elastic energy. Also, when the driving force becomes more pronounced existing micro cracks tend to deform, new micro cracks are introduces in this zone, and eventually the micro cracks link and form macro cracks. To represent this procedure, the crack band theory suggests the material in the FPZ follows a bilinear stress-strain behavior with post peak softening, as shown in Fig. 1.2a, while material elsewhere is linear elastic. Then, assuming the width of FPZ is a material constant, it is possible to calculate energy release rate per unit crack growth, G_f. This entity of quasi brittle materials is defined empirically, *e.g.* for concrete $w_c = 3d_a$, where d_a is maximum aggregate size. In addition, crack propagation results in relaxation of strain energy in some part of the structure. Knowing the geometry of such region one can write the dissipated strain energy, $U(a)$, in terms of the crack length, a. The derivative of $U(a)$ with respect to the crack length, a, then defines the energy release rate per unit of newly created crack in macroscopic domain. Therefore, the crack starts to propagate when $G_f = \partial U/\partial a$. After some basic calculations in [112, 113, 115, 103, 102, 101, 104] it is shown that the size effect follows the following:

$$\sigma^N = B\left(1 + \frac{D}{D_0}\right)^{\frac{1}{2}} + \sigma_R \tag{1.5}$$

where, B is a constant that depends on geometry and applied loading, D is size of structure, D_0 is a constant, with length dimension, which represents the size at which transition from strength theory to LEFM takes place and σ_R is the residual stress in the fractures region due to existing reinforcement such as fiber in composites or steel bars in structural concrete. For plain concrete $\sigma_R = 0$.

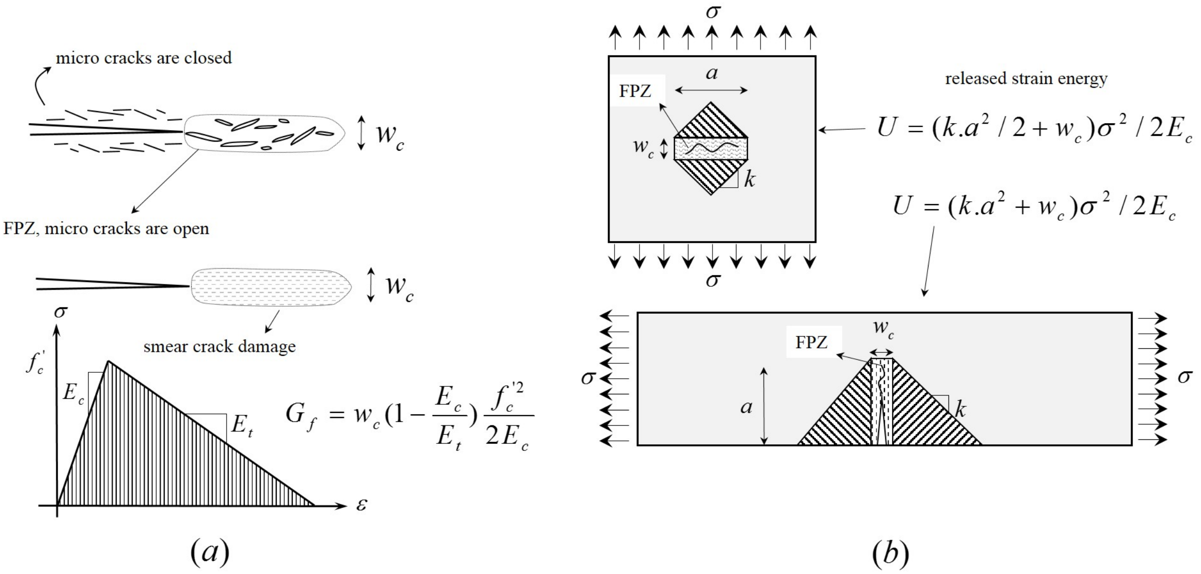

Figure 1.2: *(a) Smeared crack model with softening behavior used in crack band theory, (b) approximate zone of stress relief due to fracture.*

The soundness of the crack band theory was evaluated by dimensional analysis in [102] and the numerical results, obtained from finite element models based on this theory, was shown to be in great agreement with lab results. However, the accuracy of these numerical results is highly dependent on the accuracy of expensive laboratory experiments. For example the values of G_f, f_c' and E_t, which are necessary to describe the materials constitutive relation in the FPZ (as shown in Fig. 1.2a), are derived from expensive experimental test data. Similarly, the crack band width, w_c, in this method is defined empirically. A numerical model based on the crack band theory, despite being a beneficial tool for investigating the size effect problem, does not reflect any information about the effect of microstructural properties of materials on their macroscopic behavior, since this theory relies on the continuum description of material inside the FPZ. Fully microstructured models are suitable for this purpose since they aim at accurately modeling each and every microstructural element, but are not computationally tractable for large scale structures. An appropriate solution for this issue can be found under the umbrella of concurrent multiscale methods. These methods propose to adequately combine different descriptions of a material in a single model to ensure the accuracy and the computational efficiency of the numerical result.

The main purpose of this dissertation is to introduce a novel multiscale approach, ACM^2, in order to accurately model the fracture of materials. This method also aim at reconciling the concepts of damage mechanics, related to the microstructure of the material, and fracture mechanics, corresponding to the macroscopic level. This method is based on adaptively refining finite element mesh to transit from macroscopic scale to microscopic scale description of a material and consequently splitting the computational domain into two domains with different descriptions of the material. The method also proposes to apply necessary coupling conditions between these two domains to concurrently solve for deformation field in both domains. By combining these concepts, the method is then capable of detecting the FPZ accurately. Based on these features the method is shown to be a suitable numerical tool for obtaining the associated resistance curve and capturing the size effect of microscopically heterogeneous material. The structure of this dissertation is as follows.

Chapter two introduces the underlying ideas of the adaptive concurrent multiscale method, ACM^2, for elasticity problems. Our analysis starts from the idea that numerical simulations must ensures that numerical accuracy is maximum while the error from homogenization is minimum. While the first usually implies that element size must be refined, the second implies that elements may not be smaller than the Unit Cells of the microstructure. To accommodate these two conditions, a finite element method is introduced such that continuum elements can be replaced by explicit RVEs through properly defined macromicro kinetic conditions reminiscent to those used in classical homogenization. When combined with adaptive refinement, the methodology provides a flexible numerical method in which both continuum and microstructural descriptions can naturally coexist within a single simulation. We show, through various examples that the proposed framework addresses the important issue of reaching the optimal modeling accuracy for a minimal computational cost.

Chapter three shows that this method, in conjunction with the extended finite element method, is ideal to study the strong interactions between a crack and the microstructure of heterogeneous media. In particular, the method enables an explicit description of microstructural features near the crack tip, while a computationally inexpensive coarse scale continuum description is used in the rest of the domain. We illustrate the method with several examples showing its accuracy and relatively low computational cost and discuss its potential in relating microstructure to the fracture toughness of a diversity of heterogeneous media.

In chapter four we recapitulate the ACM^2 in conjunction with new concepts to handle the situation in which the microstructural components of a material interact with a propagating crack. This chapter also presents several examples of crack propagation in materials with random microstructures and discuss the potential of the multiscale technique in relating microstructural details to material strength and toughness. Next, in chapter five we focus on the size effect problem and aim to illustrate how the proposed method captures the size effect on the nominal strength of a heterogeneous material. Concluding remarks and suggestions for future studies are also discussed in chapter 6. It is also worth mentioning that chapters two to four include the three published journal papers that have arisen from this work. The list of these papers is as follows:

- chapter two: Vernerey, F.J., and Kabiri, M. (2012). An adaptive concurrent multiscale method for microstructured elastic solids, **Computer Methods in Applied**

Mechanics and Engineering, 241-244, pp. 52-64.

- chapter three: Kabiri, M. and Vernerey, F. J. (2013). An XFEM based multiscale approach to fracture of heterogeneous media, **International Journal of Multiscale Computational Engineering**, 11(6), pp 565-580.
- chapter four: Vernerey, F. J., and Kabiri, M (2014). Adaptive Concurrent Multiscale Model for Fracture and Crack Propagation in Heterogeneous Media, **Computer Methods in Applied Mechanics and Engineering**, 276, pp. 566588.

Chapter 2

An adaptive concurrent multiscale method for microstructured elastic solids

Franck J. Vernerey and Mirmohammadreza Kabiri
Department of Civil, Environmental and Architectural Engineering,
University of Colorado, Boulder, USA

2.1 abstract

The present paper introduces a concurrent adaptive multiscale methodology for elasticity problems in which macroscopic deformation strongly interact with microscopic deformation fields at the scale of the microstructure. This situation occurs in a variety of important situations such as ductile fracture, shear bending and when sharp discontinuities are present in the material domain. Our analysis starts from the idea that numerical simulations must ensure that numerical accuracy is maximum while the error from homogenization is minimum. While the first usually implies that element size must be refined, the second implies that elements may not be smaller than the representative volume elements (RVEs) of the microstructure. To accommodate these two conditions, a finite element method is introduced such that continuum elements can be replaced by explicit RVEs through properly defined macro-micro kinetic conditions reminiscent to those used in classical homogenization. When combined with adaptive refinement, the methodology provides a flexible numerical method in which both continuum and microstructural descriptions can naturally coexist within a single simulation. We show, through various examples that the proposed framework addresses

the important issue of reaching the optimal modeling accuracy for a minimal computational cost.

Keywords: *concurrent multiscale method, microstructured material, homogenization, strain localization.*

2.2 Introduction

Understanding how the macroscopic behavior of materials depend on their underlying microstructure has been a classical research issue in materials science but is also becoming a key question in biology and medicine. The link between structure and properties is indeed a central feature of the development of fracture resistant and multifunctional materials [53, 47] and holds the key to our understanding of how biological tissues respond, evolve and remodel [49, 48, 43]. A number of methodologies have been introduced to address this problem, most of which can be gathered under the umbrella of homogenization theory [81, 70, 67, 68, 97, 155, 30]. In this context, macroscopic behavior is cast in terms of a constitutive relation that is derived via appropriate average of the microstructure behavior in a representative volume element (or RVE) [11, 52, 40, 28]. The RVE, commonly defined as the smallest material volume that is statistically representative of the microstructure, therefore holds a central role in homogenization. Indeed, its size must always be significantly smaller than the characteristic length scale of the macroscopic problem for continuum assumptions to be valid. As such, continuum theories are usually not capable of accurately capturing material's behavior in situation where highly heterogeneous deformation fields are observed. In elasticity, this typically occurs in the presence of stress concentrations due to the presence of sharp corners, inclusions or defects whose sizes are comparable to the material's microstructure. In these cases, continuum theory can predict neither the local stress fluctuations at the material's scale (which usually are key to damage nucleation), nor the possible size effects exhibited by the microstructure (such as those observed in cellular materials [2]). Beyond the elastic range, highly heterogeneous deformation are omnipresent in situations such as in fracture [26], shear banding [20, 166], and indentation [24, 35]. In an effort to improve the predictability of continuum formulation to small scale problems, a number of extensions have been introduced to capture material's size effects and higher deformation modes [35, 32, 23]. This included higher order continuum theories such as the theory of Cosserat [135, 139, 148], the micromorphic theory [186, 187, 188], the strain-gradient theory [7, 146, 147] as well as non-local formulations in which the material response of a material point depends on its neighbors [3, 4, 5].

Although the above formulations have significantly improved our understanding of small scale material response [188], they are still based on continuum assumptions that implicitly assume a scale separation between the macroscopic problem and the deformation of the RVE. In fact, when the wave length of a macroscopic deformation field is at the same order as that characteristic size of the microstructure, it can be argued that the global material response becomes less important than its local response. In this case, the local response is affected by the stochasticity of the microstructure and a deterministic continuum framework is no longer applicable. This raises an important issue in multiscale modeling. On the one hand, the above considerations imply that a small scale material description (including microstructural details) is necessary in problems that display highly heterogeneous macroscopic deformation. On the other hand, such a refined description in macroscale domains often leads to an intractable computational problem. An optimal solution is therefore found in methods that can adequately couple a fine material description in regions of highly localized deformation and a coarse description in regions of homogeneous deformation. This idea was used in concurrent methods such as the bridging scale method [166, 156, 189, 132] in which a microscopic region (near a crack tip for instance) can be determined a priori. Such methods are then able to couple continuum models (such as finite element) and small scale material descriptions (such as molecular dynamics). A recurrent problem, however, is that the small scale region cannot, in general, be determined before hand. In this context, Ghosh et al.[150, 149, 160, 169, 168] introduced a concurrent multiscale method using Voronoi cell finite element method (VCFEM), which is based on adaptively refining mesh on three different levels of subdomains with various resolutions. The first level is a conventional displacement based finite element model based on constitutive moduli obtained from homogenization of microstructural parameters. The second level is an intermediate level used for switching between macro and micro description models, with higher computational demand compared to the two other levels. The third level subdomain, where damage evolution initiates and periodic boundary condition assumptions for microstructural RVE fail, a detailed microstructural model is formulated using VCFEM. This method addresses damage evolution in composites and heterogeneous materials in an accurate and efficient way.

In the present work, we introduce a novel adaptive multiscale method whose fundamental basis rests on the minimization of both numerical error and homogenization error. The numerical error typically arises from the fact that numerical approximations (provided by shape functions in finite elements) introduce a difference between computational and exact solutions in continuum mechanics. While this error is known to decrease with element size, excessive element refinement may lead to a situation in which element size becomes comparable to that of the microstructure. In this case, we show that additional refinement can induce significant errors in the continuum approximation of the material response. To address this issue, we introduce a numerical method in which elements, once they reach a critical size, can be replaced by explicit RVEs that coexist with a macroscopic continuum description. Upon combining this method with conventional adaptive refinement techniques, we obtain a computational formulation that possesses two major advantages. First, it maintains a relatively low computational cost since a coarse scale continuum description is used in regions of homogeneous deformation. Second, it provides a refined description of the microstructure in regions of heterogeneous deformation and does not violate the fundamental assumptions of continuum theories. In addition, the method provides a flexible framework, based on only two levels of material description, in which the location and size of the microscopic domain does not need to be predetermined and can eventually evolve with material deformation.

The paper is organized as follows. In the next section (section 2), we provide an analysis of two different types of errors that may arise in a finite element analysis and derive a criterion that governs the allowable element size. In section 4 we then introduce a bridging scale method in order to enable RVEs to coexist with a surrounding macroscopic finite element mesh. In the 4th section we combine the embedded RVE method with adaptive refinement in order to derive the final form of the proposed method. A few examples are then discussed to assess the efficiency and accuracy of the framework. Section 5 finally provides a summary of the work and suggests few improvements and extensions for the future.

2.3 Error in homogenization theory and finite elements

One of the principal objectives of multiscale methods is to ensure that modeling accuracy is maximum while the computational cost is minimum. A low computational cost can usually be obtained by using a coarse-grained homogenized continuum model such that unnecessary "fine scale" degrees of freedom are appropriately smeared out. Such an approach, however can introduce some inaccuracies in the solution, especially when the typical wave length of deformation is on the order of characteristic length of the microstructure. In fact, modeling accuracy might be dictated by several factors. On the one hand, numerical discretization error arises from the fact that the approximation provided by finite elements does not exactly capture the exact continuum fields such as displacement, strains or stresses in most situations. On the other hand, a so-called homogenization error may arise from the fact that continuum theories can only describe an average material response, which may not be enough in certain cases. We see in this section that these two types of errors lead, in certain situations, to very inappropriate solutions if continuum theories are solely used.

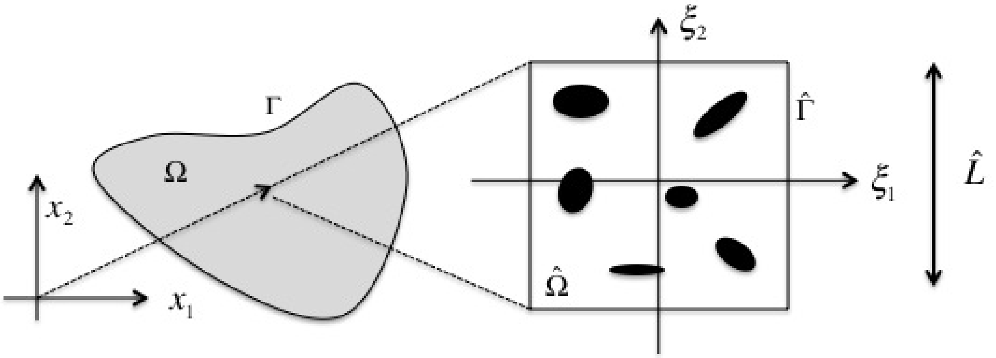

Figure 2.1: *Continuum macrostructure and heterogeneous microstructure associated with the point located at position* $\mathbf{x}$.

2.3.1 Homogenization error

Let us first assess the homogenization error that can result from the use of coarse grain continuum formulations. We base our arguments on classical first-order continuum theories, i.e., the stored energy in an elastic body exclusively depends on the first gradient of the displacement fields. While this may seem restrictive, the arguments presented in this section may be extended to high-order theories if needed.

Consider a macroscopic elastic body that is contained in a closed domain Ω and delimited by a boundary Γ. Refering to a Cartesian coordinate system with coordinates $\{x_i\}, i = 1, 2, 3$, the state of a material point P, located at position $\mathbf{x}$ can usually be described in terms of continuum quantities such as the displacement field $\mathbf{u}(\mathbf{x})$, the strain field $\boldsymbol{\epsilon}(\mathbf{x})$ or the stress field $\boldsymbol{\sigma}(\mathbf{x})$. From a multiple-scale view point, these macroscopic quantities are interpreted as averages over a material domain that is small relative to macroscopic dimensions. As depicted in Fig. (1), this domain is often denoted as the representative volume element (or RVE) and traditionally defined as the smallest material domain that statistically describes the material's microstructure. For simplicity, we represent such an RVE as a square domain $\hat{\Omega}$ with side length of $\hat{L}$, delimited by a boundary $\hat{\Gamma}$ and in which the highly fluctuating microscopic displacement, strain and stress fields are represented by

$\hat{\mathbf{u}}$, $\hat{\boldsymbol{\epsilon}}$ and $\hat{\boldsymbol{\sigma}}$, respectively. Relationships between macro and micro quantities (represented by $\diamond$ here) are then established in terms of the average operation:

$$\langle \diamond \rangle = \frac{1}{|\hat{\Omega}|} \int_{\hat{\Omega}} \diamond \, d\hat{\Omega}. \tag{2.1}$$

In particular, for a first-order continuum theory and small displacement assumptions, an infinitesimal change in macroscale elastic energy δW is related to its microscopic counterpart through the Hill-Mandel condition [87, 72]:

$$\delta W = \langle \hat{\boldsymbol{\sigma}} : \delta \hat{\boldsymbol{\epsilon}} \rangle \tag{2.2}$$

where $\delta \hat{\boldsymbol{\epsilon}} = \{\nabla \delta \hat{\mathbf{u}}\}^s$ and the superscript s is used to denote the symmetric part of the second-order tensor. Consistent with a first-order theory, we assume that the displacement field in the RVE can be given by the expansion:

$$\hat{\mathbf{u}}\left(\boldsymbol{\xi}\right) = \hat{\mathbf{u}}\left(\mathbf{0}\right) + \langle \hat{\nabla} \hat{\mathbf{u}} \rangle \cdot \boldsymbol{\xi} + \frac{1}{2} \boldsymbol{\xi} \cdot \langle \hat{\nabla} \hat{\nabla} \hat{\mathbf{u}} \rangle \cdot \boldsymbol{\xi} + \hat{\mathbf{u}}^f(\boldsymbol{\xi}). \tag{2.3}$$

Here, $\boldsymbol{\xi}$ is a nondimensional local coordinate defined as $\boldsymbol{\xi} = \left(\mathbf{y} - \mathbf{x}\right)/\hat{L}$ and the vector $\mathbf{y}$ is the position vector in a coordinate system whose origin is the geometric center of the RVE. Furthermore, the local gradient operator is defined as $\hat{\nabla} = \partial / \partial \boldsymbol{\xi}$ and the quantity $\hat{\mathbf{u}}^f(\boldsymbol{\xi})$ describes the fluctuating component of the displacement that is not captured by the series expansion. Now realising that the average fields at the microscale are equal to the macroscale fields, we obtain:

$$\langle \hat{\nabla} \hat{\mathbf{u}} \rangle = \hat{L} \nabla \mathbf{u} \quad \text{and} \quad \langle \hat{\nabla} \hat{\nabla} \hat{\mathbf{u}} \rangle = \hat{L}^2 \nabla \nabla \mathbf{u}. \tag{2.4}$$

Using this approximation in (2.3) and subsequently in (2.2) leads to the following expression of the macroscopic elastic energy:

$$\delta W = \boldsymbol{\sigma} : \delta \boldsymbol{\epsilon} + \boldsymbol{\tau} \,\vdots\, \left(\hat{L} \nabla \nabla \delta \mathbf{u}\right) + \langle \hat{\boldsymbol{\sigma}} : \hat{\nabla} \delta \mathbf{u}^f \rangle \tag{2.5}$$

where the macro-stress is logically given by $\boldsymbol{\sigma} = \langle \hat{\boldsymbol{\sigma}} \rangle$ and the stress-couple $\boldsymbol{\tau}$ is introduced as $\boldsymbol{\tau} = \langle \hat{\boldsymbol{\sigma}} \otimes \boldsymbol{\xi} \rangle$. Since first-order theories only express the elastic energy in terms of the first term on the right hand-side, it remains valid only if the last two terms are sufficiently small to be neglected. As will be discussed in section 2.4.1.2, the last term identically vanishes by enforcing proper boundary conditions in the RVE. The middle term, however, can only be neglected if

$$\boldsymbol{\tau} \vdots \left(\hat{L}\nabla\nabla\delta\mathbf{u}\right) << \boldsymbol{\sigma} : \delta\boldsymbol{\epsilon}. \tag{2.6}$$

The couple stress $\boldsymbol{\tau}$ is a bounded quantity [30] that can only remain within the same order of magnitude as the macrostress $\boldsymbol{\sigma}$. Furthermore, since the strain is typically on the order of (but less than) unity, the above condition can be rewritten in terms of a conditions on the second displacement gradient as follows:

$$e_h = \hat{L}||\nabla\nabla\mathbf{u}|| << 1 \tag{2.7}$$

where the L_2 norm of the second displacement gradient is written in indicial notation as $||\nabla\nabla\mathbf{u}|| = \sqrt{u_{i,jk}u_{i,jk}}$. Here, we introduced a homogenization error quantity e_h that must remain small everywhere in Ω for first-order theory to remain valid.

2.3.2 Discretization error

As discussed previously, the discretization error is measured by the difference between the exact continuum solution and the solution provided by the numerical scheme (finite elements in our case). In the present work, we are particularly interested in the error in strain fields (or displacement gradient) in individual elements. In this context, let us consider that the body Ω is decomposed in a number of finite elements and define Ω_e the physical domain associated with an arbitrary element e. The discretization error e_d in this element may then be written in terms of the difference between the exact solution of the displacement gradient $u_{i,j}$ and that provided by the finite element approximation $u^h_{i,j}$ as follows [138]:

$$e_d = \left(\int_{\Omega_e} \left(u_{i,j} - u^h_{i,j}\right)\left(u_{i,j} - u^h_{i,j}\right) d\Omega_e\right)^{1/2}, \tag{2.8}$$

where the Einstein convention related to summations on repeated indices is applied. To assess this quantity, it is useful to introduce a local Cartesian coordinate system z_i with origin in the geometric center of the element, in which the exact displacement field can be written in term of a Taylor series expansion as:

$$u_i(\mathbf{z}) = \bar{u}_i + \chi_{ij} z_j + \frac{1}{2} H_{ijk} z_j z_k + O(\mathbf{z}^3), \tag{2.9}$$

where $\bar{\mathbf{u}}$ is a displacement vector at $\mathbf{z} = 0$, $\boldsymbol{\chi}$ is interpreted as the deformation gradient tensor and $\mathbf{H}$ is a third-order tensor representing the second displacement gradient in the element. Further, for first-order continua, it is sufficient to consider linear (or bi-linear) two-dimensional elements in which the displacement $\mathbf{u}_h$ can be written as a function of $\mathbf{z}$ as:

$$u_i^h(\mathbf{x}) = \bar{u}_i^h + \chi_{ij}^h x_j. \tag{2.10}$$

Here, the superscript h denotes the numerical solution. Note that for four nodes finite element, the approximate displacement also contains some bi-linear terms, but this does not affect the remainder of the derivations. The difference between exact and approximate displacement therefore reads:

$$u_i(\mathbf{z}) - u_i^h(\mathbf{z}) = e_i + B_{ij} z_j + \frac{1}{2} H_{ijk} z_j z_k, \tag{2.11}$$

where $\mathbf{e} = \bar{\mathbf{u}} - \bar{\mathbf{u}}^h$ and $\mathbf{B} = \boldsymbol{\chi} - \boldsymbol{\chi}^h$. The above equation is representative of a family of conics with center $\mathbf{z}_c$ [138]. Furthermore, it can be shown that the error in displacement shown in (2.11) identically vanishes at nodal locations and takes a maximum value at the center $\mathbf{z}_c$ of the cone. One can further find that [138], under an appropriate change of coordinate, (2.11) can be rewritten in terms of the error ε at the center of the cone and new coordinates $\bar{\mathbf{z}}$ that have their origin at $\mathbf{z}_c$, in the form:

$$u_i(\mathbf{z}) - u_i^h(\mathbf{z}) = \epsilon_i - \frac{1}{2} H_{ijk} \bar{z}_j \bar{z}_k. \tag{2.12}$$

For the sake of simplicity, let us evaluate the error in a square element, whose size h is given by the length of its side. In this case, the center of the cone coincides with the geometric center of the element, i.e., $\mathbf{z} = \bar{\mathbf{z}}$. Substituting (2.12) in (2.8) then leads to:

$$e_d^2 \;=\; H_{ijm} H_{ijn} \int_{\Omega_e} z_m z_n \, d\Omega \;=\; \frac{h^2}{12} H_{ijk} H_{ijk}. \tag{2.13}$$

Recognizing that the tensor $\mathbf{H}$ is a measure of the second displacement gradient $\nabla\nabla\mathbf{u}$ in the element, the discretization error can finally be written as:

$$e_d = hc||\nabla\nabla\mathbf{u}|| \tag{2.14}$$

where $c = 1/\sqrt{12}$ and the L_2 norm $||\cdot||$ was defined in the previous section. This result shows, as discussed in [96], that the discretization error can be written in terms of the second displacement gradient and is a decreasing function of the element size h. This is a particularly useful result as the evolution of both discretization and homogenization errors may now be assessed in terms of element size. For instance, let us consider a situation in which the norm of the second displacement gradient $||\nabla\nabla\mathbf{u}||$ is fixed and we wish to investigate the gain in accuracy by decreasing the element size h. Using (3.2) and (4.2), it is possible to plot both homogenization and discretization errors as a function of h as illustrated in Fig. 2.2a. By defining the total error e as the maximum of e_h and e_d, it becomes clear that the error decreases linearly with element size as long as $h > \hat{L}/c$. However, further refinement ($h < \hat{L}/c$) ceases to improve the accuracy of the solution as the homogenization error becomes dominant.

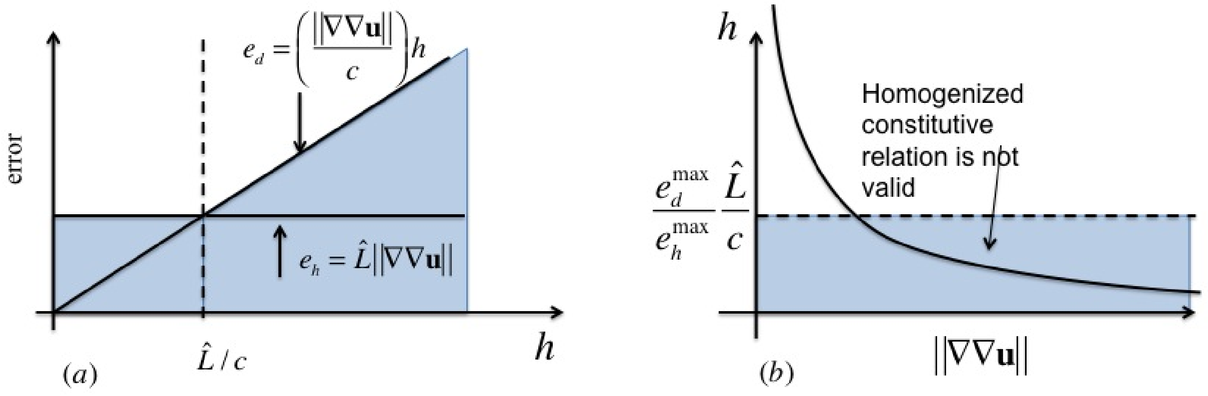

Figure 2.2: *(a) Evolution of error measures with element size when the quantity* $||\nabla\nabla\mathbf{u}||$ *is fixed. (b) critical element size in terms of the norm of the second displacement gradient* $||\nabla\nabla\mathbf{u}||$

2.3.3 Limits of the continuum based finite element method

From the above analysis, it can be seen that, in order to be accurate, a solution must ensure that both the homogenization error e_h and the discretization error e_d are significantly smaller than unity. Practically, we can therefore define maximum allowable errors e_h^{max} and e_d^{max} such that the solution is satisfactory if:

$$e_h < e_h^{max} \qquad \text{and} \qquad e_d < e_d^{max}. \tag{2.15}$$

We note here that the quantity e_h^{max} measures the difference between the typical length scale associated with strain gradient and the size of RVEs. To ensure that we do not violate the assumptions of continuum mechanics, a guideline would consist of choosing e_h^{max} such that $||\nabla\nabla\mathbf{u}||$ remains smaller than 1% of $1/\hat{L}$, i.e. e_h^{max} is less than 0.01. In contrast, the discretization error measures the difference between the finite element approximation and the analytical solution. The choice of e_d^{max} is therefore an important indicator of numerical accuracy. In the present study, we choose $e_d^{max} = 0.01$, i.e. the numerical solution is always at least 99% accurate. Since the discretization error decreases with element size, according to (4.2), classical refinement techniques can be used such that the size of elements is smaller than a critical size h^c defined as:

$$h^c = \frac{e_d^{max}}{c||\nabla\nabla\mathbf{u}||} \tag{2.16}$$

As a result, it can be seen that as the second gradient of deformation increases, the element size should inversely decrease in the fashion exhibited in Fig. 2.2b. Now enforcing the condition on homogenization error in the form $\hat{L}||\nabla\nabla\mathbf{u}|| < e_h^{max}$ and using (2.16), one obtains the following condition on the element size h^c:

$$h^c > \frac{e_d^{max}}{c(e_h^{max})}\hat{L}. \tag{2.17}$$

This enforces a strong condition on the critical element size so that the assumptions of first-order continuum theory are satisfied. As depicted in Fig. 2.2b, an element's size reaches a critical value $h^c = \hat{L}(e_d^{max}/c(e_h^{max}))$ when the second displacement gradient is such that

$||\nabla\nabla\mathbf{u}|| = e_h^{max}/\hat{L}$. This result is important as it implies that in certain cases, the variation of strain is so large that the validity of the continuum theory fails regardless of the size of elements. To better understand this, let us consider the case in which the relation between the maximum discretization and homogenization errors is $e_d^{max} = c(e_h^{max})$. In this case, (5.5) states that continuum assumptions are violated if the element size is smaller than the size $\hat{L}$ of the RVE. One can interpret this as follows. When the element size is larger than that of the RVE, they can be considered as appropriate domains on which homogenized material response can be used. However, as they become smaller than the RVE, the average material response is no longer valid and elements should be replaced by a more accurate description of the material's structure. To address this issue, we next introduce a computational method that naturally substitutes continuum elements by RVE when the minimum element size is such that it violates homogenization theory. The method guarantees that both discretization and homogenization errors converge to small values, regardless of the second displacement gradients.

2.4 Finite element with embedded RVE

As discussed above, when the size of elements becomes close to that of the RVEs, the validity of homogenized constitutive relation breaks down. Relying on the error criterion deduced above, we derive a numerical approach in which finite elements can be replaced by RVEs in the case when element size becomes critical ($h = h_c$). This idea is depicted in Fig. (3), in which the cases of a single embedded RVE and a patch of embedded RVEs are shown. A potential issue with this method is that RVEs and macroscale elements are representative of a material at very different resolutions and the bridging between macroscopic forces and displacements and their microscopic counterparts is usually subjected to debates. This section addresses this issue by introducing three possible types of macro-micro conditions.

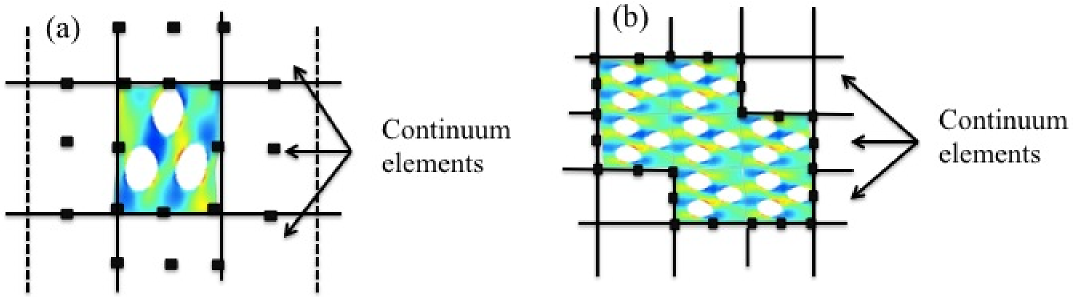

Figure 2.3: *Illustration of embedded RVE in a macroscopic finite element mesh; (a) case of a single embedded RVE and (b) case of a patch of embedded RVEs.*

2.4.1 Multiscale RVE-FEM bridging method

To appropriately bridge the mechanics of an embeded RVE to the surrounding macroscopic elements, it is first useful to derive a relationship between the kinematics at the macroscopic (continuum element) and microscopic (RVE) level. This is the object of this subsection.

2.4.1.1 Macro-micro kinematic

Let us consider an initially rectangular shaped RVE on which a macroscopic finite element is superposed (Fig. (3)a). The micro-macro kinematic compatibility conditions then imposes that the deformation of the element is "in average" the same as that of the RVE. To investigate the mathematical consequence of such a statement, let us first write the microscopic displacement in the RVE as follows:

$$\mathbf{u}(\boldsymbol{\xi}) = \sum_I N^I(\boldsymbol{\xi})\mathbf{U}^I + \mathbf{u}^f(\boldsymbol{\xi}) \tag{2.18}$$

where N^I is the macroscale shape function associated with node I and $\mathbf{u}^f(\boldsymbol{\xi})$ is an arbitrary fluctuation field. The displacement gradient in the element may then be written in terms of the differential operator $\hat{\nabla}$ as:

$$\hat{\nabla}\mathbf{u}(\boldsymbol{\xi}) = \sum_I \mathbf{B}^I(\boldsymbol{\xi})\mathbf{U}^I + \hat{\nabla}\mathbf{u}^f(\boldsymbol{\xi}) \tag{2.19}$$

where we introduced the derivatives of shape functions as $\mathbf{B}^I = \partial N^I/\partial\boldsymbol{\xi}$. The average displacement gradient in the RVE can then be written as:

$$\langle\hat{\nabla}\mathbf{u}\rangle = \sum_I \langle\mathbf{B}^I\rangle\mathbf{U}^I + \langle\hat{\nabla}\mathbf{u}^f\rangle \tag{2.20}$$

where the average deformation of the element is given by the first term on the right hand side. Thus, the compatibility of RVE and element deformation implies that the gradient of fluctuation fields must vanish, in average, in the RVE. This yields:

$$\langle\hat{\nabla}\mathbf{u}^f\rangle = \frac{1}{|\hat{\Omega}|}\int_{\hat{\Gamma}} \hat{\mathbf{u}} \otimes \mathbf{n}\, d\hat{\Omega} = 0 \tag{2.21}$$

where $\mathbf{n}$ is the unit normal vector to the boundary of the RVE and we applied the divergence theorem to obtain the surface integral. The above equation is important as it gives a condition on the fluctuating displacement on the edge of the RVE; it will prove useful in deriving coupling conditions between macroscale and microscale as discussed in the next sections.

2.4.1.2 Relationship between macroscopic and microscopic forces

Let us now assess the relationship between macroscopic nodal forces and microscopic RVE surface forces. In this context, it is useful to first write the variation of energy in an RVE as:

$$\delta\hat{w} = \int_{\hat{\Omega}} \hat{\boldsymbol{\sigma}} : \delta\hat{\boldsymbol{\epsilon}} d\hat{\Omega} = \int_{\hat{\Gamma}} \hat{\mathbf{t}} \cdot \delta\hat{\mathbf{u}} d\hat{\Gamma} \tag{2.22}$$

where $\hat{\mathbf{t}}$ is the Cauchy stress vector on the RVE boundary. Assuming that the variation of energy, associated with the fluctuation field, vanishes globally [155], i.e.,

$$\int_{\hat{\Gamma}} \hat{\mathbf{t}} \cdot \delta\mathbf{u}^f d\hat{\Gamma} = 0, \tag{2.23}$$

one can substitute (2.18) in (3.8) and find the traditional expression for the energy of a macroscopic element:

$$\delta\hat{w} = \sum_I \mathbf{f}^I \cdot \delta\mathbf{U}^I \tag{2.24}$$

where the macroscopic nodal forces are related to the traction forces $\hat{\mathbf{t}}$ on the micro-macro boundary by:

$$\mathbf{f}^I = \sum_I \int_{\hat{\Gamma}} N^I \hat{\mathbf{t}} d\hat{\Gamma}. \tag{2.25}$$

It should be noted that the magnitude and distribution of $\hat{\mathbf{t}}$ depends on the type of displacement fluctuations on $\hat{\Gamma}$. We next review three type of conditions on fluctuation fields that find their analogue in traditional computational homogenization.

2.4.2 Types of macro-micro coupling assumptions

2.4.2.1 Strong displacement coupling

The simplest way of verifying (3.7) consists of enforcing the fluctuation fields $\tilde{\mathbf{u}}$ to identically vanish at every point on the RVE boundary. Setting $\tilde{\mathbf{u}} = 0$ in (2.18) yields the following relationship between micro and macro displacement:

$$\mathbf{u}(\boldsymbol{\xi}) = \sum_I N^I(\boldsymbol{\xi})\mathbf{U}^I, \qquad \boldsymbol{\xi} \in \hat{\Gamma}. \tag{2.26}$$

This condition clearly enforces the microscopic displacement to precisely follow the macroscopic displacement variation interpolated by the macroscopic shape functions. From a numerical view point, the above constraints can typically be enforced with the Lagrange multiplier method, in which two constraints (represented by a vector $\mathbf{c}$) are enforced at every microscopic node that belongs to the micro-macro boundary. This therefore leads to a system of equations of $2N^m$ where N^m is the number of microscopic nodes on the macro-micro boundary. More precisely, considering a microscopic node n on $\hat{\Gamma}$, the constraint $\mathbf{c}_n$ is given by:

$$\mathbf{c}_n = \mathbf{u}_n - \sum_I N^I(\boldsymbol{\xi}_n)\mathbf{U}^I = 0 \tag{2.27}$$

where $\boldsymbol{\xi}_n$ is the location of node n in the local coordinate system of the RVE. This constraint is associated with a Lagrange multiplier $\boldsymbol{\lambda}_n$ that can be identified as the microscopic traction force at node n. Fig. (4)a illustrates the deformation of adjacent microscopic RVE and macroscopic element resulting from a strong displacement crouping. Note that no small scale fluctuations are allowed on the edge of the RVE; this coupling may thus be compared to Dirichlet-type boundary conditions in classical homogenisation, which are known to over-estimate the stiffness of the RVE.

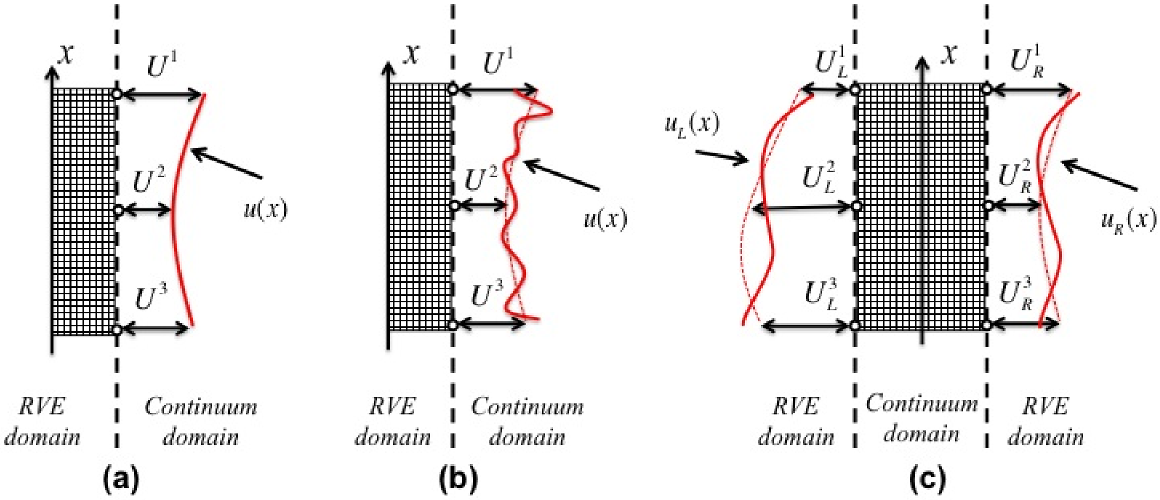

Figure 2.4: *Representation of the three types of micro-macro boundary coupling constraints; (a) strong displacement coupling, (b) weak displacement coupling and (c) quasi-periodic boundary coupling.*

2.4.2.2 Weak displacement coupling

A way to remove some of the contraints on the RVE is to apply the so-called weak displacement coupling. In this case, we seek to minimize the effect of fluctuating fields on each boundary of the RVE. Denoting each of the four boundaries by the parameter α ($\alpha = T, B, R, L$ for the top, bottom, right and left boundaries, respectively), an error measure can be defined for each boundary as:

$$e = \int_{\hat{\Gamma}_\alpha} \left(\mathbf{u}(\boldsymbol{\xi}) - \sum_I N^I(\boldsymbol{\xi}) \mathbf{U}^I \right) d\hat{\Gamma} \qquad \alpha = T, B, R, L. \tag{2.28}$$

To enforce that (3.7) is weakly satisfied, we minimize the error of each boundary with respect to the macroscopic displacements. This leads to the following system:

$$\mathbf{g}^I \left(\mathbf{U}^J, \mathbf{u}^k \right) = \frac{\partial e}{\partial \mathbf{U}^I} = 0 \qquad \forall I, J \in \hat{\Gamma} \tag{2.29}$$

where $\mathbf{u}^k$ is the displacement of microscopic node k that belongs to the micro-macro boundary. It can therefore be noticed that the weak coupling leads to the application of $2N$ equations, where N is the number of macroscopic nodes on boundaries $\hat{\Gamma}_\alpha$ (N=3 in the illustration in Fig. (4)b). Enforcing those constraints via the Lagrange multiplier method leads to the definition of $2N$ multipliers λ^I, which can be interpreted as macroscopic nodal forces. This usually represents a significant decrease in the number of contraints compared to the strong displacement coupling conditions. Consequences of the weak conditions are depicted in Fig. (4)b, in which the microscopic deformation displays fluctuations on the RVE edge although the RVE conform to the deformation of surrounding elements in an average fashion. This situation may thus be thought as analogue to the case of Neumann boundary conditions in classical homogenization.

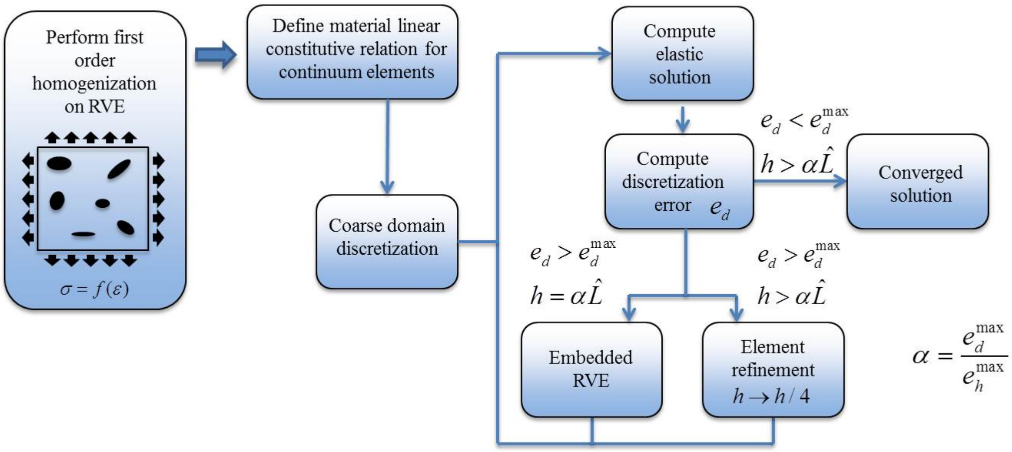

Figure 2.5: *Algorithm used in the adaptive multiscale method.*

2.4.2.3 Quasi-periodic boundary coupling

This condition is based upon the assumption of the periodicity of the microstructure and aims to dictate a periodic deformation of RVE while conforming to the surrounding macroscopic continuum. In the case of an initially rectangular RVE considered in this study, it is possible to define two corresponding points on opposite boundaries denoted by $\hat{\Gamma}_T$

and $\hat{\Gamma}_B$ for top and bottom RVE boundaries and $\hat{\Gamma}_L$ and $\hat{\Gamma}_R$ for left and right boundaries, respectively. Further introducing the outward unit normal vectors to these boundaries by $\mathbf{n}_T$, $\mathbf{n}_B$, $\mathbf{n}_L$ and $\mathbf{n}_R$, one can show that (3.7) is verified if:

$$\tilde{\mathbf{u}}_B(\xi) = \tilde{\mathbf{u}}_T(\xi) \qquad \text{and} \qquad \tilde{\mathbf{u}}_R(\eta) = \tilde{\mathbf{u}}_L(\eta) \tag{2.30}$$

where ξ and η are the local RVE coordinates shown in Fig. (1). This automatically implies from (2.18) that:

$$\begin{aligned} \delta\mathbf{u}_T(\xi) - \delta\mathbf{u}_B(\xi) &= \sum_I N^I(\xi,1)\delta\mathbf{U}_T^I - \sum_I N^I(\xi,-1)\delta\mathbf{U}_B^I && (2.31) \\ \delta\mathbf{u}_R(\eta) - \delta\mathbf{u}_L(\eta) &= \sum_I N^I(1,\eta)\delta\mathbf{U}_R^I - \sum_I N^I(-1,\eta)\delta\mathbf{U}_L^I. && (2.32) \end{aligned}$$

Enforcing these constraints leads to the introduction of Lagrange multipliers for each pair of nodes on corresponding boundaries. These multipliers have the physical meaning of traction forces and can be used to find the macroscopic forces via (3.10). This type of periodic boundary coupling not only preserves micro structural periodic behavior, which is expected for all periodic materials, but also results in a more physically sound solution compared to other conditions. Using linear quadrilateral elements for continuum modeling of structure, this formulation by itself leads to both periodicity in deformed state and conformity of macro-micro displacement. However, for higher order elements (i.e., quadratic elements), this formulation does not fully ensure conformity of deformation between RVE and macro-elements. To resolve this issue, periodic boundary coupling conditions can be enforced in combination with weak displacement coupling condition on one of two opposite boundaries ($\hat{\Gamma}_T$ and $\hat{\Gamma}_R$, for instance). As depicted schematically in Fig. (4)c, such coupling conditions lead to quasi-periodic deformed state, which allows fluctuation of micro displacement and conformity between RVE and adjacent elements. Note that when large strain and rotation gradient exits, RVEs lose their rectangular shapes and become non-periodic. This is the reason why the term “quasi”-periodic conditions is used. Finally, it is important to mention that since adjacent RVEs share the same microscopic nodes, no Lagrange multipliers are needed for coupling their displacement. The Lagrange multipliers are only used to enforce kinematic constraints between microscopic and macroscopic nodes on the continuum-microstructural boundary.

2.5 Adaptive multiscale method: computational aspects and examples

This section now introduces a multiple scale algorithm that combines the concepts of embedded RVEs discussed above and that of adaptive element refinement. Given a specific elasticity problem, the methodology's objective is to minimize discetization error via refinement, and to provide maximum accuracy in terms of material modeling by embedding RVEs when the critical element size is reached. The method is based on the algorithm presented in Fig. 5. The numerical method is based on rectangular quadratic (nine-node) finite elements in order to facilitate the calculation of the discretization error defined in (4.2). In particular, the second gradient of a displacement field in point $\mathbf{x}$ in a quadratic element can be written as a 6×1 matrix as:

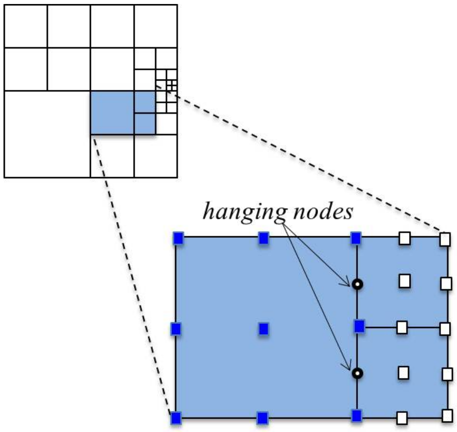

Figure 2.6: *Illustration of hanging nodes between elements of different sizes*

$$\nabla\nabla\mathbf{u}(\mathbf{x}) = [\frac{\partial^2 u_x}{\partial x^2}\ \frac{\partial^2 u_x}{\partial x \partial y}\ \frac{\partial^2 u_x}{\partial y^2}\ \frac{\partial^2 u_y}{\partial x^2}\ \frac{\partial^2 u_y}{\partial x \partial y}\ \frac{\partial^2 u_y}{\partial y^2}]^T = \sum_{I=1}^{9} \mathbf{G}^I(\mathbf{x})\mathbf{u}^I \qquad (2.33)$$

Where $\mathbf{u}^I = [u_x^I \ u_y^I]^T$ is nodal displacement vectors at node I and $\mathbf{G}^I(\mathbf{x})$ is a matrix given by:

$$\mathbf{G}^I(\mathbf{x}) = \begin{bmatrix} \frac{\partial^2 N_I(\mathbf{x})}{\partial x^2} & \frac{\partial^2 N_I(\mathbf{x})}{\partial x \partial y} & \frac{\partial^2 N_I(\mathbf{x})}{\partial y^2} & 0 & 0 & 0 \\ 0 & 0 & 0 & \frac{\partial^2 N_I(\mathbf{x})}{\partial x^2} & \frac{\partial^2 N_I(\mathbf{x})}{\partial x \partial y} & \frac{\partial^2 N_I(\mathbf{x})}{\partial y^2}. \end{bmatrix}^T \tag{2.34}$$

With this notation, it is straightforward to show that the L2 norm of second gradient of displacement in a quadratic element takes the form:

$$\|\nabla\nabla\mathbf{u}(\mathbf{x})\|_2 = \left(\sum_{I=1}^{9} \left(\mathbf{u}^I(\ \mathbf{x})\right)^T \left(\int_\Omega \left(\mathbf{G}^I(\mathbf{x})\right)^T \mathbf{G}^I(\mathbf{x}) d\Omega \right) \mathbf{u}^I(\mathbf{x}) \right)^{1/2}. \tag{2.35}$$

Finite element refinement then consists of subdividing elements that display large error measures into four sub-elements. This technique is known to introduce hanging nodes that are present in small elements but are non-existent in adjacent elements of larger size (Fig. 6). To solve this discrepancy, large elements, such as that depicted on the right of Fig. 6, are enriched with addition shape functions associated with the hanging node in a way that conventional conditions on shape functions (continuity and partition of unity) are satisfied. The form of the new shape function, presented in the appendix, ensures that a force equilibrium is appropriately enforced between elements of different sizes.

Upon convergence of the multiscale algorithm, the computational problem reduces, for a linear elastic material undergoing small deformation, into a linear system of the form:

$$\begin{bmatrix} \mathbf{K}_M & \mathbf{0} & \mathbf{I}_{Mm}^{\mathbf{T}} \\ \mathbf{0} & \mathbf{K}_m & \mathbf{I}_{mM}^{\mathbf{T}} \\ \mathbf{I}_{Mm} & \mathbf{I}_{mM} & \mathbf{0} \end{bmatrix} \begin{bmatrix} \mathbf{u}^M \\ \mathbf{u}^m \\ \boldsymbol{\lambda} \end{bmatrix} = \begin{bmatrix} \mathbf{f}^M \\ \mathbf{f}^m \\ \mathbf{c} \end{bmatrix} \tag{2.36}$$

where subscript M and m represent “macro” continuum elements and the “micro” embedded RVEs, respectively, while $\mathbf{K}$, $\mathbf{u}$ and $\mathbf{f}$ are used to represent stiffness matrices, nodal displacement vector and external force vector, respectively. In addition, the symbol $\boldsymbol{\lambda}$ represents Lagrange multipliers that enforce the macro-micro conditions $\mathbf{c} = 0$ derived in the section 2.4.2. We note that the stiffness matrix is decomposed into different parts: the first diagonal block $\mathbf{K}_M$ represents the macroscopic stiffness associated with continuum elements and the second diagonal block $\mathbf{K}_m$ represents the stiffness arising from the presence of RVEs. Displacements at macro and micro levels are then coupled via the presence of interaction matrices $\mathbf{I}_{Mm}$ and $\mathbf{I}_{mM}$ that represent the derivative of the macro-micro constraints $\mathbf{c}$ with respect to macro and micro displacements, respectively. It can generally be observed that the system is clearly decoupled into a macroscopic problem (continuum elements), a microscopic problem (RVE) and their interactions. Finally, we note that for consistency between micro and macroscales, the constitutive relation at the continuum scale is ultimately derived from a first order computational homogenization procedure (Fig. 5). For instance, in the present study, an isotropic, linear elastic constitutive relation is obtained by relating the average RVE strain to the average RVE stress after subjecting the RVE domain to appropriate boundary conditions. For more information on this method, the reader is referred to [186]. We next illustrate the features of the method and assess its performance in terms of accuracy and cost by considering a few examples. We mostly concentrate on macroscopic elasticity problems for which the material is described at the microscale by a voided linear elastic microstructure. The distribution of voids in the RVE is chosen such that the overall response remains isotropic.

2.5.1 Example 1: Effect of micro-macro coupling constraints

The first example aims at investigating the role of using different micro-macro constraints on the deformation of embedded RVEs. As such, we consider a purely academic problem of a square domain, discretized with eight microscopic elements that possesses an embedded RVE in its center. The domain is then subjected to inhomogeneous deformation through the application of displacement boundary conditions depicted in Fig. 7. The deformation of the embedded RVE is then assessed for the three types of boundary coupling conditions introduced in the previous section.

Regardless of the coupling conditions, it can be seen that the RVE globally displays significant

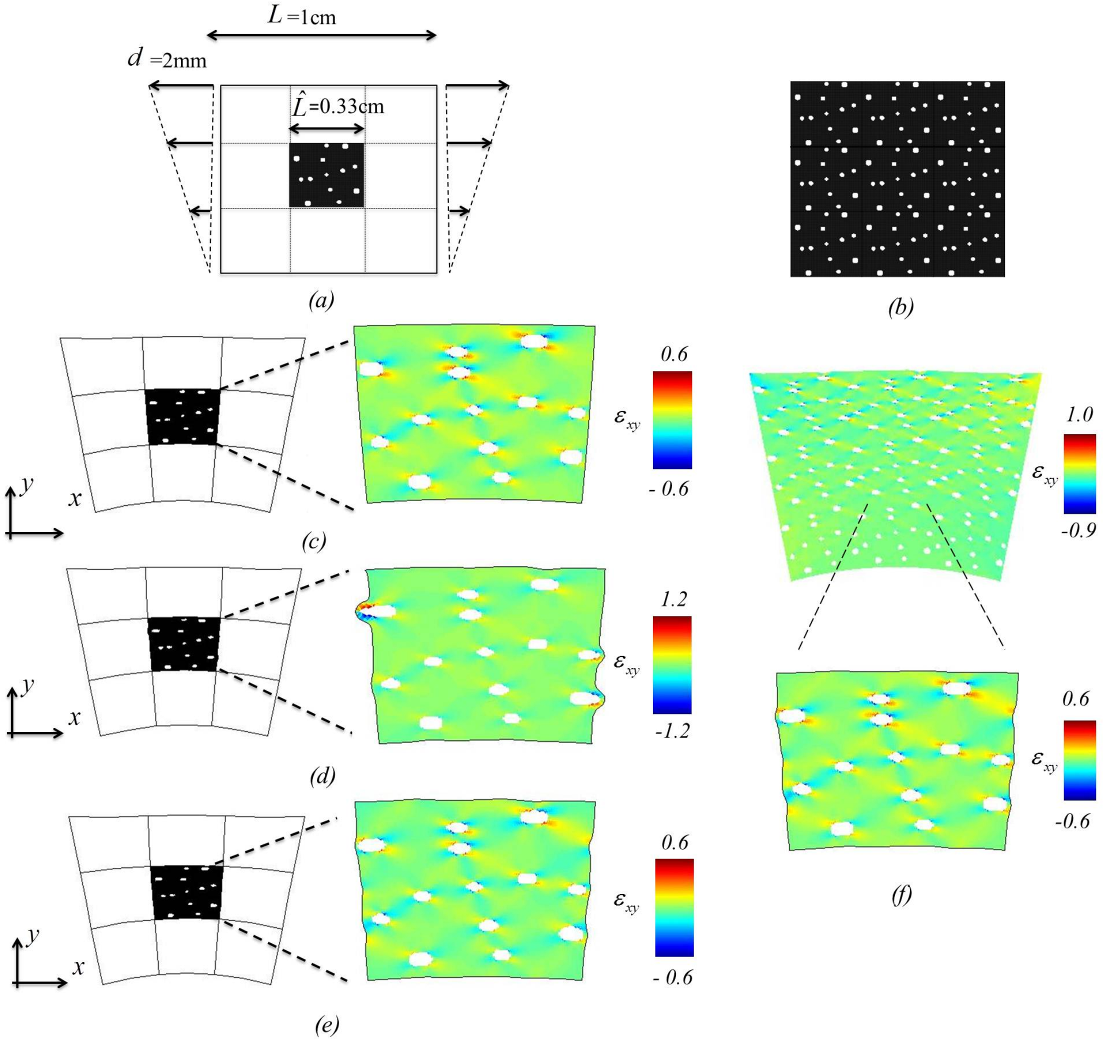

Figure 2.7: *(a) Single RVE embedded in a continuum region (b) brute force approach (c) strong displacement coupling, (d) weak displacement coupling and (e) quasi-periodic boundary coupling (f) shear strain field obtained from brute force approach.*

bending modes. This implies that the norm of the second displacement gradients $||\nabla\nabla\mathbf{u}||$ is not negligible and first-order theory cannot accurately describe the mechanical response of the composite. In addition, we note that the type of micro-macro constraints have a strong effect on the fluctuating strain fields in the RVE. Strong displacement coupling tends to attenuate strain concentrations near the RVE boundary while the weak displacement coupling allow very large fluctuations. The term "quasi-periodic boundary coupling" is also justified in this example, as seen in Fig. 7, the microscopic displacement fields are periodic across the RVE, while the global RVE deformation is not. We note that the latter constraint provides a better estimation of micro-deformation, as it implicitly assumes that the adjacent macroscopic elements possess a microstructure with the same arrangement as that in the RVE. Furthermore, it is well known from traditional computational homogenization that periodic boundary conditions gives the best estimation of the material behavior. We therefore choose this type of coupling in the next examples. For further validation, we compared the strain fields obtained from these three micro-macro constraints with numerical results obtained from a "brute force" approach that consists of using a microstructural description in the entire macroscopic domain. This strategy is expected to be highly accurate but its computational cost is often relatively high, if not intractable, for large problems. As shown in Fig. 7f, the strain and deformation fields obtained from the brute force approach are in best agreement with results obtained after applying the quasi-periodic boundary coupling on the embedded RVE.

2.5.2 Example 2: Three-point bending test of a porous elastic beam

The next example illustrates how the combination of finite element adaptivity and the concept of embedded RVE provides an efficient and accurate method to describe problems that are sensitive to multiple length scales. We thus consider a rectangular beam, in plane stress conditions, of length L and thickness $L/3$ subjected to three-point bending conditions. More precisely, the beam is supported by two rigid supports of finite-length and subjected to a distributed vertical load p on its top (Fig. 8). At the microscopic level, the beam is then represented by a porous linear elastic microstructure represented by the RVE depicted on the right of Fig. 8, for which the matrix is made of rubber with Young's modulus $E = 10MPa$ and Poisson's ratio $\nu = 0.3$. continuum elements is obtained from first order computational homogenization. For this material, under the plane strain condition, the homogenized Young's modulus and Poisson's ratio are $E = 4.71MPa$ and $\nu = 0.338$, respectively.

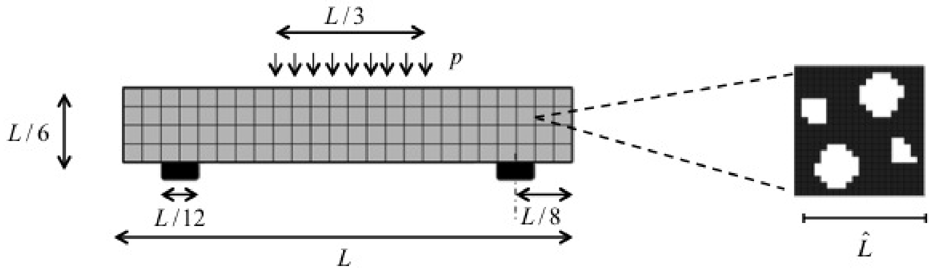

Figure 2.8: *Three point bending test. In this simulation,* $L = 6$ *and* $p = 100KN/m$

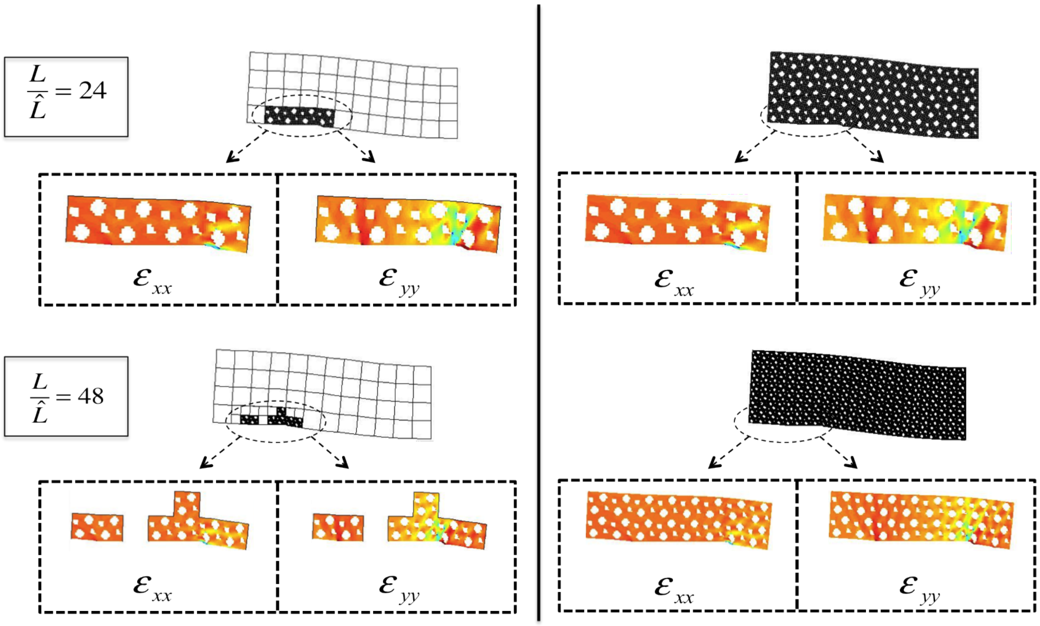

Figure 2.9: *Results comparison from microscale (left) and the brute force (right) approaches. Comparisons are provided for* $L/\hat{L} = 24$ *(top) and* $L/\hat{L} = 48$ *(bottom)*

This problem is of particular interest as the existence of fixed supports with sharp angles introduces a singular strain field in their neighborhood. This implies that continuum assumptions (for first-order model) are not valid in a small region surrounding the supports, which motivates the use of the proposed multiscale model. We particularly aim to assess the performance of the multiscale framework by measuring computational accuracy and cost for different ratios of material and macroscopic length-scales. On the one hand, cost is measured by the computational time for a specific simulation on a single CPU computer. On the other hand, accuracy is evaluated by comparing the local strain fields near the fixed supports to those predicted by a brute force approach.

In this context, Fig. 9 depicts simulation results of the half-beam deflection and the associated microscopic deformation near the support for different situations. In the first case, for a ratio $\hat{L}/L$ of the RVE size and the beam length equal to 24, as little as two levels of refinements are needed to converge to the final solution. The final solution shows that four RVEs are needed to accurately capture the microstropic strain fields near the supports and the comparison with strain fields computed from a brute force approach are excellent. In the second case, we considered a small microstructure, for which the ratio $\hat{L}/L$ is 48. Here, three levels of refinement were necessary to reach the final solution which displays seven RVEs split in two regions around the support's two corners. Once again, the local strain prediction from the multiscale method are showing very good agreement with those obtained from the brute force approach. Computational cost comparisons are then given in Fig. 10b for cases in which $L/\hat{L} = 12, 24, 48$ and 96, respectively. The graph clearly shows that gain in computation time increases drastically as the scale separation between the macroscopic problem and the microstructure becomes more pronounced. This saving is attributed to the fact that the multiscale method only needs an accurate description in critical regions (where large strain gradients exist). As a result, an accurate solution can be obtained for problems that show a very large scale separation such as shown in Fig. 10a in which $L/\hat{L} = 768$. In this case, the corresponding brute simulation was not tractable with a single CPU computer while a converged multiscale solution was obtained after seven stages of refinement.

2.5.3 Example 3: Stress concentration near a corner

The last example treats another classical elasticity problem that contains a singularity in its solution. Consider the square domain shown in Fig. 11a, subjected to a vertical distributed loading on its top and bottom boundaries. Assume that this solid is represented, at the microscale, by an elastic material that consists of a periodic distribution of small

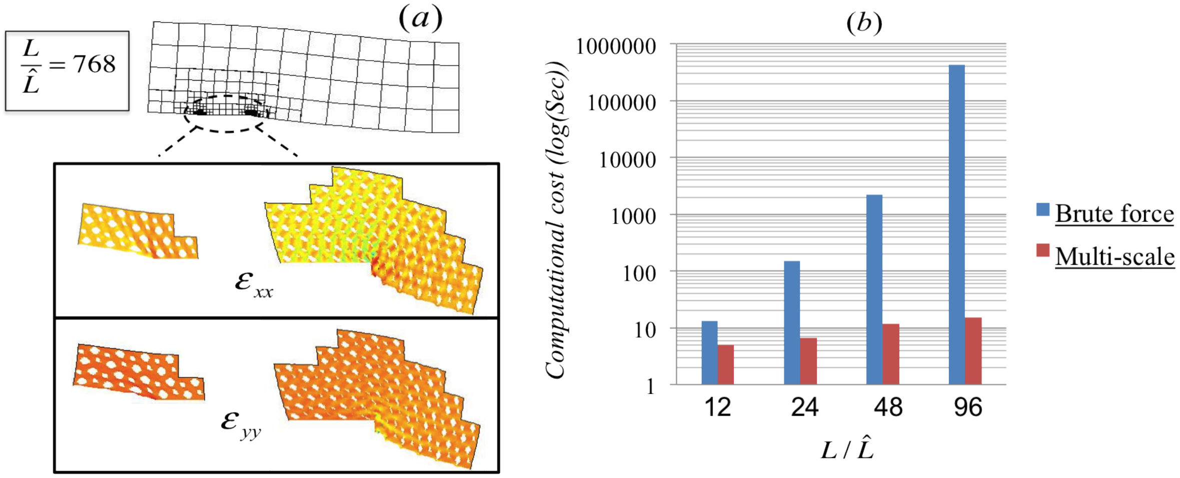

Figure 2.10: *(a) Beam deflection and microscopic strains in critical regions when* $L/\hat{L} = 768$ *in which the very large strain gradient near the support's angles is clearly visible. (b) Computational costs of the brute force and multiscale approaches for different values of* $L/\hat{L}$

square shaped voids of volume fraction 25 % . Material's elastic properties are the same as those used in the previous example. Using symmetry arguments, the domain is then reduced to a quarter of its size (Fig. 11b) with adequate displacement boundary conditions. The presence of a sharp corner induces increasingly large strain gradient as one approaches it; this implies that first continuum theories are limited in providing an accurate solution in this area. In Fig. 12, we present simulation results in the case where the size $\hat{L}$ of the

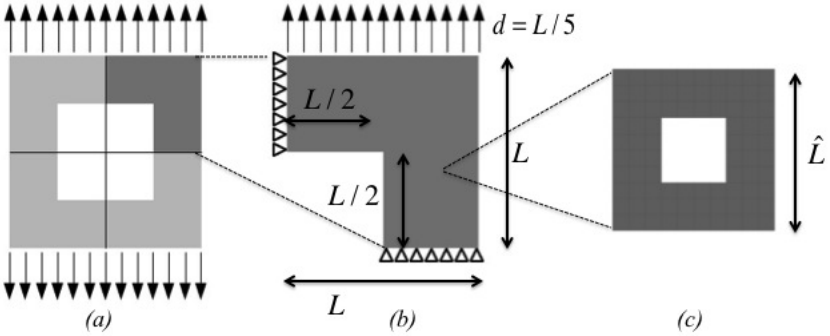

Figure 2.11: *(a) Original benchmark problem and its reduction using symmetry arguments (b). At the microscale, we consider a periodic microstructure represented by the RVE shown in (c)*

microstructure is 32 times and 2048 times smaller than the macroscale domain (represented by L), respectively. For both cases, we start from an initial mesh that comprises three square elements of size $L/2$. As expected, since the solution exhibits large strain gradients near the corner, adaptive refinement occurs in this region. When the size of element is equal to $\hat{L}$, RVEs are naturally embedded in the macroscale, leading to the microscale regions shown in the figure.

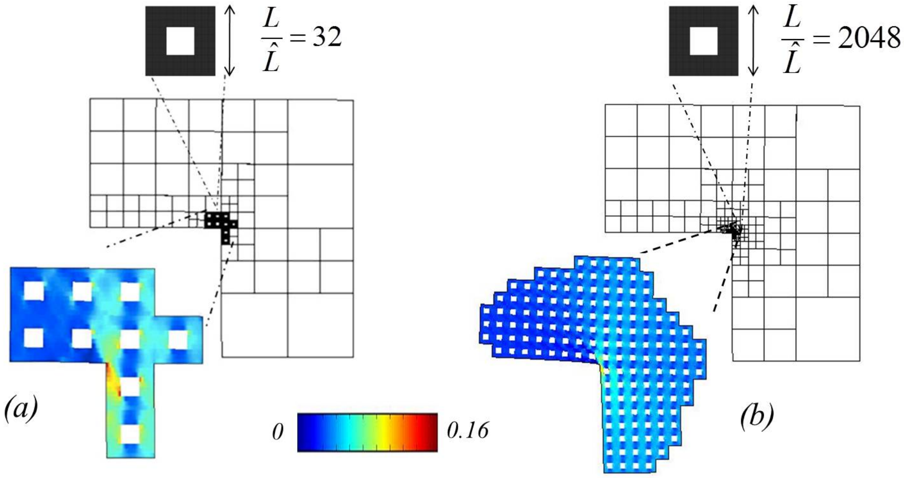

Figure 2.12: ϵ_{xx} *over RVE elements for (a)* $L/\hat{L} = 32$ *(b)* $L/\hat{L} = 2048$.

Similarly to the previous example, we assessed the efficiency of the method by measuring computational time for different values of $L/\hat{L}$ ranging from 4 to 256 and compared it to brute force simulations when possible. Once again, the trend showed that brute force simulation time exponentially increases with $L/\hat{L}$ while the cost of the multiscale simulation remains affordable for very large values of $L/\hat{L}$. We also assessed accuracy by computing a local strain value near the corner (see Fig. 13) with both brute force and the multiscale method. As shown in Fig. 14, we obtained an excellent match between the two solutions, confirming that accuracy is maintained despite the lower computational cost.

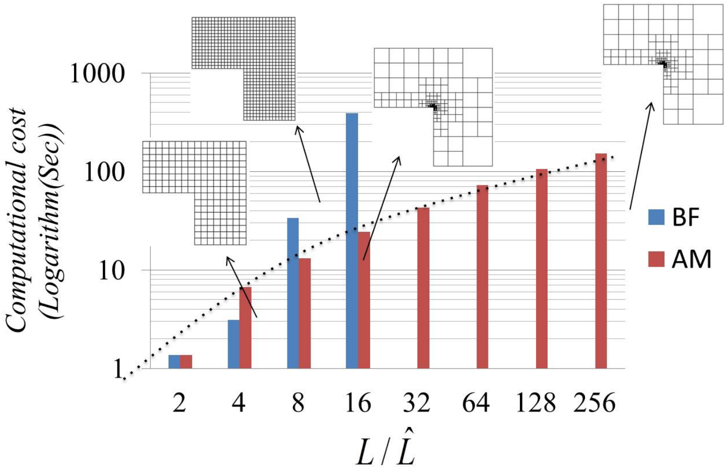

Figure 2.13: *Comparison between Brute Force approach (BF) and Adaptive Multiscale method (AM) computational cost.*

2.6 Summary and perspectives

In summary, this paper introduced an adaptive multiscale framework that is based on the following idea. The reduction of discretization error by adaptive refinement may lead to a situation in which element size become comparable to the microstructure length-scale (or RVE size). In this condition, we showed that the solution induces a finite homogenization error that tends to increase as refinement proceeds. Based on this concept, we introduced an adaptive concurrent multiscale method in which below a certain size, continuum elements are replaced by explicit RVEs. In this context, we derived a set of bridging scale conditions, consistent with traditional homogenization theory that naturally enable RVE to coexist with surrounding larger continuum elements. By adequately combining the concept of adaptive refinement and that of embedded RVEs, we then introduced a flexible concurrent multiscale framwork in which one can obtain optimal macroscale and microscale accuracy with minimal computational cost.

Although the efficiency of the method was demonstrated with several examples, it still, at this point, suffers from few limitations. First, due to their inherent periodicity, RVEs must originally possess a rectangular shape, which in turn enforces that the macroscopic finite element mesh should be regular and rectangular. While this feature is usually not convenient when modeling domains that possess curved boundaries and internal interfaces, this limitation can be addressed by invoking flexible formulations that describe interfaces independent from discretization. An example of such a formulation is provided by the extended finite element method [33]. Second, the present work focussed on the case of small deformation, linear elastic problems, which is usually restrictive for most real-life applications. In fact, the proposed framework can naturally be extended to describe nonlinear material behaviors and finite strains, such as observed during plastic deformation, damage and fracture [186, 27]. In particular, the adaptive multiscale method provides an ideal platform on which to study the phenomenon of ductile fracture, in which large scale features and local deformation mechanisms in the process zone must be modeled with maximum precision [188, 187]. The potential of the method is therefore significant as it will, by enabling simulations of ductile fracture at multiple scales, relate macroscopic fracture toughness to the nature of a material's microstructures; this capability is crucial for the development of future high-toughness materials.

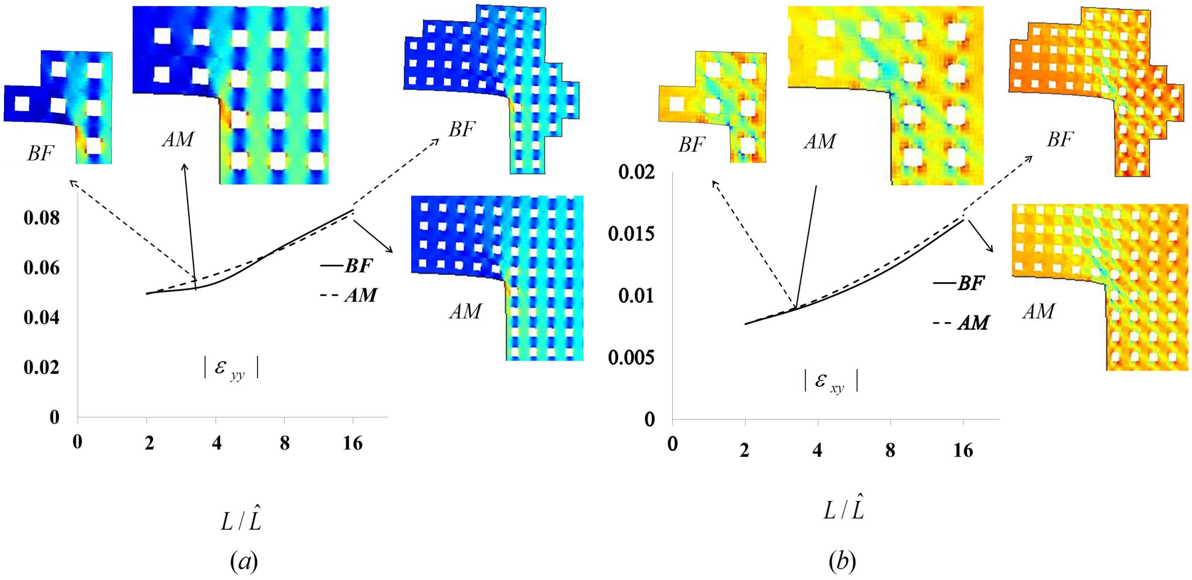

Figure 2.14: *Comparison between the brute force approach (BF) and the adaptive multiscale method (AM) accuracy for four different ratios of* $L/\hat{L}$. *Results are displayed for (a) the tensile strain in the y-direction (b) the shear strain.*

Chapter 3

An XFEM based multiscale approach to fracture of heterogeneous media

Mirmohammadreza Kabiri and Franck J. Vernerey
Department of Civil, Environmental and Architectural Engineering,
University of Colorado, Boulder, USA

3.1 abstract

This paper introduces a concurrent adaptive multiscale methodology in which both macroscopic and microscopic deformation fields strongly interact. The method is based on the balance between numerical and homogenization error; while the first type of error states that elements should be refined in regions of high deformation gradients, the second implies that elements size may not be smaller than a threshold determined by the size of the representative volume element (RVE). In this context, we introduce a multiscale method in which RVEs can be embedded in continuum region through appropriate macro-micro boundary coupling conditions. By combining the idea of adaptive refinement with the embedded RVE method, the methodology ensures that appropriate descriptions of the material are used adequately, regardless of the severity of deformations. We show that this method, in conjunction with the extended finite element method, is ideal to study the strong interactions between a crack and the microstructure of heterogeneous media. In particular, the method enables an explicit description of microstructural features near the crack tip while a computationally inexpensive coarse scale continuum description is used in the rest

of the domain. We illustrate the method with several examples showing its accuracy and relatively low computational cost and discuss its potential in relating microstructure to the fracture toughness of a diversity of heterogeneous media.

Keywords: *concurrent multiscale method, adaptive refinement, macro-micro coupling.*

3.2 Introduction

The relation between microstructural properties and material toughness plays a key role in designing stronger materials and predicting material failure. While quantifying this relation by experiment may prove challenging, theoretical and computational approaches are particularly useful in this regard. Many authors have been investigating this problem within the framework of homogenization theory [81, 70, 67, 68, 97, 155, 73], in which macroscopic material behavior is cast in terms of a constitutive relation derived by means of appropriate averaging over microstructural representative volume element (RVE). Higher order continuum theories such as micromorphic theories [188, 186, 187, 170, 71, 80], micro-continuum models [184, 181], Cosserat theory [135, 139, 148] or strain gradient theories [147, 146, 140] have been introduced by extending these formulations in order to make them capable of capturing size effects when inhomogeneous strains are present. However, when the inhomogeneity of macroscopic deformation is severe, it can be argued that the local microstructural response becomes more important than the homogenized material response. In this situation, coarse scale continuum theories fail to predict local material behavior and a microstructural description often becomes the most adequate strategy to assess the response. An obstacle to this strategy is, however, that microstructural descriptions are often not tractable over large (macro) computational domain. This challenge motivated the development of methods that aim at coupling microstructural material description (in regions with high heterogeneity of deformation) and continuum description of materials (where the deformation field is homogeneous and continuum theories are valid)[165, 154]. For instance, a class of concurrent multiscale methods [166, 156, 189, 132] was introduced based on the idea that a microscopic region can be determined a priori (such as around a crack tip) and can be coupled with a coarse grained continuum region. Using a similar idea, Ghosh et al. [150, 149, 160, 169, 168] introduced a method based on Voronoi Cell Finite Element Method (VCFEM) to deal with problems in which the micro region can not be defined a priori and is determined by adaptively refining the description in critical regions.

In a previous study [185] we introduced a novel adaptive concurrent multiscale method, based on the idea that modeling error, arising from two sources, should be minimized. The first source of error, known as discretization error, is defined as the difference between computational and exact solutions. The second type arises from imprecision in continuum assumptions and is known as the homogenization error. While the first type of error decreases with mesh refinement, it can be shown that at a certain point, further decrease of element size cause a significant rise in homogenization error. This argument is based on the fact that continuum description is only valid as long as the element size is larger than a critical size, which is based on the characteristic length scale of the material's microstructure. In this context, the proposed method aims at replacing continuum elements of critical size with a microscopic description of material in the form of RVE. In this way, the method enables both continuum and explicit microstructural descriptions to coexist within a single simulation. In addition, since a coarse continuum description is only used for regions of homogeneous deformations, the method ensures a low computational cost and provides highly accurate results in regions of heterogeneous deformation without violating the fundamental assumptions of continuum theories.

In the present work, we take advantage of the Extended Finite Element Method (XFEM) and extend the above formulation in order to obtain a multiscale solution for elasticity problems containing displacement discontinuities such as cracks in heterogeneous media. In next section we summarize the adaptive concurrent multiscale method and provide a brief description of error analysis and the method for bridging continuum and microstructural descriptions. Section 3 then provides a reformulation of the methodology in conjunction with the XFEM framework, which allows us to consider the problem of fracture in heterogeneous media. A few examples are then investigated in section 5 before a discussion and suggestions for future studies are given in section 6.

3.3 General adaptive multiscale methodology

Two basic attributes of multiscale methodologies are to preserve low computational cost while predicting accurate material behavior in regions of highly localized strain. In the finite element framework, low computational cost can typically be obtained via local mesh refinement. Such a strategy may, however, introduce significant modeling error as the element size reaches critical value. In such a situation, continuum elements may typically be replaced by an explicit microstructural description of material [185]. The ideas underlying the concept are discussed next.

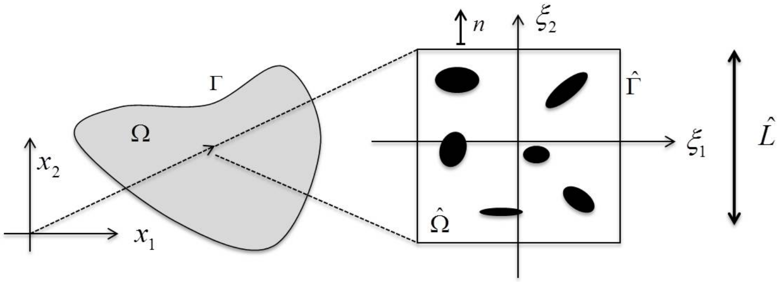

Figure 3.1: *Continuum macro structure and heterogeneous micro structure of a point* $\mathbf{x}$.

3.3.1 Discretization and homogenization error

3.3.1.1 Homogenization error

The fact that continuum theories are based on constitutive relations that are driven from homogenization poses a restriction on the size of continuum elements. The so-called homogenization error plays key role on this restriction. To illustrate this idea, let us consider a material domain Ω delimited by the boundary Γ and consider a material point $\mathbf{P}$

with coordinates $\mathbf{x}$ (Fig. 3.1). The macroscopic state of the material in this point can then be quantified by quantities that are averaged over the representative volume element (RVE), including the displacement vector, $\boldsymbol{u}$, the strain tensor, $\boldsymbol{\varepsilon}$ and the stress tensor $\boldsymbol{\sigma}$. Considering the RVE as a square domain (Fig. 3.1) with side length $\hat{L}$, a non-dimensional Cartesian coordinate, $\boldsymbol{\xi}$, can be introduced to characerize the fluctuating microscopic displacement, strain and stress $\hat{\boldsymbol{u}}$, $\hat{\boldsymbol{\varepsilon}}$ and $\hat{\boldsymbol{\sigma}}$, respectively. The Hill-Mandel condition [87, 72] then states that the variation of macroscopic elastic energy can be written in terms of microscopic fields through the relation $\delta W = \langle \hat{\boldsymbol{\sigma}} : \delta \hat{\boldsymbol{\epsilon}} \rangle$ where $\langle \cdot \rangle$ denotes the average operation over the RVE. After performing a linear expansion of the microscopic strain field, it can be found that:

$$\delta W = \boldsymbol{\sigma} : \delta \boldsymbol{\varepsilon} + \boldsymbol{\tau} \vdots \left(\hat{L} \nabla \nabla \delta \mathbf{u} \right) + \langle \hat{\boldsymbol{\sigma}} : \hat{\nabla} \delta \mathbf{u}^f \rangle, \tag{3.1}$$

where $\boldsymbol{\tau} = \langle \hat{\boldsymbol{\sigma}} \otimes \boldsymbol{\xi} \rangle$ is the stress-couple, $\mathbf{u}^f$ is the micro fluctuating displacement field and $\hat{\nabla}$ is the gradient operator in the non-dimensional coordinate system. For a first order theory, only the first term in right-hand side is considered, and the second and third terms are assumed to be negligible. While the last term often vanishes by enforcing specific boundary conditions on the RVE (as seen later in this paper), first order theory assumes the following condition on the second term:

$$e_h = \hat{L} || \nabla \nabla \delta \mathbf{u} || << 1 \tag{3.2}$$

where $|| \cdot ||$ is the L_2 norm which is defined as $||\mathbf{u}|| = \sqrt{u_{i,j} u_{i,j}}$ in indicial notation. We call e_h as the "homogenization error" in the remaining of the paper.

3.3.1.2 Discretization error

Discretization error is commonly defined as the difference between numerical solution obtained by finite element discretization and an exact continuum solution. It is often suitable to define the discretization error, e_d over the element domain Ω_e as the second norm of difference between exact and numerical strain fields solutions. For simplicity, we opt to asses this type of error over a square element with side length h and in which a local coordinate

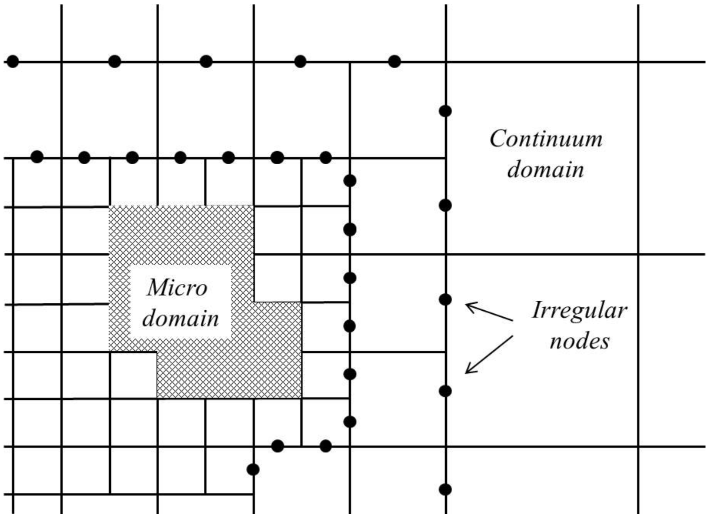

Figure 3.2: *Refined mesh with embedded RVEs. Irregular nodes appear on the borders of refined and unrefined elements.*

system $\bar{\mathbf{z}}$ can be introduced with origin at the geometrical center of the domain. Expanding the exact and numerical displacement field about $\bar{\mathbf{z}} = 0$, it can be shown that the error in displacement can be written [138, 96]:

$$u_i(\bar{\mathbf{z}}) - u_i^h(\bar{\mathbf{z}}) = \epsilon_i - \frac{1}{2} H_{ijk} \bar{z}_j \bar{z}_k, \tag{3.3}$$

where superscript h refers to the numerical solution, the error in the origin is defined as ϵ_i and H_{ijk} is a third order tensor interpreted as the second gradient of the exact displacement. Taking the norm of equation (3.3), one can obtain [96]:

$$e_d = hc||\nabla\nabla\mathbf{u}|| \tag{3.4}$$

where $c = 1/\sqrt{12}$ and $||\cdot||$ is the L_2 norm. Let us now take the two error definitions (3.2) and (3.4) as a vehicle to explain the key concept of our concurrent multiscale method. On the one hand, equation (3.4) states that for the discretization error to be less than e_d^{max}, the size of elements should verify $h < e_d/c||\nabla\nabla\mathbf{u}||$. On the other hand, since the homogenization error should be less than allowable tolerance, e_h^{max}, it can be shown that the refined element size, h, in the continuum region should satisfy:

$$h > \frac{e_d^{max}}{e_h^{max}} \hat{L}. \tag{3.5}$$

For instance, in the particular case where $e_d^{max} = e_h^{max}$, (3.5) implies that if the element size reaches to that of the RVE, subsequent refinement will induce a non-negligible homogenization error in the element. In this case, we argue that a continuum description is not appropriate and elements must be replaced by a finer, microstructural description provided by the RVE. The following section discusses various techniques to bridge microstructural and continuum descriptions when this situation arises.

3.3.2 Embedded RVE formulation

The previous section implies that continuum and microstructural descriptions often should coexist within a single simulation (Fig. 3.2). This can be done by introducing macro-micro kinematics, force conditions and appropriate boundary conditions at the boundary between these domains associated with two different descriptions. This can be done by introducing appropriate boundary conditions on the boundary between macro and micro domains which satisfies kinematic and force conditions on this boundary.

3.3.2.1 Macro-micro kinematics

Macro-micro compatibility conditions state that, in an average sense, the macro deformation of an individual element must conform with that of the RVE that replaces it. The strain in a continuum element $\langle \nabla \mathbf{u} \rangle^s$ is written in terms of nodal macro displacement vectors, $\mathbf{U}$ and the micro displacement fluctuation field, $\tilde{\mathbf{u}}$ as:

$$\langle \nabla \mathbf{u} \rangle^s = \sum_I \langle \mathbf{B}^I \rangle \mathbf{U}^I + \langle \nabla \tilde{\mathbf{u}} \rangle^s, \tag{3.6}$$

where a superscript s indicates the symmetric part of a tensor, the matrix $\mathbf{B}^I$ contains the gradient of element shape functions and $\langle \cdot \rangle$ is the average operator over domain $\hat{\Omega}$. Since the average deformation field of an element and RVE should conform, the second term in (3.6) vanishes and by using the divergence theorem, we obtain:

$$\langle \nabla \tilde{\mathbf{u}} \rangle = \frac{1}{|\hat{\Omega}|} \int_{\hat{\Gamma}} \tilde{\mathbf{u}} \otimes \mathbf{n} \, d\hat{\Omega} = 0, \tag{3.7}$$

where $\mathbf{n}$ is the unit normal vector to the boundary $\hat{\Gamma}$ of the RVE (Fig. 3.1). Equation (3.7) is known as kinematic coupling condition.

3.3.2.2 Force balance between macro and micro descriptions

In order to build conditions between nodal forces at continuum and microstructural descriptions, we write the variation of elastic energy as:

$$\delta W = \int_{\Omega} \boldsymbol{\sigma} : \delta \boldsymbol{\epsilon} d\hat{\Omega} = \int_{\Gamma} \mathbf{t} \cdot \delta \mathbf{u} d\hat{\Gamma} \tag{3.8}$$

Taking advantage from the fact that the elastic energy arising from fluctuating fields vanishes [155], it is straightforward to show that the variation in elastic energy becomes:

$$\delta W = \sum_{I} \mathbf{f}^{I} \cdot \delta \mathbf{U}^{I}, \tag{3.9}$$

where the macroscopic nodal forces are related to the traction forces $\hat{\mathbf{t}}$ on the macro-micro boundary by:

$$\mathbf{f}^{I} = \sum_{I} \int_{\hat{\Gamma}} N^{I} \tilde{\mathbf{t}} d\hat{\Gamma}. \tag{3.10}$$

Note that the distribution of surface traction $\hat{\mathbf{t}}$ over the RVE boundaries is dictated by the type of boundary conditions. While the variety of boundary conditions can be introduced (as discussed in [185]) , we here focus on the simplest of all, known as the strong displacement coupling. This type of boundary condition is written as:

$$\mathbf{u}(\boldsymbol{\xi}) = \sum_{I} N^{I}(\boldsymbol{\xi}) \mathbf{U}^{I}, \qquad \boldsymbol{\xi} \in \hat{\Gamma}. \tag{3.11}$$

in which N^{I} are the finite element shape functions. This set of boundary condition is formulated to strongly verify (3.7) by prescribing micro nodes on RVE edges to follows adjacent macro element's displacement.

3.4 XFEM based adaptive multiscale method

The XFEM was first introduced by Moës et al. [129] in order to avoid remeshing continuum domain for propagating crack. This method is based on enriching the ordinary finite element basis with singular functions, which covers the singular displacement field around the crack tip, and smooth Heaviside functions for elements along the crack surface. Based on this concept, we show how the above adaptive multiscale method can be naturally extended to predict materials behavior in the presence of the highly localized deformation fields near the tip of a crack.

3.4.1 Crack definition and numerical approximation using XFEM

In the context of XFEM, the geometry of a line discontinuity can be defined by the zero level of a level-set function ϕ. While this method was first used to model closed boundaries, Stolarska et al. [78] generalized it for the modeling of open boundaries such as cracks and open interfaces. In this formulation, a crack surface Γ_c is defined by two level set functions, specifying whether a point is below or above the crack and whether a point is in front or in the wake of the crack tip. The standard XFEM approximation of a function $u(\mathbf{x})$ over an element domain is then written as:

$$u(\mathbf{x}) = \sum_{I \in SI} N_I(\mathbf{x}) u_I + \sum_{I \in SI^{enr}} N_I(\mathbf{x}) \psi(\mathbf{x}) a_I, \tag{3.12}$$

in which the first term on the right hand-side is the standard finite element approximation and SI is the set of all the nodes in the element domain. The second term is the enriched part of approximation, with ψ be an appropriate enrichment function of node $I \in SI^{enr}$ and SI^{enr} is the enriched subset of I. Finally, u_I and a_I are the nodal coefficients of standard finite element and the enriched degrees of freedom. For split elements, the function ψ captures the discontinuity of the displacement field inside the element as:

$$\psi(\mathbf{x}) = H(\phi(\mathbf{x})) = \begin{cases} 0 & for \quad \phi(\mathbf{x}) \leq 0 \\ 1 & for \quad \phi(\mathbf{x}) > 0 \end{cases} \tag{3.13}$$

where H is the Heaviside function. In addition, to capture the singular strain field around the crack tip, four different enrichment functions are used on each node of the crack tip element, which are:

$$\psi(r,\theta) = \left\{ \sqrt{r}sin(\frac{\theta}{2}),\ \sqrt{r}cos(\frac{\theta}{2}),\ \sqrt{r}sin(\theta)sin(\frac{\theta}{2}),\ \sqrt{r}sin(\theta)cos(\frac{\theta}{2}), \right\} \tag{3.14}$$

where r is the distance of the point to the crack tip and θ is the angle between the tangent to the crack tip and the line that connects the point $\mathbf{x}$ to the crack tip. It should be noted that for $\theta = \pm\pi$, the first term in (3.14) also captures the discontinuity in the displacement field along the crack surface in the element.

3.4.2 Error and refinement

Error and refinement criteria follows a similar approach as that described in section 2, with the difference that the element are now characterized with additional degrees of freedom when split by a crack. The calculation of the discretization error is then performed by using 9-node quadrilateral elements in which second gradients of displacement are calculated as follows:

$$\nabla\nabla\mathbf{u}(\mathbf{x}) = \sum_{I=1}^{9} \mathbf{G}_I(\mathbf{x})\mathbf{u}_I + \sum_{I=1}^{n^{enr}} \mathbf{G}_I^{enr}(\mathbf{x})\mathbf{a}_I. \tag{3.15}$$

Here, $\mathbf{u}_I$ and $\mathbf{a}_I$ are respectively the nodal displacement and the nodal enrichment vectors and n^{enr} is the number of enriched nodes in element. $\mathbf{G}$ and $\mathbf{G}^{enr}$ are the second derivative of the finite element and XFEM shape functions defined by:

$$\mathbf{G}_I(\mathbf{x}) = \begin{bmatrix} \frac{\partial^2 N_I(\mathbf{x})}{\partial x^2} & \frac{\partial^2 N_I(\mathbf{x})}{\partial y^2} & \frac{\partial^2 N_I(\mathbf{x})}{\partial x \partial y} & 0 & 0 & 0 \\ 0 & 0 & 0 & \frac{\partial^2 N_I(\mathbf{x})}{\partial x^2} & \frac{\partial^2 N_I(\mathbf{x})}{\partial y^2} & \frac{\partial^2 N_I(\mathbf{x})}{\partial x \partial y} \end{bmatrix}^T . \tag{3.16}$$

$$\mathbf{G}_I^{enr}(\mathbf{x}) = \begin{bmatrix} \frac{\partial^2 N_I^{enr}(\mathbf{x})}{\partial x^2} & \frac{\partial^2 N_I^{enr}(\mathbf{x})}{\partial y^2} & \frac{\partial^2 N_I^{enr}(\mathbf{x})}{\partial x \partial y} & 0 & 0 & 0 \\ 0 & 0 & 0 & \frac{\partial^2 N_I^{enr}(\mathbf{x})}{\partial x^2} & \frac{\partial^2 N_I^{enr}(\mathbf{x})}{\partial y^2} & \frac{\partial^2 N_I^{enr}(\mathbf{x})}{\partial x \partial y} \end{bmatrix}^T . \tag{3.17}$$

Note that due to the singular strain fields near the crack tip strain gradients, and thus the discretization error become infinite at the tip. This implies that the element containing the crack tip is always subjected to refinement, which indicates that (3.15) need not to be calculated for tip elements. However, for split elements (3.17) is written as:

$$\frac{\partial N_I^{enr}(\mathbf{x})}{\partial x_i} = \frac{\partial N_I(\mathbf{x})}{\partial x_i} \left(H(\phi_1(\mathbf{x})) - H(\phi_1(\mathbf{x}_I)) \right) + N_I(\mathbf{x}) \delta \left(\phi_1(\mathbf{x}) \right), \tag{3.18}$$

where δ is the Dirac-delta function and ϕ_1 is the signed distance function from the crack surface, Γ_c. The second term in (3.18) vanishes over the element but takes an infinite value on the crack surface. Since the methodology is based on decreasing the discretization error within the continuum region, this term is not considered in the error evaluation Accordingly the second gradient of shape functions can be written as:

$$\frac{\partial^2 N_I^{enr}(\mathbf{x})}{\partial x_i \partial x_j} = \frac{\partial^2 N_I(\mathbf{x})}{\partial x_i \partial x_j} \left(H(\phi_1(\mathbf{x})) - H(\phi_1(\mathbf{x}_I)) \right). \tag{3.19}$$

The L2 norm of displacement defined in (3.4) is then written as:

$$\begin{aligned} \|\nabla \nabla \mathbf{u}(\mathbf{x})\|_2 &= \left(\sum_{I=1}^{9} (\mathbf{u}_I)^T \left(\int_{\Omega} (\mathbf{G}_I(\mathbf{x}))^T \mathbf{G}_I(\mathbf{x}) d\Omega \right) \mathbf{u}_I \right)^{1/2} + \\ & \left(\sum_{I=1}^{9} (\mathbf{a}_I)^T \left(\int_{\Omega - \Gamma_c} (\mathbf{G}_I^{enr}(\mathbf{x}))^T \mathbf{G}_I^{enr}(\mathbf{x}) d\Omega \right) \mathbf{a}_I \right)^{1/2} . \end{aligned} \tag{3.20}$$

For a split element, (3.20) takes a different value on the two subdomains separated by the crack. In this study, the largest of the two value is used as the discretization error measure of the element. The local mesh refinement then consists of dividing elements into four sub elements, an operation that usually introduces irregular nodes on the edge of surrounding non-refined elements (Fig. 3.2). Following the method introduced in [65] this irregularity is addressed through the definition of new sets of shape functions that enable a smooth transition of continuum fields between element while satisfying the conformity of displacement as well as the partition of unity.

3.4.3 Embedded RVE formulation in XFEM framework

Let us now discuss the issue of the bridging scale method between macroscale and microstructural descriptions in the XFEM framework.

3.4.3.1 Kinematics of macro-micro coupling

We first consider that the RVE is a computational domain that can be superimposed on a continuum (macro) element. The micro displacement fields in the RVE can be written in terms of nodal displacement vector $\mathbf{U}$, the enriched nodal value vector of $\mathbf{a}$ and the micro fluctuation field $\tilde{\mathbf{u}}^f$ as:

$$\tilde{\mathbf{u}}(\boldsymbol{\xi}) = \sum_{i\in I} N_i(\boldsymbol{\xi})\mathbf{U}_i + \sum_{i\in I^{enr}} N_i^{enr}(\boldsymbol{\xi})\mathbf{a}_i + \tilde{\mathbf{u}}^f(\boldsymbol{\xi}). \tag{3.21}$$

The gradient of micro displacement is then:

$$\nabla\tilde{\mathbf{u}}(\boldsymbol{\xi}) = \sum_{i\in I} \mathbf{B}_i(\boldsymbol{\xi})\mathbf{U}_i + \sum_{i\in I^{enr}} \mathbf{B}_i^{enr}(\boldsymbol{\xi})\mathbf{a}_i + \nabla\tilde{\mathbf{u}}^f(\boldsymbol{\xi}), \tag{3.22}$$

where ∇ is the differential operator with respect to $\boldsymbol{\xi}$ while $\mathbf{B}$ and $\mathbf{B}^{enr}$ denote the gradient of regular and enriched shape functions, respectively. In order to substitute a continuum element by an RVE, the macro-micro kinematic conditions dictate that "in average" the deformation of the RVE is equal to that of the macro element. One can therefore write the average displacement field of micro displacement as:

$$\left\langle \nabla\tilde{\mathbf{u}} \right\rangle = \sum_{i\in I} \left\langle \mathbf{B}_i \right\rangle \mathbf{U}_i + \sum_{i\in I^{enr}} \left\langle \mathbf{B}_i^{enr} \right\rangle \mathbf{a}_i + \left\langle \nabla\tilde{\mathbf{u}}^f \right\rangle, \tag{3.23}$$

where $\langle\cdot\rangle$ is the average operator over the element. For a macro element the average displacement is defined by first two terms in the right hand side of (3.23) which means $\left\langle \nabla\tilde{\mathbf{u}}^f \right\rangle$ should vanish over the element. Using the divergence theorem it can be shown that (3.7) again verifies the macro-micro kinematic condition. By taking similar arguments as in section 3.3.2.2, one can show the validity of (3.9). However, it should be noted that since the XFEM shape functions vanish on the edges of elements, no enriched counterpart of micro traction distribution appears in the definition of macroscopic force.

3.4.3.2 Macro-micro coupling assumption

A simple way of verifying (3.7) is to impose a condition that leads to zero fluctuation field along the RVE boundaries. This, in other words implies that $\tilde{\mathbf{u}} = 0$ on the border between micro and macro domains. This is equilvalent to write:

$$\mathbf{u}(\boldsymbol{\xi}) = \sum_{i \in I} N_i(\boldsymbol{\xi})\mathbf{U}_i + \sum_{i \in I^{enr}} N_i^{enr}(\boldsymbol{\xi})\mathbf{a}_i \qquad \boldsymbol{\xi} \in \hat{\Gamma}, \tag{3.24}$$

on a boundary $\hat{\Gamma}$ of an RVE. This equation is similar as (3.11) in with additional terms appear to account for the contribution of the discontinuous part of the solution at the macroscopic level. Similar to the strong coupling introduced previously, this type of condition strongly enforces the micro-nodes to follow the macroscopic displacement field variation on the macro-micro boundary. Figure 3.3 schematically depicts the distributions of macroscopic and microscopic displacements along the macro-micro boundary in two different cases.

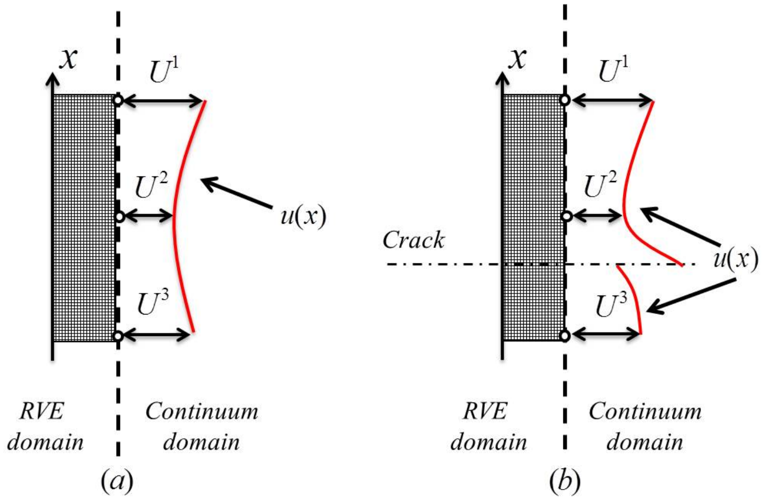

Figure 3.3: *Representation of macro-micro boundary coupling constraints; (a) without crack (b) when a crack is present.*

3.5 Computational aspects

In this section, we introduce the multiple scale algorithm that combines adaptive refinement and embedded RVE. The algorithm of methodology is shown in Fig. 3.4. It should be noted that in this work, an incremental approach is taken but we do not consider crack propagation. Furthermore, from a numerical view point, the constraints introduced in section

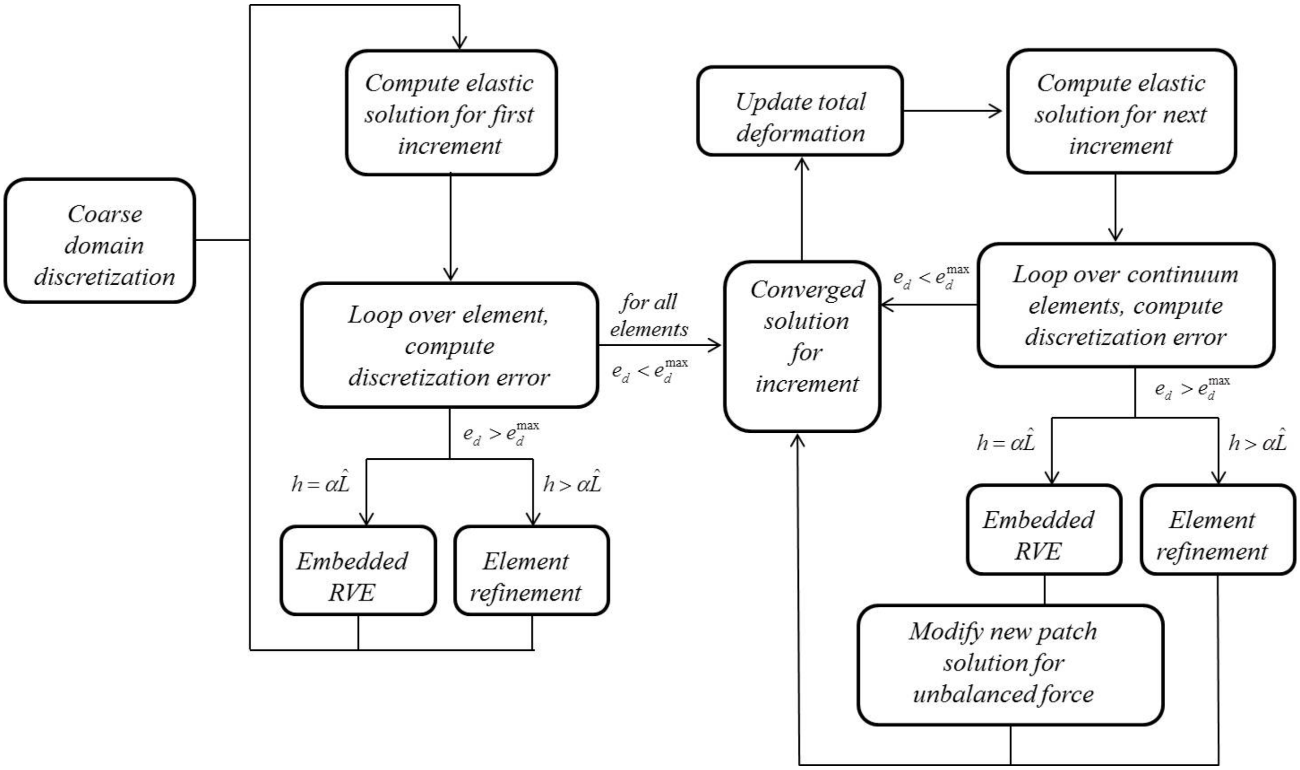

Figure 3.4: *Algorithm of the method.*

3.4.3.2 can be enforced by the Lagrange Multipliers Method. Typically, at every microscopic node on the edge $\hat{\Gamma}$, a pair of constraints are defined as:

$$\mathbf{c}_n = \mathbf{u}_n - \sum_{i \in I_{\hat{\Gamma}}} N_i(\boldsymbol{\xi}_n)\mathbf{U}_i - \sum_{i \in I_{\hat{\Gamma}}^{enr}} N_i^{enr}(\boldsymbol{\xi}_n)\mathbf{a}_i, \tag{3.25}$$

where $I_{\hat{\Gamma}}$ is the set of nodes on boundary, $I_{\hat{\Gamma}}^{enr}$ is the enriched set of nodes on the boundary and n is the micro-nodes number which varies from 1 to the total number of micro-nodes on boundaries of RVEs (N^m). In this method, each constraint equation c_n is associated with a Lagrange multiplier λ_n which can be interpreted as the microscopic tractions on the boundaries of RVE. The objective of the method is then to solve the linear system of equation

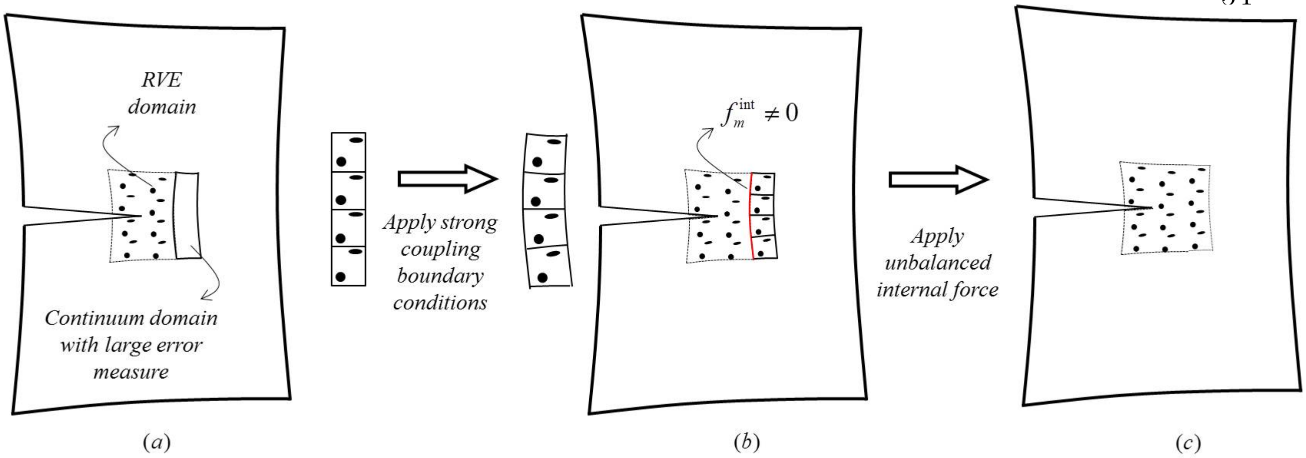

Figure 3.5: *Procedure involved in substituting macro elements by RVEs during incremental loading, (a) Continuum elements with high error measure, (b) Internal force on the border between two patches of RVEs is not balanced, (c) Final equilibrium is obtained solving* $\mathbf{K}_m\mathbf{u_m} = -\mathbf{f}_m^{int}$.

of the form:

$$\begin{bmatrix} \mathbf{K}_M & \mathbf{0} & \mathbf{I}_{Mm}^{\mathbf{T}} \\ \mathbf{0} & \mathbf{K}_m & \mathbf{I}_{mM}^{\mathbf{T}} \\ \mathbf{I}_{Mm} & \mathbf{I}_{mM} & \mathbf{0} \end{bmatrix} \begin{bmatrix} \delta\mathbf{u}_M \\ \delta\mathbf{u}_m \\ \boldsymbol{\lambda} \end{bmatrix} = \begin{bmatrix} \delta\mathbf{f}_M \\ \delta\mathbf{f}_m \\ \mathbf{c} \end{bmatrix}, \tag{3.26}$$

in which $\mathbf{K}_M$ is the stiffness matrix associated with continuum degrees of freedom (including standard and enriched degrees of freedom) while $\mathbf{K}_m$ is the stiffness matrix associated with microscopic nodal degrees of freedom. Similarly, $\delta\mathbf{u}_M$ and $\delta\mathbf{f}_M$ are respectively, the incremental displacement and force vectors, associated with standard and enriched continuum degrees of freedom and $\delta\mathbf{u}_m$ and $\delta\mathbf{f}_m$ are the incremental microscopic displacement and force vectors. The vector $\boldsymbol{\lambda}$ represents the Lagrange multipliers that enforces the constraints $\mathbf{c} = 0$. Note that the global stiffness matrix is decomposed in two different parts, namely macro and micro degrees of freedom. Interactions between these two components appear through the interaction matrices, $\mathbf{I}_{Mm}$ and $\mathbf{I}_{mM}$ defined as the derivatives of the constraints with respect to macro and micro displacements.

On the final note, we wish to discuss some important points pertaining to the incremental refinement procedure. For this, let us consider that after N load increments, a particular element e (in a deformed state) is characterized with a large computational error (both discretization and homogenization) and must undergo a transition to the RVE description. A challenge in this situation is that the embedded RVE must be inserted in a deformed state. This issue may be addressed in the following manner: First, the nodal displacements of the macro element are extracted and imposed on the RVE, independently of the global simulation. A macroscopically conforming RVE deformation can then be obtained through the strong coupling boundary condition developed in 3.4.3.2. This deformed RVE may then substitute the continuum element, as part of the refinement procedure. While the displacements are conforming, we note that this operation introduces unbalanced internal forces, $\mathbf{f}_m^{int}$, on the border between the new patch of RVEs and patch of RVEs before refinement (as shown in Fig. 3.5b). These forces, however vanish after solving the global force equilibrium $\mathbf{K}_m\mathbf{u_m} = -\mathbf{f}_m^{int}$. This procedure is shown schematically in Fig. 3.5.

A similar problem arise when deformed split elements have to be divided into four subdomains. In this case, it is particularly useful to establish the relation between enriched degrees of freedom, $\mathbf{a}$, and the crack opening δ_c in the RVE through the formula:

$$\delta_c = \sum_{i=1}^{9} N_i a_i, \tag{3.27}$$

where δ_c is the crack opening, N_i are the standard finite element shape functions and a_i are the values of enriched degrees of freedom. As shown in Fig. 3.6 and based on (4.21), values of new enriched degrees of freedom can be obtained by interpolating enriched degrees of freedom in larger element.

3.6 Numerical examples

We now aim to illustrate the method by considering two examples focusing on the problem of fracture of heterogeneous media in the elastic regime. We concentrate on a particular type of foam-like material in which the microstructure consists of micro-truss

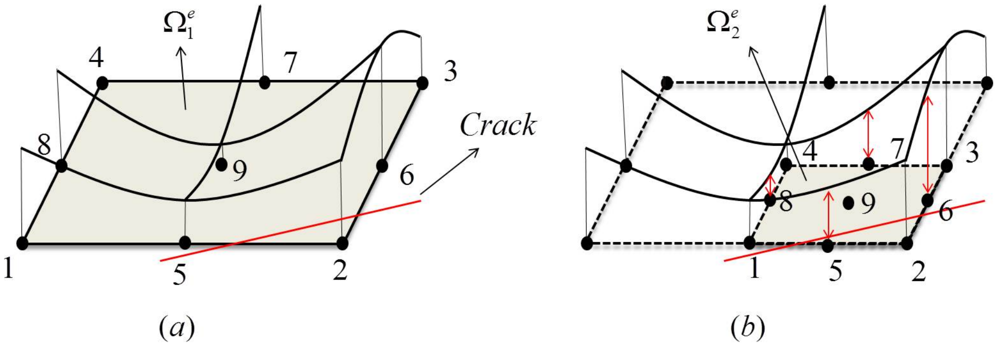

Figure 3.6: *(a) Variation of nodal enrichment values over split element and (b) variation of nodal enrichment values over refined element.*

structure with characteristic length of $\hat{L}$ as depicted in Fig. 3.7b.

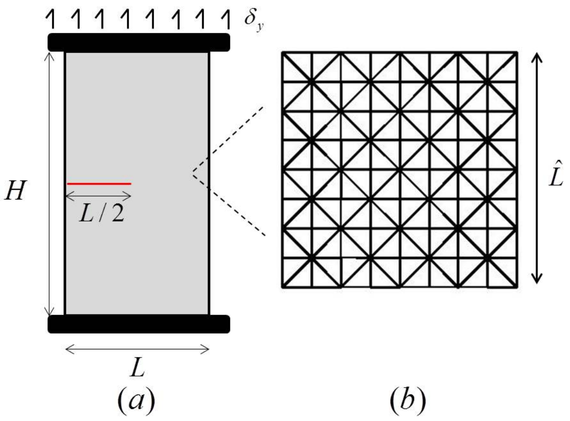

Figure 3.7: *(a) Plate with an edge crack under mode I loading. In this problem the initial finite element mesh consists of square elements of size* $h = 0.25L$ *and* $L = 3$, $H = 5.5$, $\delta_y = 0.1$ *and (b) microstructure RVE.*

Example 1: Edge crack under mode I loading

In the first example, we aim to show how combining the adaptive multiscale approach and the XFEM leads to an effective and accurate method to describe the fracture behavior of material at multiple length scales. We consider the classical fracture mechanics problem that consists of a rectangular plate of size $L \times H$ with a preexisting edge crack under mode I loading in plane strain condition. For all simulation, we start from a very coarse initial mesh that is refined until both discretization and homogenization errors are below the acceptable criterion. The boundary conditions consist of fixed vertical displacements on the bottom of the plate while an incremental vertical displacement is imposed on the top boundary via 5 increments of $0.02L$. At the microscopic level, truss elements have a Young's modulus $E = 0.1Mpa$ and a cross sectional area $A = 0.01L_t$ where L_t is the length of a truss. The RVE (of size $\hat{L}$) shown in Fig. 3.8 illustrates the truss layout in the microstructure. At the micro scale, the crack is defined by a levelset function and the Heaviside enrichment function described in Sec. 3.4.1. The crack at this length scale is accounted by deleting trusses whenever they intersect with the crack path. The linear elastic constitutive relation at the continuum level is obtained by a priori performing RVE based first order computational homogenization as described in [186]. Briefly, the method consists of subjecting the RVE to three different modes of deformation and deriving the corresponding average traction forces on the RVE boundary. These forces are then used to obtain the continuum stress via a proper averaging operation; this enable the determination of the linear elastic matrix used at the continuum level. Based on linear elastic fracture mechanics (LEFM) solution, the strain field in the vicinity of the crack tip is singular. This means that continuum assumptions for heterogeneous media are not valid in this region and an explicit microstructural description is necessary. In addition, since the boundary conditions are applied in an incremental manner, the size of the process zone grows as the applied displacement increases. In this context, the results for two different ratio of $L/\hat{L}$ are shown in Fig. 3.8. For each simulation, the vertical strain field, ε_{yy}, is depicted at the end of third and fifth load increments. For the case where, $L/\hat{L} = 32$ three levels of refinement are necessary to obtain a converged solution. In the case where the ratio $L/\hat{L}$ is 512, six levels of refinement are necessary. It should be noted that in the second situation, as the number of increment increases from three to five, the number of RVEs in the vicinity of the crack tip increases such that the RVE patch defines the crack process zone. This does not occur in the first case since RVEs occupy a larger region in front of the crack tip.

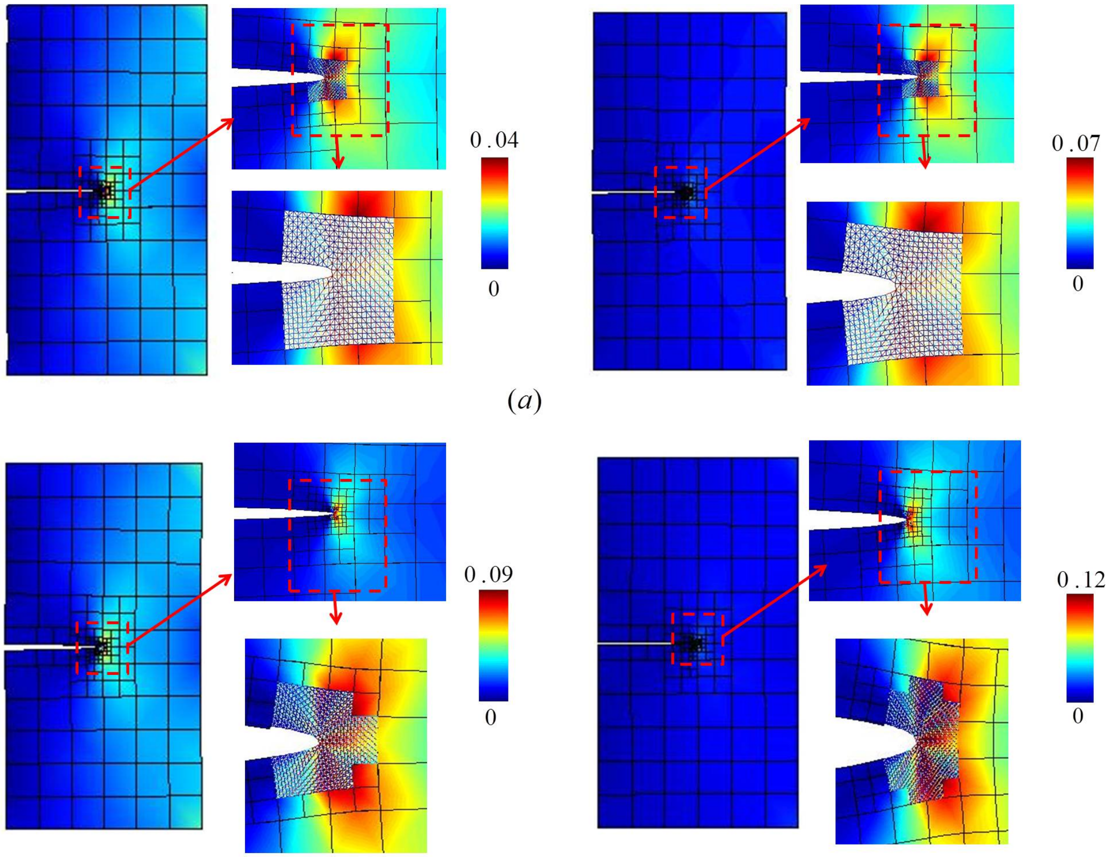

(*a*)

(*b*)

Figure 3.8: ε_{yy} *at the end of load increment 3(left) and 5(right) for two different cases of (a)* $L/\hat{L} = 32$ *and (b)* $L/\hat{L} = 512$.

Since in practice crack propagation in foam materials is initiated by the rupture of truss elements at the micro-scale, we illustrate the accuracy of the method by comparing the maximum tensile strain in the micro elements obtained from our method and those obtained from a "brute force" computational approach. In the latter, a microstructural material representation (micro-truss elements) is used for the entire computational domain. Fig. 3.10 shows an excellent agreement between the two simulations, which confirms the adequacy of macro-micro conditions at the edge of RVEs. To show the efficiency of the method, we also compared the total computational time needed for both methods on a single CPU machine. As shown in Fig 3.9 the difference between computational costs of the two approaches increase

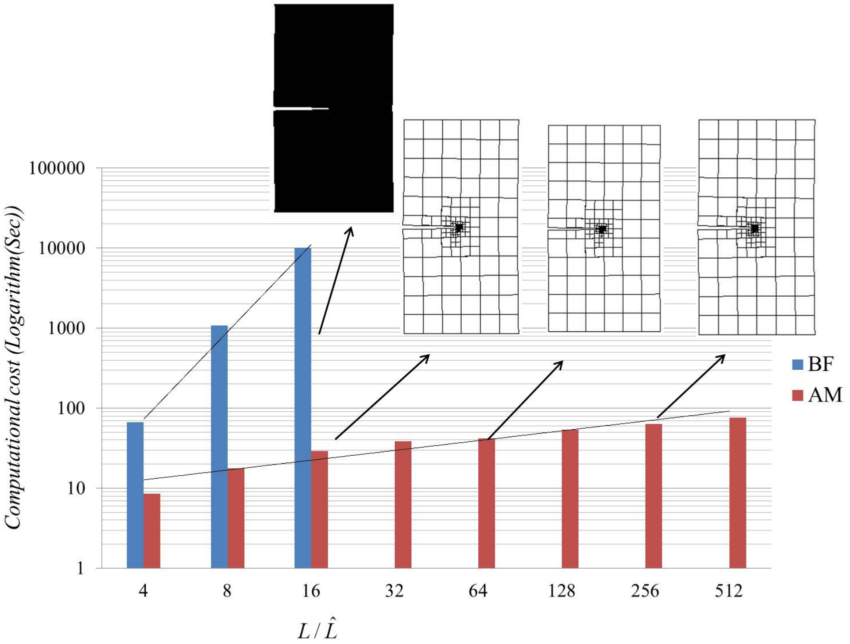

Figure 3.9: *Computational cost for brute force and multiscale approaches.*

drastically as the microstructural size decreases to the ratio $L/\hat{L}$ of 16, after which the brute force analysis is no longer tractable.

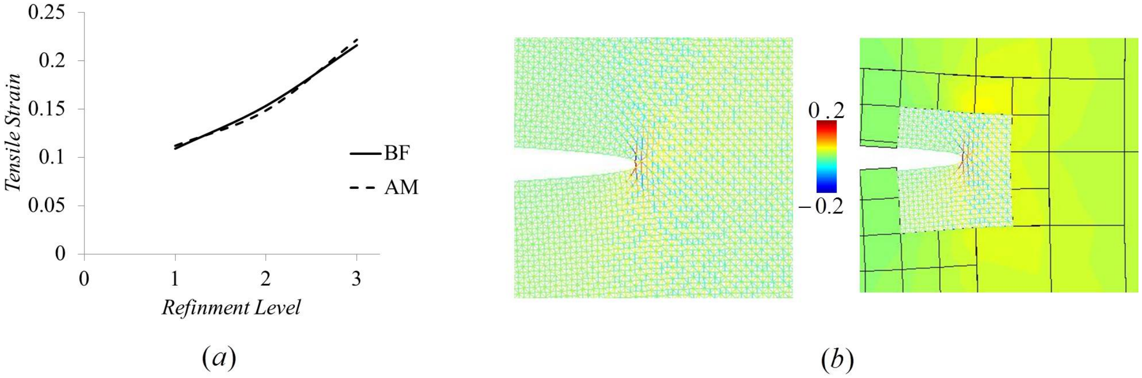

Figure 3.10: *(a) maximum tensile strain comparison (b) Strain in micro elements for brute force simulation (left) and multiscale simulation (right) for* $L/\hat{L} = 16$.

Example 2: Inclined crack under mixed mode loading condition

In the second example, we consider another classical LEFM problem that consists of a plate containing an inclined edge crack, and subjected to mixed mode boundary conditions as depicted in Fig. 3.11a. The material properties and domain dimensions are the same as in the previous example and it is assumed that the truss microstructure contains a periodic distribution of voids (of volume fraction 45%) as shown in Fig. 3.11b. The initial mesh is comprised of 6×22 elements of size $L/12$. Refinement is performed in the vicinity of crack tip, where the singular strain field exists, up to the level in that the smallest element size is equal to the RVE size, $\hat{L}$. The simulation is performed for $L/\hat{L} = 128$ requiring five levels of refinements. The horizontal strain fields, ε_{xx} in the macroscopic domain at the end of second and fourth load increments are shown in Fig. 3.12. It should be noted that due to the presence of crack, the strain range in the microscopic truss elements are drastically different than that of continuum elements. The strain distribution in the micro trusses is shown in Fig. 3.13 in which the potential crack growth path can be evaluated by identifying the truss element with the highest tensile strain (around voids intersected by the crack). Future studies will account for failure of these elements by introducing relevant instability mechanisms which arise from both geometrical and material origins. On the one hand,

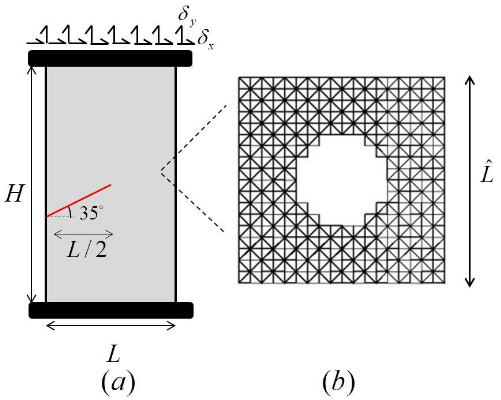

Figure 3.11: *(a) Plate with an inclined edge crack under mixed mode loading. In this problem* $L = 3$, $H = 5.5$, $\delta_x = \delta_y = 0.01$ *and (b) RVE with a void size ratio of* 45%.

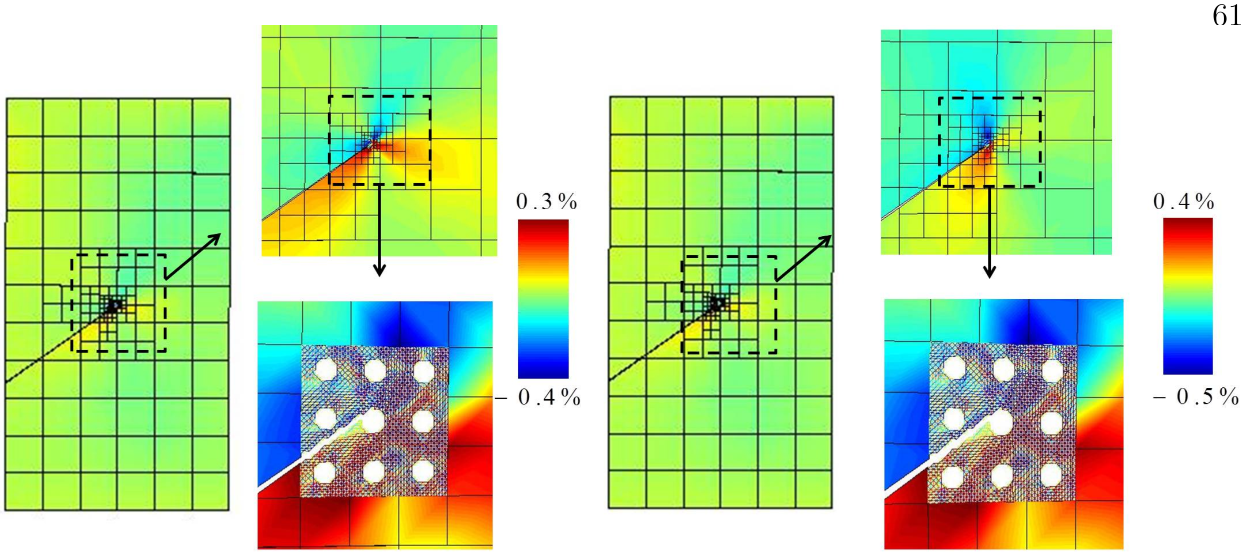

(*a*) (*b*)

Figure 3.12: *(a) horizontal strain, ε_{xx}, in continuum domain and longitudinal strain in micro elements at the end of second and fourth increment for (a) $L/\hat{L}$ ratio of 64 and (b) $L/\hat{L}$ ratio of 128.*

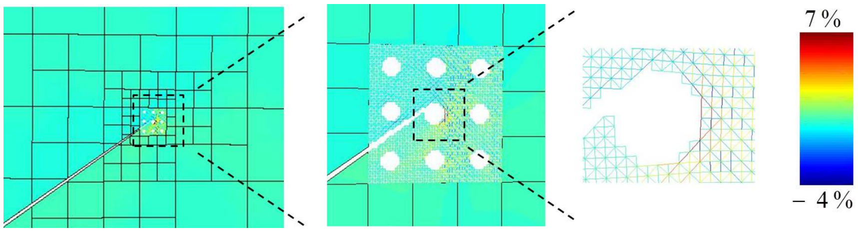

Figure 3.13: *Longitudinal strain in the micro domain.*

the tensile failure of trusses can be described with softening damage/plasticity model that captures the necking instability and rupture. On the other hand, compressive failure can be accounted by incorporating buckling instabilities. Ultimately, incorporating the above mechanisms will allow us to establish a bridge between the microstructure of materials and their fracture behavior (onset of crack growth, crack path, energy dissipation and fracture toughness).

3.7 Conclusion:

The present paper introduced an adaptive multiscale method for fracture in heterogeneous media by invoking concepts of the adaptive refinement, the embedded RVE method and the extended finite element method. The underlying idea of the methodology is to reduce discretization error by local mesh refinement up the level at which continuum assumptions are valid. Once the critical limit of refinement is reached, the strategy consists of replacing continuum elements by RVEs. In this context, a set of bridging scale conditions was introduced in order to enable RVEs to naturally coexist with a surrounding region of large continuum elements. By appropriately combining local refinement and RVE embedding and XFEM enrichment functions, the method ensures a low computational cost while a highly accurate description of the microscopic processes occurring ahead of a crack tip is possible. The efficiency of the method is demonstrated in the first example where microscopic strain field could accurately be predicted when the specimen was subjected to macroscopic boundary conditions. The second example clearly shows the potential of the method by predicting the heterogeneous deformation in void materials. The present work focused on small deformation, linear elastic problems where crack propagation is not permitted. However, this paper lays a strong foundation to investigate more complex problems in which damage and plasticity governs fracture behavior. Further works will therefore consist of extending the method to describe nonlinear material behavior, interstitial fluid flow in cracks[183, 182], nanoscale microstructural effects [142], plastic deformation in order to quantify the relation between microstructure and macroscopic toughness in a diversity of materials.

Chapter 4

Concurrent Multiscale Method, Adaptivity, Strain Localization, Damage and Fracture, Heterogeneous Media

Franck J. Vernerey and Mirmohammadreza Kabir

Department of Civil, Environmental and Architectural Engineering,

University of Colorado, Boulder, USAi

4.1 abstract

We introduce an adaptive concurrent multiscale methodology (ACM^2) to handle situations in which both macroscopic and microscopic deformation fields strongly interact near the tip of a crack. The method is based on the balance between numerical and homogenization error; while the first type of error states that elements should be refined in regions of high deformation gradients, the second implies that element size may not be smaller than a threshold determined by the size of the unit cell representing the material's microstructure. In this context, we build a finite element framework in which unit cells can be embedded in continuum region through appropriate macro-micro boundary coupling conditions. By combining the idea of adaptive refinement with the embedded unit cell technique, the methodology ensures that appropriate descriptions of the material are used adequately, regardless of the severity of deformations. We will then show that our computational technique, in conjunction with the extended finite element method, is ideal to study the strong interactions between a crack and the microstructure of heterogeneous media. In particular, it enables an

explicit description of microstructural features near the crack tip, while a computationally inexpensive coarse scale continuum description is used in the rest of the domain. The paper presents several examples of crack propagation in materials with random microstructures and discuss the potential of the multiscale technique in relating microstructural details to material strength and toughness.

4.2 Introduction

Today's technological advances in micro- and nanofabrication will soon enable the design of new materials that are sustainable, durable and multifunctional through a careful control of their micro-architecture. Proof-of-concepts have already been provided by a number of biological materials that, due to their highly organized microstructure, overwhelmingly exhibit a high fracture toughness, despite their weak building blocks [141, 158]. Fracture resistance is also particularly desirable for next generation of synthetic materials. However, unlike biological materials, they do not benefit from the efficient, but lengthy evolution process to optimize their properties. The development of man-made materials must therefore rely on the use of rational design and mathematical modeling to accurately describe material failure and subsequently predict microstructures that can resist failure the most. So far, research efforts have been hindered by the fact that fracture mechanics in heterogeneous media typically involve two distinct and separate length-scales. On the one hand, the growth of a ductile crack occurs via the evolution of damage ahead of the crack tip, in a relatively small region, known as the process zone [188, 128]. In this region, materials usually exhibit a complex behavior involving inelasticity, damage and eventually a strain-softening response that may induce size effects [128, 157]. A micromechanical modeling approach [162] is often necessary to accurately capture these mechanisms and their effects on fracture resistance. On the other hand, fracture initiation and propagation highly depends on macroscopic loading, geometry and macroscopic material features. At this level, a continuum description is usually preferred due to its ability to describe uniform material deformation and its low computational cost. Because of this scale separation, theoretical studies on the role of microscopic damage on fracture properties have been limited to either unrealistically small domains or overly restrictive assumptions. Instances include the studies of ductile crack growth in metallic alloys [170, 164, 187], or numerical predictions of the fracture resistance of biological silica-based composites [172], to name a few.

From a theoretical and computational viewpoint, a number of alternative strategies have been proposed to address the multiscale dilemma. For instance, a potential solution was provided by the development of higher order continuum theories such as micromorphic theories [188, 186, 187], micro-continuum models [184, 181], Cosserat theory [135, 139, 148] or strain gradient theories [147, 146, 140] in order to capture microstructural size effects when the material deformation becomes inhomogeneous. These methods have been particularly successful when the displacement fields are nonuniform, but smooth, such as during plasticity and the early stages of material's failure. However, when the deformation fields become strongly non-uniform and non-smooth, the very validity of continuum assumptions becomes questionable and new approaches must be considered. In this context, the use of microstructural descriptions provide a clear solution but they often involve computational problems that are intractable over domains of realistic size. This has motivated the development of multiscale methods that can bridge microstructural material descriptions (in regions in which highly heterogeneous deformation occurs) and the continuum description (where the deformation field is homogeneous)[165, 154]. For instance, a class of concurrent multiscale methods [166, 156, 189, 132] was introduced based on the idea that a microscopic region can be determined a priori (such as around a crack tip) and coupled with a coarse grained continuum region via appropriately designed bridging scale conditions. Using a similar idea, Ghosh et al. [150, 149, 160, 169, 168] introduced a method based on Voronoi Cell Finite Element Method (VCFEM) to deal with problems in which the microscopic region is not a priori determined but is informed by the nature of the numerical solution. Finally, we have previously introduced a finite element based Adaptive Concurrent Multiscale Method (ACM^2) that provided a dual (micro-macro) description of an elasticity problem by adaptively splitting a physical domain into a microstructural component (with refined description) and macroscopic continuum component [185]. The adaptivity of the method relied on the idea that element refinement should result from two kinds of approximation errors: discretization and homogenization. This led to the idea that continuum finite element description can only be refined up to a certain level after which elements must be replaced by a more refined microstructural description provided by so-called unit cells.

Despite the number of powerful methods, establishing a relationship between microstructure and the mechanisms of damage evolution and crack propagation still remains a challenge. We therefore propose to extend the concepts behind the ACM^2 to address this shortcoming. The contributions of this paper are several folds. First, we present a method for which a crack is naturally accounted for at both micro and macro scales by coupling the aforementioned multiscale technique with the extended finite element method. Second, because strain and rotation fields are often large in the vicinity of the tip of a loaded crack, we present an iterative nonlinear formulation of the ACM^2 for finite deformation and nonlinear material response. Third and finally, we account for damage nucleation and evolution in the crack tip region by modeling the microscopic material response with a lattice model. This feature is critical to capture the phenomenon of crack propagation in heterogeneous materials. We show, via a variety of examples, that the ACM^2 enables both continuum and explicit microstructural descriptions to coexist within a single simulation and therefore ensures a low computational cost and provides highly accurate results. From a more theoretical viewpoint, the approach addresses the well known issues associated with strain softening and localization by automatically refining the description and therefore capturing microstructural size effects within regions of localized deformations. By doing so, the method also has the potential to reconcile concepts from damage mechanics (which considers microscopic phenomenon only) to those from fracture mechanics (which is inherently macroscopic). We particularly illustrate this point by demonstrating, through a simple example, that it is possible to establish a relationship between microstructure and the overall mechanics of a crack, represented by the resistance curve. In other words, the proposed study provides a tool that, in the long term, can lead to the computational design of material's microstructures with optimized fracture resistance capabilities.

The paper is organized as follows. In the next section, we provide an overview of the ACM^2 to study fracture and briefly recapitulate the error analysis, refinement techniques and bridging scale coupling conditions. In section 3, we focus on the case of multiscale linear elastic fracture with finite deformation and perform a number of studies to illustrate the behavior and performance (accuracy and efficiency) of the ACM^2. Section 4 then concentrates on the case of damage and crack propagation in heterogeneous microstructures. A summary of the paper's contributions is finally provided in section 5 along with concluding remarks.

4.3 Multiscale adaptive formulation to model fracture in heterogeneous media

The general idea behind the ACM^2 is to provide both a microscopic description (in the process zone) and a macroscopic description (further from the crack tip) adaptively as fracture proceeds. The strategy relies on a combination of finite element analysis, adaptive refinement and unit cell modeling for periodic microstructures. Before we give further details, let us first describe the general idea behind the proposed method. Referring to Fig. 4.1a, let us consider a macroscopic domain characterized by presence of a preexisting crack, represented by a surface Γ_c. The material in this domain is assumed to be heterogeneous at the microscale with a periodic structure that is represented by the unit cell of side length $\hat{L}$. Fig. 4.1b shows an example of such a unit cell for a microstructure that possesses a pseudo-random distribution of voids and inclusion. We note that there are no restrictions on the size of the unit cell, as long as it is significantly smaller than the macroscopic domain. The proposed method can thus be used for a variety of heterogeneous materials with inclusions and voids (for instance, steel, concrete, bone) or periodic molecular and atomic structures (crystalline solids). To preserve the mutiscale requirement (low computational cost and high accuracy [143]), the ACM^2 consists of discretizing the macroscopic domain with coarse finite elements and adaptively refining the mesh in the neighborhood of the crack tip (Fig. 4.1c), where the deformation is highly inhomogeneous. As the size of elements become comparable to the size of a unit cells, however, the ACM^2 proposes a strategy in which continuum elements are replaced by unit cells (Fig. 4.1d).

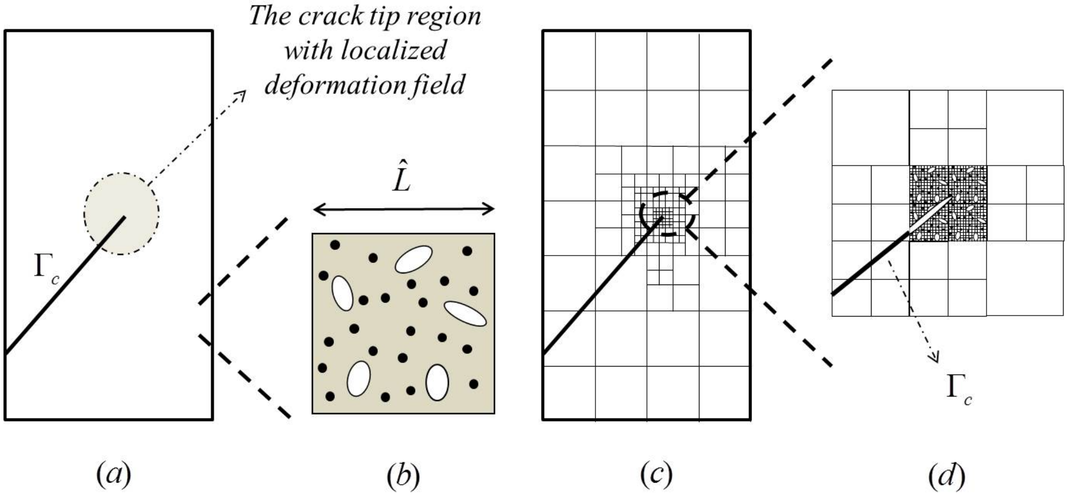

Figure 4.1: *(a) Macroscopic domain with a preexisting crack,* Γ_c*, which is modeled as a line of displacement discontinuity. (b) Schematic of a unit cell of length* $\hat{L}$ *representing the material's microstructure. (c) Illustration of macroscale refinement around the crack tip to reduce numerical error. (d) Continuum elements are replaced with unit cells in the region of high strain gradients.*

A consequence of this operation is that the computational domain is split into two subdomains, namely, the macro- and the micro-domain. The material description in the macrodomain is provided by a pure continuum approach for which the constitutive relation can be derived by performing first order homogenization on the unit cell (Fig. 4.1b) [144]. At the microscale, the domain consists of a "patch" of connected unit cells, which provides an explicit microscopic description without a need for homogenization [185, 174, 180, 134, 131, 167].

This feature is critical as classical homogenization procedures are known to be inaccurate in the regime of material's failure and localization. For clarity, the details of the refinement strategy and the micro-macro transition are left to the next section. It is clear, however, that the framework involves a concurrent technique that is reminiscent of the bridging scale method [189, 166, 156]. It can however be distinguished from it in three significant aspects: (a) the microscopic domain is not a priori determined and is computed from an adaptive refinement strategy, (b) the ACM^2 is developed for quasi-static problems and differs in the treatment of the bridging scale boundary conditions and (c) the ACM^2 is suitable for all micro-domains characterized by continuum, discrete or molecular structures.

4.3.1 Crack description at the macro and micro-scales

The co-existence of macroscopic and microscopic material descriptions calls for a similar definition of a crack at two levels. At the macroscale, it can be represented by a dimensionless surface $\mathbf{\Gamma}_c$ across which displacement fields are discontinuous. Although this representation does not cause any major issues with regular finite elements [173], it is not the case for the ACM^2. Indeed, the nature of the multiscale refinement requires a regular and uniform discretization, made of rectangular finite elements and unit cells [185]. This condition is restrictive to the modeling of curved cracks as they cannot follow element boundaries. The extended finite element method (X-FEM) [159] provides a natural solution to this shortcoming since it enables a discretization-free description of a crack at the expense of adding discontinuous degrees of freedom to elements that are cut by the surface Γ_c. In such elements, the discontinuous displacement is traditionally written as:

$$\mathbf{u}(\mathbf{x}) = \sum_{I \in SI} N^I(\mathbf{x})\mathbf{u}^I + \sum_{I \in SI^{enr}} N^I(\mathbf{x})\left(H(\mathbf{x}) - H(\mathbf{x}_I)\right)\mathbf{a}^I. \tag{4.1}$$

where superscript I denotes node number, $\mathbf{u}$ and $\mathbf{a}$ are the continuous and discontinuous displacement degrees of freedom, respectively, N are the conventional shape functions for a two-dimensional element and H is the Heaviside function [159, 129]. In addition, SI and

SI^{enr} are sets of ordinary and enriched nodes, respectively.

At the microscale, a crack (particularly near its tip) often takes the form of a region of finite width in which various complex processes, such as crack bridging [133, 137, 136, 179], micro-cracking [177, 153] or necking between coalescing voids [178, 176, 175], take place. Its simplistic approximation into a line of discontinuity is therefore unsuitable at this level. The presented method has the advantage of addressing this issue by representing the crack tip region within a structurally refined domain (Fig. 4.1.d) which naturally lends itself to capturing the transition between the macro- and microscopic description of a crack. Microscopically, a crack tip can therefore be modeled in various ways, according to its nature and history, including a micro-notch of finite radius, the presence of a dense distribution of microcracks or even a region of diffused damage. In the present study, we limit ourselves to the first situation as it provides a fairly accurate representation of a ductile crack in a porous matrix [170]. We note that the different resolution used to describe a crack at the micro and macro-scales results in an apparent mismatch between the crack surfaces at the micro-macro boundary (Fig. 6). While this issue does not affect the results reported in this paper, it can potentially be solved by assigning an initial opening to the macroscopic crack in the stress-free state.

4.3.2 Adaptivity and multi-scale refinement

While details of the adaptive multiscale refinement procedure have been discussed in a previous paper [152], we give here a brief summary of the method.

a- Discretization error. Traditionally, FEM refinement strategies aim at minimizing the discretization error which is defined the difference between the approximate numerical solution and the exact solution of the elasticity problem. In [138] a classical discretization error for triangular finite element was introduced. Taking the same approach in [185] we have shown that the discretization error over an square-shaped, two-dimensional element can be expressed with the simple expression:

$$e_d = \frac{h}{\sqrt{12}} ||\nabla\nabla\mathbf{u}(\mathbf{x})|| \tag{4.2}$$

where e_d is the discretization error, h is the side length of the element, $\mathbf{u}(\mathbf{x})$ is displacement field in the element. Furthermore, the symbols ∇ and $||\cdot||$ denote the gradient and L_2 norm operators, respectively. Refinement strategies aim at computing the value of (4.2) over all macroscopic elements and propose to refine the size of elements when this error measure becomes larger than a given tolerance e_d^{max}. While it is satisfying in most situations, this strategy does not converge for problems admitting singular strain fields, as observed in fracture mechanics. Indeed, if strain gradients are singular, it is clear that the discretization error (4.2) will tend to infinity, regardless of the element size.

b- Homogenization error. To address the above shortcoming, another type of error measure, denoted as "homogenization error" must be invoked.

At the continuum level, the introduction of constitutive relations relies upon the concept of homogenization, in which appropriate averaging operations over a representative volume element (RVE) are performed. Since these operations are only valid when macroscopic deformations vary uniformly over the RVE, sharp localization events may sometimes be incompatible with continuum assumptions. The Homogenization error aims at quantifying the loss of accuracy provided by continuum models when the deformation field deviates from uniformity. The continuum approximation (for traditional Cauchy materials) is based on the concept of first order homogenization, which itself relies on a truncated Taylor series that is accurate where second displacement gradients are relatively small compared to leading order terms. We have shown in [185] that the homogenization error e_h over an element can thus be written in terms of the norm of the second displacement gradient as:

$$e_h = \hat{L}||\nabla\nabla\mathbf{u}|| \tag{4.3}$$

where we had defined $\hat{L}$ as the side length of the unit cell (Fig. 4.1b). It should also be noted that despite the similarity in their expressions, e_d and e_h are representative of two fundamentally different sources of errors. On the one hand, the former represents an error source that is purely numerical and arises from the approximate nature of the finite element solution. On the other hand, the latter quantifies the error that originates from continuum assumptions and therefore finds its source within the concept of homogenization and the representative volume element (or unit cell).

c- Multiscale refinement procedure. For maximum accuracy, a numerical solution must ensure that both the homogenization error e_h and the discretization error e_d remain small compared to unity. Practically, we can therefore define maximum allowable errors e_h^{max} and e_d^{max} such that the solution is satisfactory if $e_h < e_h^{max}$ and $e_d < e_d^{max}$ for all macroscopic elements. A discussion on the meaning and acceptable values for these criteria is provided in [185]. Combining these requirements with (4.2) and (4.3), it can be shown that there exists a critical element size h^c, below which any further refinement will only increase the discretization error. This critical size is given by:

$$h^c = \alpha \hat{L}, \qquad \text{where} \qquad \alpha = \frac{\sqrt{12} e_d^{max}}{e_h^{max}}. \tag{4.4}$$

One can generally interpret this result as follows; when elements are significantly larger than the unit cell and the deformation field is uniform, a homogenized material response is appropriate to represent their mechanical response. However, as their size becomes comparable or smaller than the size of a unit cell, it is no longer appropriate to use a macroscale, homogenized response and elements should be replaced by a more accurate, microstructural description. This is accomplished by substituting these elements by explicit unit cells that concurrently exist within the macroscale FEM description (Fig. 4.1d).

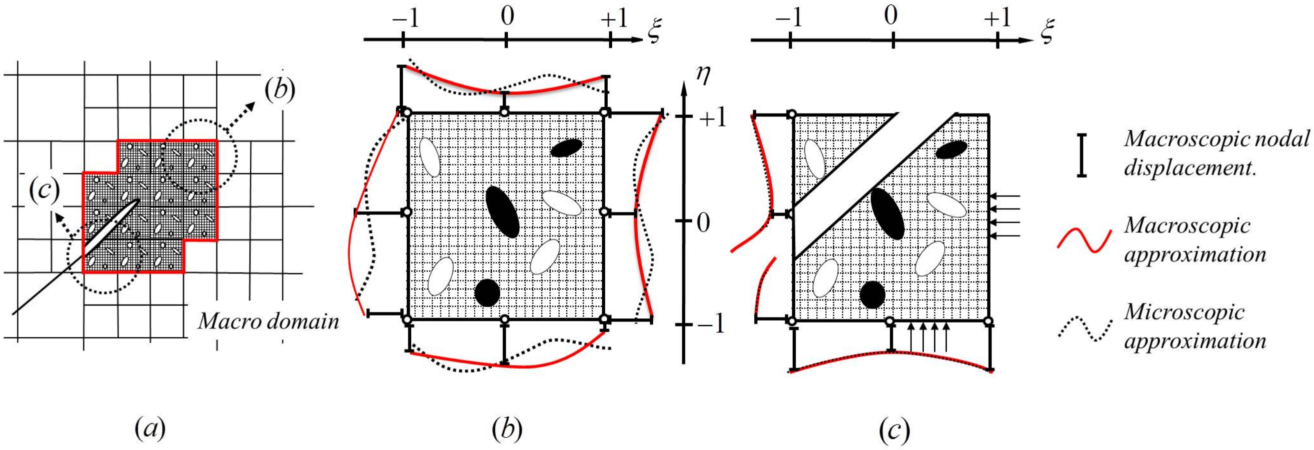

Figure 4.2: *(a) Microscopic domain, made of a patch of unit cells, in the vicinity of a crack tip. (b) Schematic of a unit cell on the macro-micro boundary and illustration of the displacement fields when quasi-periodic boundary coupling conditions are applied, (c) The periodicity of unit cell deformation is not respected when it is intersected by a crack. Strong boundary coupling conditions are therefore applied on this type of unit cells.*

4.3.3 Macro-micro coupling

Let us now discuss the conditions to be enforced at the boundary between macroscopic and microscopic domains. In [185], we have introduced three types of displacement coupling conditions (namely strong coupling, weak coupling and quasi-periodic boundary coupling) that are reminiscent of the different types of boundary conditions that can be applied to a representative volume element during computational homogenization [155]. We have also shown that quasi-periodic boundary coupling provided the most accurate prediction of the microscopic strain in unit cells by allowing realistic fluctuation fields on its boundaries [185]. In the context of fracture, however, such boundary coupling cannot always be applied as discussed below. A mixed approach using both strong displacement and quasi-periodic conditions is therefore taken.

a- Quasi-periodic boundary coupling. As depicted in Fig. 4.2, this coupling condition enforces two constraints: First, the microscopic displacement on the boundary $\hat{\Gamma}$ between the unit cell and the macroscopic domain follows on average, the macroscopic displacement.

This requirement can be enforced with the least-square method for which the error function $\mathbf{e}$, can be expressed as the difference between macro and micro-displacements on $\hat{\Gamma}$. The error function is then written as:

$$e = \left(\sum_{i=1}^{n_{node}} \left(\mathbf{u}(\boldsymbol{\xi}_i) - N^j(\boldsymbol{\xi}_i)\mathbf{U}^j \right)^2 \right)^{1/2}, \qquad \boldsymbol{\xi} \in \hat{\boldsymbol{\Gamma}} \tag{4.5}$$

where $\mathbf{U}$ and $\mathbf{u}$ denote macroscopic and microscopic nodal displacements, respectively, $\boldsymbol{\xi}$ denotes the local coordinates of a point in the unit cell as shown in Fig. 4.2 and n_{node} represents the number of microscopic nodes on $\hat{\boldsymbol{\Gamma}}$. The conformity between macro and micro-displacements on $\hat{\boldsymbol{\Gamma}}$ is then ensured by minimizing this error, or equivalently, by enforcing that its derivative with respect to macroscopic nodal displacement vanish. This leads to constraints functions $\mathbf{c}_{LS}^{M}$ of the form:

$$\mathbf{c}_{LS}^{M} = \frac{\partial \mathbf{e}}{\partial \mathbf{U}} = 0 \quad \Longrightarrow \quad \sum_{i=1}^{n_{node}} \left(N^k(\boldsymbol{\xi}_i)\mathbf{U}^k - \mathbf{u}(\boldsymbol{\xi}_i) \right) = 0 \quad \text{(no sum on k)} \tag{4.6}$$

Second, to ensures that the fluctuation fields on the microscopic domain are represented accurately, additional constraints should be added to specify that unit cells that belong to the boundary $\hat{\Gamma}$ deform in a quasi-periodic fashion. This leads to the following requirements [185]:

$$\begin{aligned} \mathbf{c}_{BT} = [\mathbf{u}_T(\xi) - \mathbf{u}_B(\xi)] - \left[\sum_I N^I(\xi,1)\mathbf{U}_T^I - \sum_I N^I(\xi,-1)\mathbf{U}_B^I \right] &= 0 \\ \mathbf{c}_{LR} = [\mathbf{u}_R(\eta) - \mathbf{u}_L(\eta)] - \left[\sum_I N^I(1,\eta)\mathbf{U}_R^I - \sum_I N^I(-1,\eta)\mathbf{U}_L^I \right] &= 0 \end{aligned} \tag{4.7}$$

where subscripts B, L, T and R denote bottom, left, top and right boundaries of a unit cell, respectively. A consequence of these conditions is thus that unit cells display similar fluctuation fields on opposite boundaries while the conformity between macroscopic and microscopic displacement fields is ensured in an average sense (Fig. 4.2). These features stem from our assumptions of the periodicity of the microstructure.

b- Strong boundary coupling. Although the quasi periodic boundary coupling conditions can be applied on almost any unit cell at the micro-macro boundaries, an exception must be made for those that are located on the crack path (Fig. 4.2c). Indeed, unlike the microstructure, a crack is not periodically present in all unit cells; this implies that the application of periodic coupling likely leads to a very inaccurate approximation of fluctuation fields on $\hat{\Gamma}$. In this situation, we therefore propose to apply the so-called strong coupling conditions in the form:

$$\mathbf{c}_{SC} = \mathbf{u}(\xi) - \sum_{I \in SI} N^I(\xi)\mathbf{U}^I - \sum_{I \in SI^{enr}} N^I(\xi)\psi(\xi)\mathbf{a}^I = 0 \tag{4.8}$$

where SI and SI^{enr} are the set of all ordinary and enriched nodes, respectively, on the boundary $\hat{\Gamma}$ and $\mathbf{a}^I$ denotes the enriched nodal degrees of freedom corresponding to the macro nodes appearing in (4.8). It is important to note that this requirement ensures that macro and micro-displacement conform exactly on $\hat{\Gamma}$ as depicted in Fig. 4.2c.

4.4 Modeling of elastic cracks in heterogeneous media

The objective of this section is to establish the basis of the ACM^2 for fracture mechanics and microstructural damage. The formulation is first introduced in the context of elastic fracture for two reasons. First, it will enable us to discuss the implementation of the method in the presence of a crack without the complexity of damage evolution. Second, the case of nonlinear finite deformation and the associated iterative procedure can be introduced in a simple situation. In the following examples, the material is assumed to be elastic, periodic and porous with a representative unit cell containing two voids of radius $\hat{L}/6$ centered at coordinates $(\pm\hat{L}/10, \pm\hat{L}/10)$ with respect to the center of the domain (Fig. 4.3a). The matrix material is modeled as a Saint Venant-Kirchhoff model that relates the microscopic (second Piola-Kirchhoff) stress $\tilde{\mathbf{S}}$ to the microscopic Green-Lagrange strain $\tilde{\mathbf{E}}$ via elastic constants $\tilde{\lambda}$ and $\tilde{\mu}$ as:

$$\tilde{\mathbf{S}} = \tilde{\lambda} \cdot tr(\tilde{\mathbf{E}})\mathbf{1} + 2\tilde{\mu}\tilde{\mathbf{E}}, \qquad \text{and} \qquad \tilde{\mathbf{E}} = \frac{1}{2}\left(\nabla\tilde{\mathbf{u}} + (\nabla\tilde{\mathbf{u}})^T + (\nabla\tilde{\mathbf{u}})^T \cdot \nabla\tilde{\mathbf{u}}\right). \tag{4.9}$$

We note that this model is merely an extension of a linear, isotropic elastic material to the range of large deformations. At the macroscale, we then assume that the material retains the characteristics of a Saint Venant-Kirchhoff material and compute the associated elastic constants $\bar{\lambda}$ and $\bar{\mu}$ via a first order computational homogenization procedure prior to the multiscale analysis (Fig. 4.3) [186] We note that these constants are determined once and are used at the entire macroscopic domain.

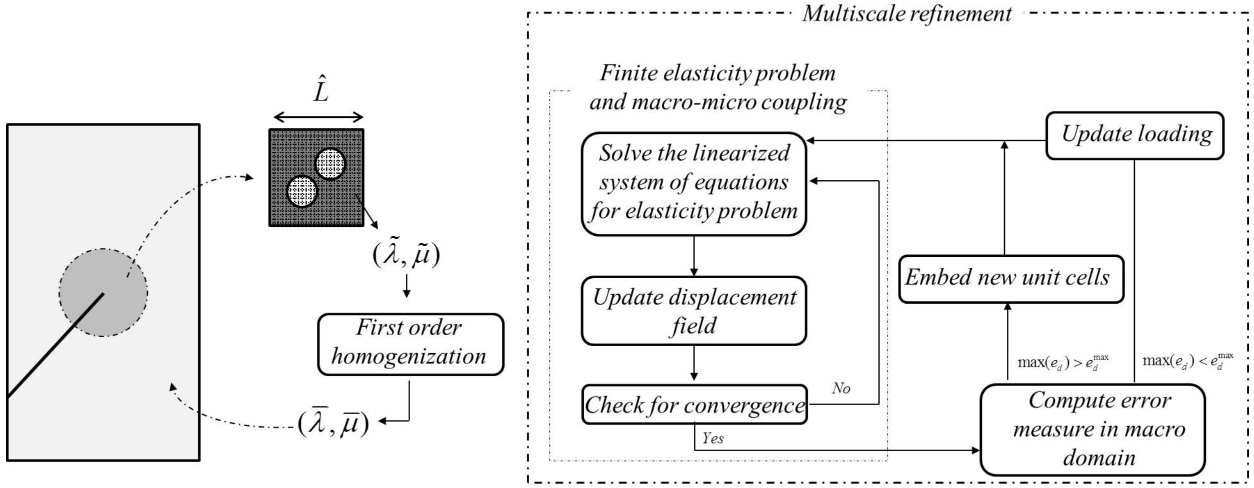

(*a*) (*b*)

Figure 4.3: *(a) Macroscopic domain and associated unit cell for a porous and periodic medium. The relationship between matrix elastic properties and macroscopic elastic properties is derived by computationally performing a first order homogenization [144] procedure on the unit cell. (b) The algorithm of nested iterations for the nonlinear elasticity problem.*

4.4.1 Numerical problem

Numerically, the multiscale method relies on a nonlinear algorithm with two-level nested iterations (Fig. 4.3b). On the one hand, the "inner" level of iterations seeks to determine the nonlinear elastic solution of the two-scale problem. On the other hand, the "outer" level analyses the converged elastic solution, computes the two types of error defined in section 4.3.2 for macroscopic elements and refines the description accordingly. We discuss here each of these numerical aspects in further details.

a- Finite elasticity problem and macro-micro constraints. Let us consider a physical domain with an embedded crack and a numerical FEM discretization that is split into a macroscale and a microscale domain as represented in Fig. 4.3a. Consistent with this domain decomposition, we introduce three types of degrees of freedom: the macroscopic nodal displacements $\bar{\mathbf{u}}$, the microscopic nodal displacements $\tilde{\mathbf{u}}$ and a set of Lagrange-multipliers, denoted as $\boldsymbol{\lambda}$ that are used to enforce constraints at the micro-macro boundary. The energy W^c of the system can then be written:

$$W^c(\bar{\mathbf{u}}, \tilde{\mathbf{u}}, \boldsymbol{\lambda}) = W(\bar{\mathbf{u}}, \tilde{\mathbf{u}}) + \boldsymbol{\lambda}^T \mathbf{c}(\bar{\mathbf{u}}, \tilde{\mathbf{u}}) \tag{4.10}$$

where W is the total energy in the absence of constraints and the constraints $\mathbf{c}$ are written in terms of the various conditions developed in section 4.3.3:

$$\mathbf{c}(\bar{\mathbf{u}}, \tilde{\mathbf{u}}) = [\mathbf{c}_{LS} \;\; \mathbf{c}_{BT} \;\; \mathbf{c}_{LR} \;\; \mathbf{c}_{SC}]. \tag{4.11}$$

It is furthermore convenient to decompose the functional W^c into a macroscopic component $\bar{W}$ which is only a function of the macroscopic displacements and a microscopic component $\tilde{W}$, written in terms of microscopic displacements only. Further splitting these energies into components ($\bar{W}^{int}$ and $\tilde{W}^{int}$) from internal forces and components ($\bar{W}^{ext}$ and $\tilde{W}^{ext}$) associated with the work of external forces, we write:

$$W(\bar{\mathbf{u}}, \tilde{\mathbf{u}}) = \bar{W}^{int}(\bar{\mathbf{u}}) + \tilde{W}^{int}(\tilde{\mathbf{u}}) - \bar{W}^{ext}(\bar{\mathbf{u}}) - \tilde{W}^{ext}(\tilde{\mathbf{u}}). \tag{4.12}$$

Recognizing that the solution of the multiscale elasticity problem is found by minimizing the constrained energy W^c, the governing equations are obtained by stating that the gradient of (4.10) with respect to the independent variables, $\bar{\mathbf{u}}$, $\tilde{\mathbf{u}}$ and $\boldsymbol{\lambda}$ must vanish. This condition yields:

$$\begin{aligned} W^c_{,\bar{\mathbf{u}}} &= \bar{\mathbf{f}}^{int} - \bar{\mathbf{f}}^{ext} + \boldsymbol{\lambda}^T \mathbf{c}_{,\bar{\mathbf{u}}} = \mathbf{0}, \\ W^c_{,\tilde{\mathbf{u}}} &= \tilde{\mathbf{f}}^{int} - \tilde{\mathbf{f}}^{ext} + \boldsymbol{\lambda}^T \mathbf{c}_{,\tilde{\mathbf{u}}} = \mathbf{0}, \\ W^c_{,\bar{\lambda}} &= \mathbf{c}(\bar{\mathbf{u}}, \tilde{\mathbf{u}}) = \mathbf{0} \end{aligned} \tag{4.13}$$

where the subscripts denotes partial derivatives and $\bar{\mathbf{f}}^{int} = \bar{W}^{int}_{,\bar{\mathbf{u}}}$, $\bar{\mathbf{f}}^{ext} = \bar{W}^{ext}_{,\bar{\mathbf{u}}}$, $\tilde{\mathbf{f}}^{int} = \tilde{W}^{int}_{,\tilde{\mathbf{u}}}$ and $\tilde{\mathbf{f}}^{ext} = \tilde{W}^{ext}_{,\tilde{\mathbf{u}}}$ are the internal and external forces at the macro and microscale, respectively. Within the total Lagrangian formulation, these forces can be expressed in terms of the macroscopic and microscopic stresses $\bar{\mathbf{S}}$ and $\tilde{\mathbf{S}}$ as

$$\begin{aligned} \bar{\mathbf{f}}^{int} &= \int_{\bar{\Omega}_0} \mathbf{B}_0^T \{\bar{\mathbf{S}}\} d\bar{\Omega}_0 \quad \text{and} \quad \tilde{\mathbf{f}}^{int} = \int_{\tilde{\Omega}_0} \mathbf{B}_0^T \{\tilde{\mathbf{S}}\} d\tilde{\Omega}_0 \\ \bar{\mathbf{f}}^{ext} &= \int_{\bar{\Gamma}_0} \mathbf{N}\bar{\mathbf{t}} d\bar{\Gamma}_0 \quad \text{and} \quad \tilde{\mathbf{f}}^{ext} = \int_{\bar{\Gamma}_0} \mathbf{N}\tilde{\mathbf{t}} d\tilde{\Gamma}_0 \end{aligned} \tag{4.14}$$

in which $\bar{\Omega}_0$ and $\tilde{\Omega}_0$ are respectively the macroscopic and microscopic element domains in the reference configuration, while $\bar{\Gamma}_0$ and $\tilde{\Gamma}_0$ denote element edges that belong to the domain boundary Γ. In addition, the matrix $\mathbf{N}$ contains the finite element shape functions and $\mathbf{B}_0$ is the matrix containing their derivative. Details on these standard notations can be found in [130]. The final system of nonlinear equations (4.13) can then be solved numerically via the Newton-Raphson method relying on the following linearized form:

$$\begin{aligned} \bar{\mathbf{r}} + \boldsymbol{\lambda}^T \bar{\mathbf{G}} + \bar{\mathbf{K}} \delta \bar{\mathbf{u}} + \bar{\mathbf{G}}^T \delta \boldsymbol{\lambda} &= \mathbf{0} \\ \tilde{\mathbf{r}} + \boldsymbol{\lambda}^T \tilde{\mathbf{G}} + \tilde{\mathbf{K}} \delta \tilde{\mathbf{u}} + \tilde{\mathbf{G}}^T \delta \boldsymbol{\lambda} &= \mathbf{0} \\ \mathbf{c} + \bar{\mathbf{G}} \delta \bar{\mathbf{u}} + \tilde{\mathbf{G}} \delta \tilde{\mathbf{u}} &= \mathbf{0} \end{aligned} \tag{4.15}$$

where the residual functions are defined by $\bar{\mathbf{r}} = \bar{\mathbf{f}}^{int} - \bar{\mathbf{f}}^{ext}$ and $\tilde{\mathbf{r}} = \tilde{\mathbf{f}}^{int} - \tilde{\mathbf{f}}^{ext}$, the interaction matrices were introduced as $\bar{\mathbf{G}} = \mathbf{c}_{,\bar{\mathbf{u}}}$ and $\tilde{\mathbf{G}} = \mathbf{c}_{,\tilde{\mathbf{u}}}$ and the macroscopic and microscopic tangent matrices take the form $\bar{\mathbf{K}} = \bar{\mathbf{r}}_{,\bar{\mathbf{u}}}$ and $\tilde{\mathbf{K}} = \tilde{\mathbf{r}}_{,\tilde{\mathbf{u}}}$. For finite deformation elasticity, the stiffness matrices can generally be decomposed into a material and a geometrical component; for the sake of clarity, we show the detailed expressions in Appendix I. It is finally important to note that we implicitly used the fact that the second derivatives of constraint functions with respect to displacement fields $\bar{\mathbf{u}}$ and $\tilde{\mathbf{u}}$ identically vanish. The incremental numerical formulation therefore consists of finding the i^{th} increment in nodal quantities ${}^{(i)}\Delta = [{}^{(i+1)}\delta\bar{\mathbf{u}} \;\; {}^{(i+1)}\delta\tilde{\mathbf{u}} \;\; {}^{(i+1)}\delta\boldsymbol{\lambda}]$ by solving the matrix equation:

$$\begin{bmatrix} {}^{(i)}\bar{\mathbf{K}} & \mathbf{0} & {}^{(i)}\bar{\mathbf{G}}^T \\ \mathbf{0} & {}^{(i)}\tilde{\mathbf{K}} & {}^{(i)}\tilde{\mathbf{G}}^T \\ {}^{(i)}\bar{\mathbf{G}} & {}^{(i)}\tilde{\mathbf{G}} & \mathbf{0} \end{bmatrix} \begin{bmatrix} {}^{(i+1)}\delta\bar{\mathbf{u}} \\ {}^{(i+1)}\delta\tilde{\mathbf{u}} \\ {}^{(i+1)}\delta\boldsymbol{\lambda} \end{bmatrix} = \begin{bmatrix} -{}^{(i)}\bar{\mathbf{r}} - {}^{(i)}\,\boldsymbol{\lambda}^T\;{}^{(i)}\bar{\mathbf{G}} \\ -{}^{(i)}\tilde{\mathbf{r}} - {}^{(i)}\,\boldsymbol{\lambda}^T\;{}^{(i)}\tilde{\mathbf{G}} \\ -{}^{(i)}\mathbf{c} \end{bmatrix} \tag{4.16}$$

This form clearly shows the decomposition of the problem into a macroscale component (matrix $\bar{K}$), a microscale component (matrix $\tilde{K}$) and interaction matrices $\bar{\mathbf{G}}$ and $\tilde{\mathbf{G}}$ enforcing the coupling conditions between the macro and micro-domains.

b- Multiscale refinement. Based on the computed elastic solution, the discretization and homogenization errors defined in (4.2) and (4.3) are calculated in all macroscopic elements and compared to tolerance values. Elements that exhibit large errors are subsequently split into four smaller elements following a technique discussed in [185]. This refinement procedure continues until elements reach the critical size h_c expressed in (5.5), after which it is replaced by a unit cell. While the initial discretization is usually at the macroscale, it should be noted that an exception should be made in the case of fracture. Indeed, in the presence of a crack, the LEFM solution predicts singular strain fields varying with $r^{-1/2}$ (r being the distance from crack tip) around the crack tip. This implies that both error measures (e_d and e_h) will automatically exceed their tolerance in the crack tip region as the strain gradients diverge. Based on this argument, the initial FEM discretization automatically includes a unit cell into the macroscopic element that contains the crack tip as shown in Fig. 4.4. Furthermore, since the periodic assumptions corresponding to the unit cell located at the crack tip is violated by the presence of crack (as discussed in section 4.3.3), the method aims at inserting adjacent unit cells on which periodic coupling conditions are acceptable. This procedure is schematically illustrated for two different cases (horizontal and inclined crack) in Fig. 4.4.

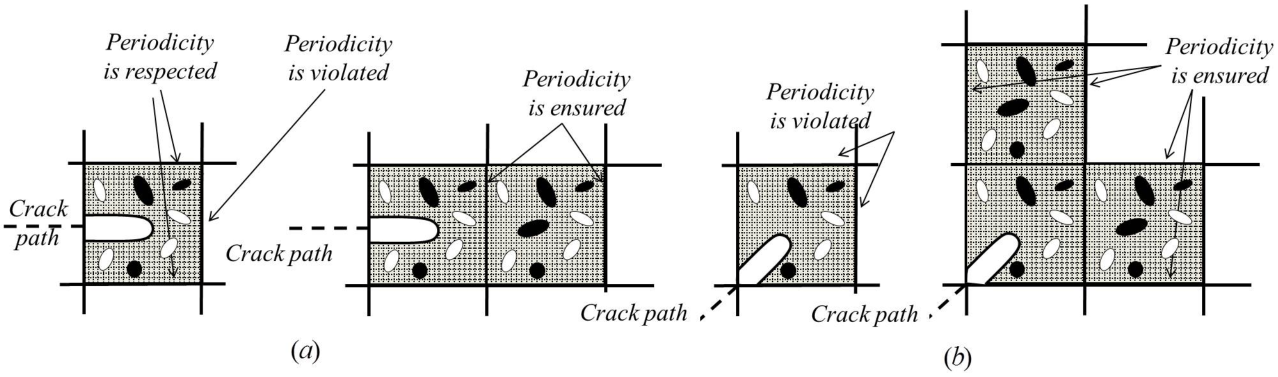

Figure 4.4: *The periodicity of unit cells near a crack tip can be preserved by adding additional adjacent cells. Different numbers and placements of such cells are considered for (a) straight crack and (b) inclined cracks.*

4.4.2 Efficiency analysis: ACM^2 versus brute force analysis

Let us first assess the efficiency of the proposed method compared to a fully microstructured analysis. For this we consider a rectangular plate of size $L \times D$ with a horizontal edge crack, as shown in Fig. 4.5. Over the bottom edge, motion is prescribed in both directions while over the top edge, displacements are held fixed in the horizontal direction and prescribed with a value of $\delta_y = 0.001 \times D$ in the vertical direction. The material's microstructure is assumed to be periodic and voided with the relative porosity of 0.0873 as shown by the unit cell (of side length $\hat{L}$) in Fig. 4.5. For simplicity, the voids are assumed to have a circular cross-section with a diameter $\frac{\hat{L}}{3}$ and located at the center of the unit cell. For the computations, the lamé constants of the microscopic matrix material are taken to be $\tilde{\lambda} = \tilde{\mu} = 7 \times 10^6$ and $\tilde{\mu} = 4.017 \times 10^6$. The macroscopic material properties, derived from the first order homogenization, are then found to be $\bar{\lambda} = 6.0544 \times 10^6$ and $\tilde{\mu} = 5.6528 \times 10^6$. Our numerical approach was then tested in two ways. First, the numerical accuracy was investigated by comparing the stress components σ_{xx} and σ_{yy} at similar points in front of crack tip for all simulations (Fig. 4.5). Second, numerical efficiency was measured by computing the variation in computational cost obtained from the ACM^2 and brute force (BF) simulations (or direct numerical simulation), for $L/\hat{L}$ equal to 32, 64 and 128. It should be noted here that brute force simulations provide an expensive solution technique since a refined finite element mesh is used in the entire domain, irrespectively of the location of the crack. They however provide a good reference to assess the relative cost of our multiscale method for different values of $L/\hat{L}$. The gain in computational cost for each pair of simulation is then assessed by showing the ratio $n_{dof}^{BF}/n_{dof}^{ACM^2}$, in which n_{dof}^{BF} and $n_{dof}^{ACM^2}$ are the numbers of degrees of freedom in BF analysis and ACM^2 analysis, respectively. From this figure one can observe that the computational efficiency of the proposed method increases exponentially as the characteristic length of the microstructure decreases, while the numerical results are in good agreement with the BF analysis.

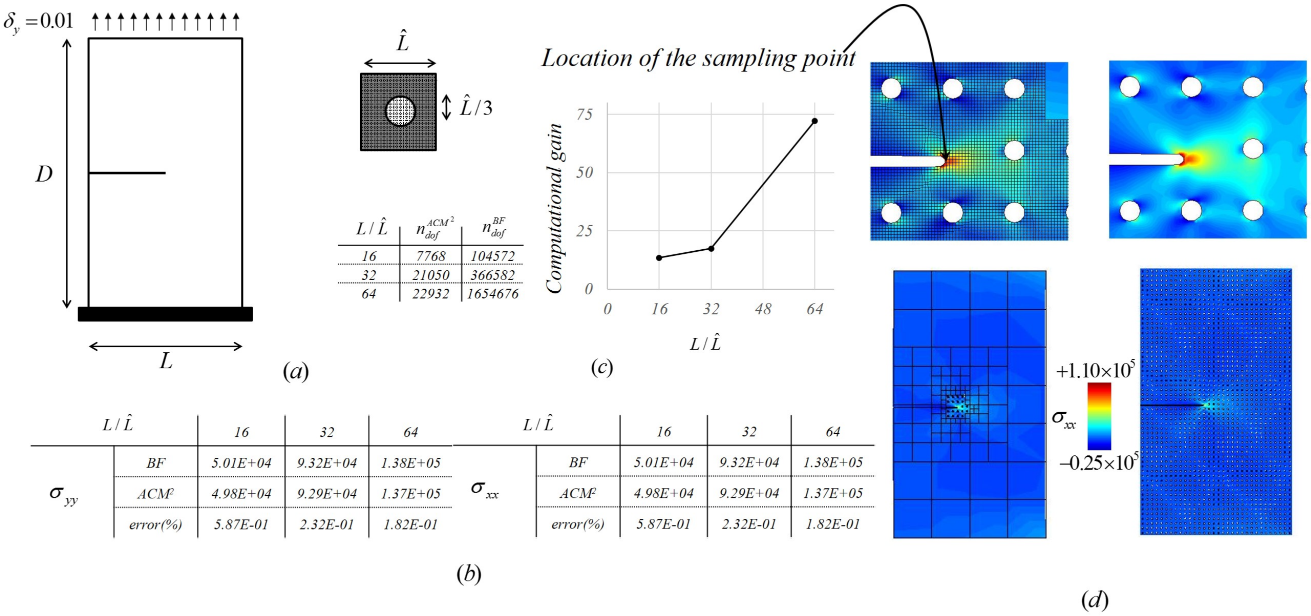

$L/\hat{L}$	$n_{dof}^{ACM^2}$	n_{dof}^{BF}
16	7768	104572
32	21050	366582
64	22932	1654676

$L/\hat{L}$		16	32	64
σ_{yy}	BF	5.01E+04	9.32E+04	1.38E+05
	ACM^2	4.98E+04	9.29E+04	1.37E+05
	error(%)	5.87E-01	2.32E-01	1.82E-01

$L/\hat{L}$		16	32	64
σ_{xx}	BF	5.01E+04	9.32E+04	1.38E+05
	ACM^2	4.98E+04	9.29E+04	1.37E+05
	error(%)	5.87E-01	2.32E-01	1.82E-01

Figure 4.5: *(a) Geometry of the problem and the microscopic unit cell. (b) Comparison of the near crack tip stress fields obtained from ACM^2 and BF analysis. (c) Computational gain versus* $\hat{L}$*. (d)* σ_{xx} *field obtained from ACM^2 (left) and BF (right) over entire domain and around crack tip.*

4.4.3 Optimum refinement criteria and computational cost: case of an edge crack

We now propose to assess the accuracy and the computational efficiency of the ACM^2 while varying the refinement criteria by considering the case of a single edge crack that co-exists with the periodic microstructure whose associated unit cell is depicted in Fig. 4.3a. To further illustrate the flexibility of the method, we consider two situations: (a) the case of a horizontal, straight crack whose direction is in line with the mesh and (b) the case of an inclined crack. For all simulations, the microscopic lamé constants are $\tilde{\lambda} = \tilde{\mu} = 7 \times 10^6$ Pa and the macroscopic lamé constant, derived from the first order homogenization, are $\bar{\lambda} = 6.778 \times 10^6$ and $\tilde{\mu} = 4.017 \times 10^6$.

a- Horizontal crack. Let us consider a semi-infinite crack in an infinite domain under mode I loading (opening) conditions. Numerically, the associated far displacement fields $\mathbf{u}$, can be represented by the Linear Elastic Fracture Mechanics (LEFM) solution around a crack as [188]:

$$\begin{aligned} u_1 &= \frac{K_I}{2\bar{\mu}}\sqrt{\frac{r}{2\pi}}\cos(\frac{\theta}{2})\left[\kappa - 1 + 2\sin^2(\frac{\theta}{2})\right] \\ u_2 &= \frac{K_I}{2\bar{\mu}}\sqrt{\frac{r}{2\pi}}\sin(\frac{\theta}{2})\left[\kappa + 1 - 2\cos^2(\frac{\theta}{2})\right] \end{aligned} \tag{4.17}$$

where r and θ are polar coordinates in a system centered at the crack tip, $\bar{\mu}$ is the macroscale shear modulus, $\kappa = 4 - 3\bar{\mu}$ for plane strain condition and K_I is the mode I stress intensity factor. These displacements are applied as boundary conditions on a rectangular domain of size $512\hat{L} \times 896\hat{L}$ as depicted in Fig.(5)a. At the micro-level, the unit cell domain is discretized with a structured mesh possessing 21×21 quadrilateral 4-node elements, which ensured a precise description of the local stress and strain field around the crack tip. We also found that denser discretization did not affect the multiscale refinement, but it involved a rise in computational time to reach a very similar results. Also, the two voids are modeled with the X-FEM formulation following the approach described in [142].

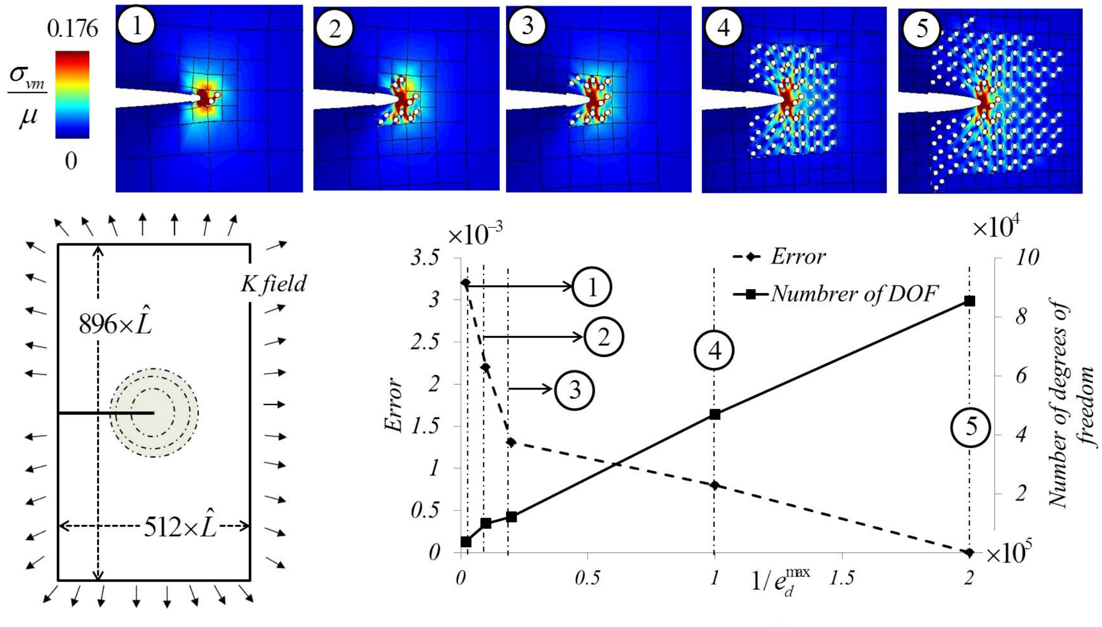

(*a*) (*b*)

Figure 4.6: *(a) Rectangular domain with a horizontal edge crack under a mode I displacement "K-field" .(b) Variation of the approximation error defined in* (4.18) *and computational cost for different values of* $1/e_d^{max}$*. Corresponding refinement levels and associated von-Mises (normalized by shear modulus* μ*) stresses are also depicted.*

Since fracture is strongly affected by the magnitude of the strains in the immediate vicinity of the tip, it is critical to accurately capture displacement fields in this region. We propose here to explore the role of the error criterion on model accuracy by numerically subjecting a preexisting crack to a constant driving force K_I ($K_I = 5 \times 10^5$) and assessing the change in local displacement field with e_d^{max}. We then argue that the value of (e_d^{max}) that leads to a negligible change in local displacement field is satisfactory. To identify this value, we thus introduce a measure e^α of the change in local displacement fields as follows:

$$e^\alpha = \int_{\Omega_T} ||\mathbf{u}^\alpha - \mathbf{u}^{\alpha-1}||d\Omega \tag{4.18}$$

where Ω_T denotes the unit cell that contains the crack tip. We then plot this measure in terms of the discretization error in Fig. 4.6b. The computational cost of the method is further estimated by the number of degrees of freedom (size of the solution vector) necessary to obtain a fully converged and refined solution. Fig. 4.6b thus shows (a) the drop in error

e^{α} and (b) the increase in computational cost resulting from decreasing the tolerance e_d^{max}. The figure also displays the microscopic regions for each values of e_d^{max} and the associated von-Mises stress fields. It can clearly be seen that decreasing the error tolerance provides a more accurate solution at the expense of computation cost. Interestingly, the accuracy seems to follow a bi-linear relationship. For a value of e_d^{max} greater than 1%, we observe a large gain in accuracy for relatively small changes in the tolerance. However, when e_d^{max} becomes smaller than 1%, the gain in accuracy is not as sharp. This feature may be explained by the fact that at the critical value $e_d^{max} \approx 1\%$, the crack tip region (where the strain are the most inhomogeneous) becomes entirely surrounded by unit cells. Further refinement results in adding unit cells further from the crack, which only contributes mildly to the overall accuracy. On the other hand, an important increase in computational cost is observed when e_d^{max} becomes larger than 1%. It, therefore, seems like an optimum value of the discretization error, which provide high accuracy and low computation cost, is $e_d^{max} \approx 1\%$.

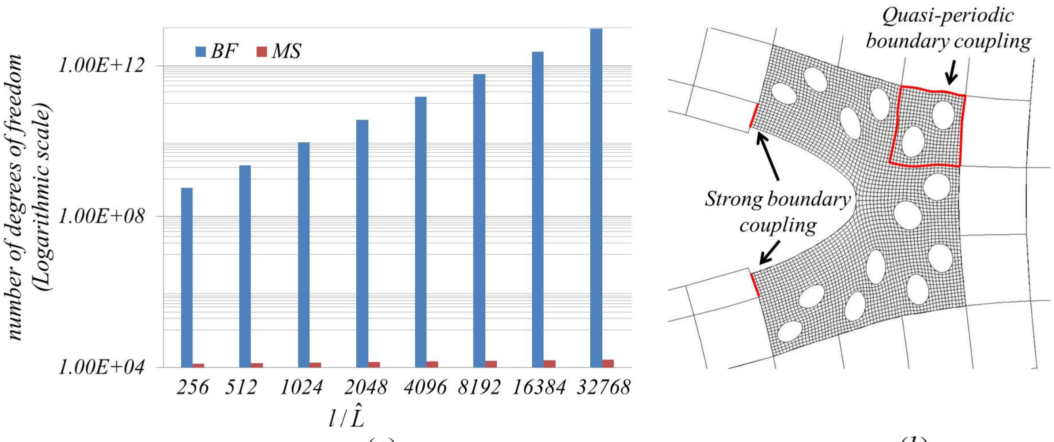

(*a*) (*b*)

Figure 4.7: *(a) Comparison of the computational cost between the ACM^2 and the brute force approach, for different ratios $l/\hat{L}$. The computational gains are significant when the characteristic length-scale $\hat{L}$ of the material becomes small compared to the application length-scale l. (b) Magnification of the microscopic region and associated fluctuation fields on the microscopic boundary.*

A study of computational cost (Fig. 6a) is then performed by calculating the total number of degrees of freedom necessary to obtain an accurate solution using two strategies: (a) the ACM^2 and (b) an equivalent direct numerical simulation (DNS) strategy, where a refined (microscopic) description is used in the entire macroscopic domain. Comparing the cost associated with the two methods, Fig. 6a clearly shows that the gain in computation cost with ACM^2 increases drastically as the scale separation $l/\hat{L}$, between the macroscopic problem and the microstructure becomes more pronounced. These large computational gains are possible thanks to the reduced number of embedded unit cells necessary to obtain an accurate solution, a feature that is partly due to the applications of quasi-periodic boundary coupling. Indeed, the existence of displacement fluctuations on the macro-micro boundary (Fig. 6b) largely contributes to the accuracy of the microscale solution, even for small microscopic domains.

b- Inclined crack. To explore the behavior of the method when a crack is not in line with the mesh, let us now consider an edge crack with an inclination θ ($\theta = 51°$ degrees here) in a rectangular domain of size $512\hat{L} \times 896\hat{L}$ as shown in Fig.(6)a. Mixed mode loading conditions are then provided by constraining the motion of the bottom boundary in both vertical and horizontal directions and applying a positive vertical displacement $\delta_y = 0.64\hat{L}$ to the top boundary. Fig. 4.6b depicts the contours of von-Mises stresses in both domains in the vicinity of crack tip region and depicts the change in accuracy with changes in error tolerance $(e_d^{max})^i$. Once again, we clearly see an optimal value of the error, which is estimated to be 0.004. This value is fairly consistent with that derived in the previous example, which confirms the flexibility of the method, regardless of crack orientation.

4.4.4 Evolution of the refined region during incremental loading: case of double edge cracks

This section discusses the adaptivity of the refined microscopic region when a domain is subjected to incremental loading. In this part we assume that the material remains in elastic

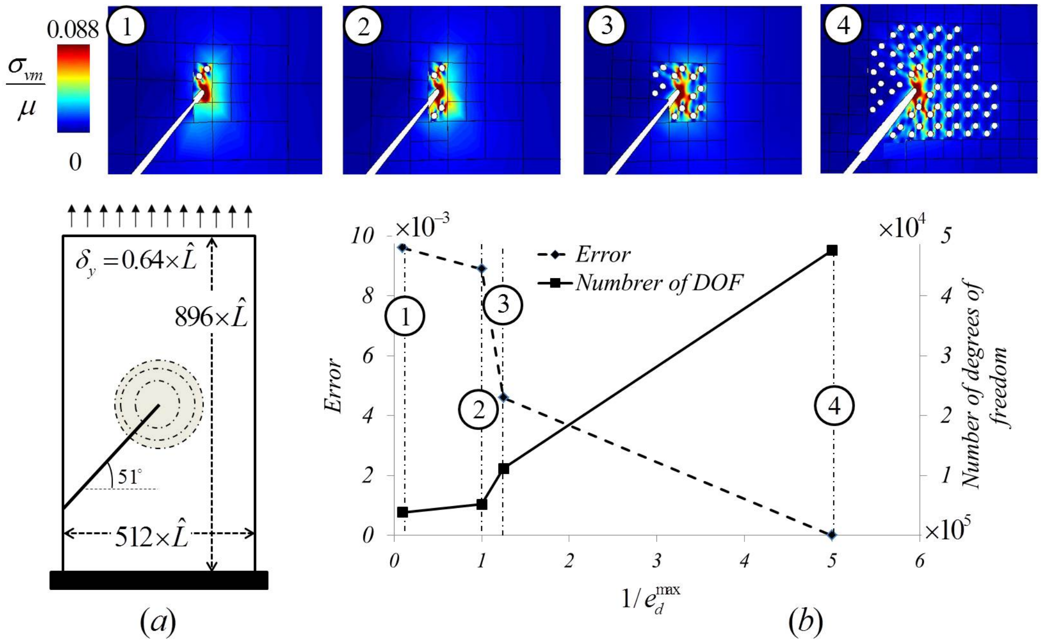

Figure 4.8: *(a) A rectangular domain with an inclined edge crack under mixed mode loading conditions. (b) Variation of the approximation error defined in* (4.18) *and computational cost for different values of* $1/e_d^{max}$. *Corresponding refinement levels and associated von-Mises (normalized by shear modulus* μ*) stresses are also depicted.*

regime after deformation. While not necessary in the case of elasticity, incremental loading becomes a requirement when the material response becomes history-dependent such as during plasticity and damage evolution. The problem of interest here consists of a rectangular domain of size $128\hat{L} \times 224\hat{L}$ containing two parallel horizontal edge cracks that are offset by a small distance $2h$, as depicted in Fig. 4.9a. The plate is then subjected to an incremental tensile vertical displacement and a fixed horizontal displacement on top and bottom boundaries. Increasing the macroscopic stretch results in the rise of the strain gradients around the two crack tips; this leads to a local mesh refinement over this region and the evolution of the resulting microscopic domain as loading increases (Fig. 4.9b). It can be observed that for large enough deformations, the microscopic region around the two cracks coalesce into single region. To illustrate the refinement procedure, we show in Fig. 4.9c the number of new unit cells added to the microscopic region for each of the four loading increments. One can observe that most of the unit cells are added to the system during second and third loading increment. This can be explained by the fact that increasing δ_y from $0.16\hat{L}$ to $0.32\hat{L}$ induces highly heterogeneous deformations in the continuum region between the two crack tips which triggers a localized macro-micro refinement in this region (Fig. 4.9d). After this point however, increasing the loading magnitude only results in little refinement since the critical region (between crack tips) is already in the microscopic domain.

Let us now investigate the convergence of multiscale refinement procedure described in section 4.4.1. For each loading increment, the ACM^2 aims at solving the elasticity problem and at refining continuum elements that display an excessive error. For each of the four loading increments, the refinement is performed until the error in all continuum elements is below the given tolerance. In this context, Fig. 4.9d and Fig. 4.9e show the number of continuum elements that are replaced with new unit cells at each refinement iteration and the associated arrangement of unit cells at each iteration during the second increment, respectively. We observe that the number of newly embedded unit cells decreases with iteration number, showing good convergence. It is also noted that the large number of iterations (6 and 5, respectively) needed for convergence at the second and third increments are due to the fact that large incremental displacements are applied. In practice, an optimal increment size must therefore be determined to limit the number of iterations and thus minimize computational cost.

4.5 Modeling localized damage and crack propagation in heterogeneous media

Modeling the physics of ductile crack deformation and propagation has always been a challenging computational problem due to its multiscale nature. Two routes can usually be taken. On the one hand, nonlinear fracture mechanics is able to relate crack propagation to concepts such as fracture energy, the resistance curve and fracture toughness, but it has been difficult to understand how microstructure affect these properties. On the other hand,

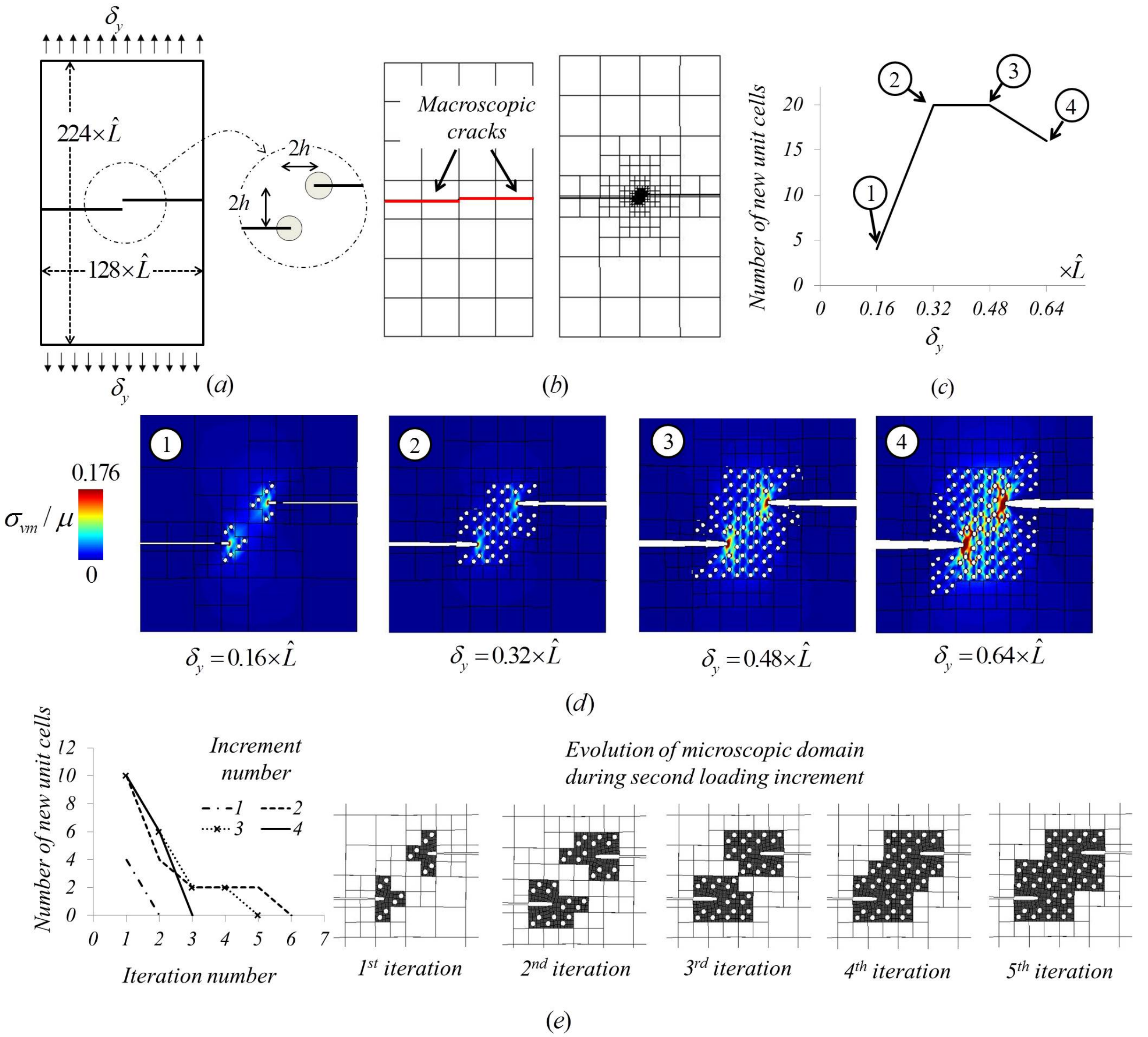

Figure 4.9: *(a) Rectangular plate with double edge cracks. (b) Initial and final discretization of the domain. (c) Number of new unit cells added for each macroscopic increment. (d) von-Misses stress field (normalized by shear modulus μ) over crack tip region at the end of each increment. (e) Number of unit cells added to the microscopic domain at each refinement iteration for different loading increments. The evolution of the microscopic domain during the second loading increment is also displayed.*

the field of damage mechanics, by taking a microstructural approach, has been successful at relating microstructural features to damage nucleation and evolution. However, the relationship between these models and fracture properties is still unclear. In this section, we address this issue by exploring the behavior of the presented multiscale model when the material is capable of undergoing damage nucleation and evolution. For this, we consider a periodic and porous microstructure whose geometry was described earlier (Fig. 4.3.a) but for which the matrix material exhibits an elastic-brittle behavior, that can be computationally captured with a lattice model [163, 171]. It is important here to note that such a lattice model is chosen for its simplicity of implementation and relevance to the problem of microstructural fracture. It is not, however, a requirement of the proposed multiscale model, in which any microscale model (atomistic, molecular dynamics or refined continuum models) could be utilized. Fig. 4.10 describes the lattice damage model considered in our study, including the mechanical response of individual one-dimensional elements, their organization and the influence of microscopic damage on the macro-scale. As depicted in Fig. 4.10a, the physical state of a lattice member is represented by two quantities: (a) its level of damage D and (b) its level of tensile stress σ. The damage D varies between 0 (when no damage is present) to the unity (when the material is totally damaged). For a brittle material, we introduce a simple law governing its evolution:

$$D = 0 \text{ if } \varepsilon < \varepsilon_c \quad \text{and} \quad D = 1 \text{ if } \varepsilon > \varepsilon_c \tag{4.19}$$

where ε_c is the critical tensile strain in the element. We note that once D has taken the value of one, it may not return to 0, regardless of the strain value. The uniaxial stress σ is then calculated with Hooke's law in the form:

$$\sigma = E(1 - D)\varepsilon \tag{4.20}$$

where E is the Young's modulus of the element. This relation clearly shows that the load carrying capacity of an element is totally lost once it is damaged (D=1). In practice, this implies that the element can be eliminated from the problem. Using first order numerical homogenization techniques [186], we also show the pre- and post-peak tensile behavior of the unit cell; one can distinguish three characteristic in the macroscopic response: (a) a linear elastic region before damage occurs, (b) a maximum stress occurring at a critical strain value approximately equal to 10^{-4} and (c) a strain-softening region that is associated with a redistribution of damage at the microscale.

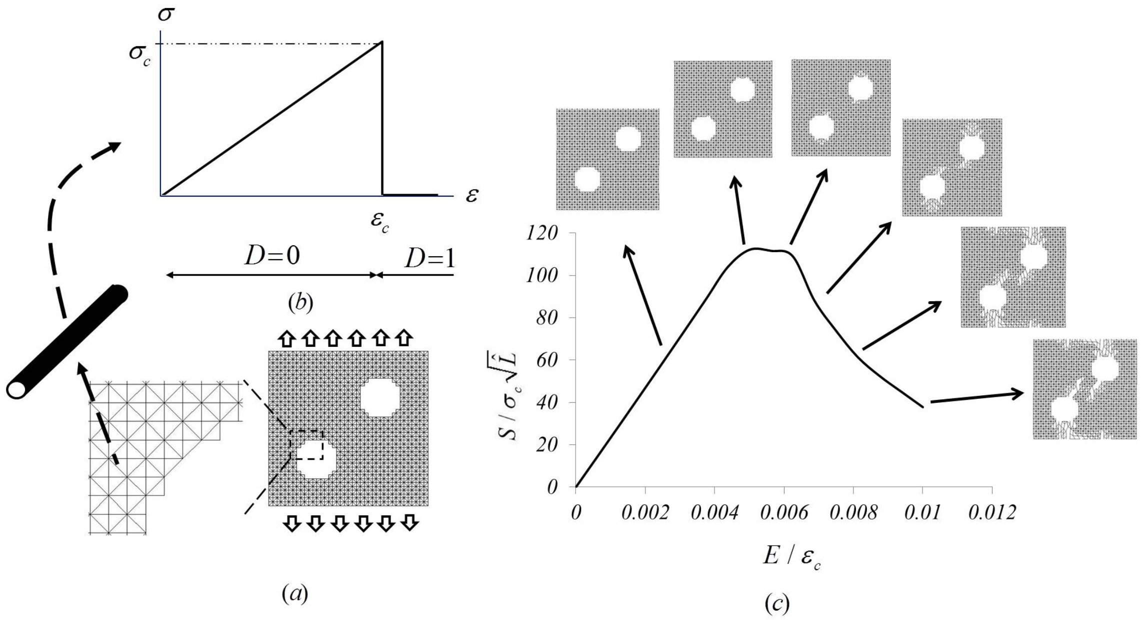

Figure 4.10: *(a) Unit cell of voided microstructure with a brittle matrix represented by a lattice model, (b) the stress strain relation and damage measure D for a lattice element, (c) The macroscopic behavior of the material under tension displaying a strain-softening region.*

It is well known in the damage mechanics literature that the strain softening response is associated to damage localization at the macroscale [166]. In other words, the post peak response does not represent the behavior of the material as a whole, but only in a localized region characterized by high strain gradients. This observation implies that homogenization is only valid before the material reaches the maximum stress or displays large strain gradients. The proposed multiscale method provides a perfect alternative for this issue since it bypasses the need for homogenization in these situations. The extension of our method to history-dependent damage model however requires an incremental procedure that is described next.

4.5.1 Incremental and adaptive formulation for history dependent material behaviors

The numerical approach relies on a nested iterative strategy as discussed in section 4.4.1. There are however two main differences in the implementation due to the inelastic response of the material. The first difference appears in the inner iterative loop to compute the displacement fields. The second difference is in the multiscale refinement techniques.the generality of the results proved

a- Predictor-corrector incremental procedure. Damage nucleation and growth are phenomena can be characterized by their nonlinear behavior and dependency on the history of prior events. For this reason, an incremental approach is critical to accurately follow the loading path and the evolution of damage at every moment during the deformation history. Several numerical strategies can be taken towards this goal. On the one hand, explicit incremental methods have been attractive due to their simple implementation; they are however known to require excessively small increments which drastically increase computational cost [127]. On the other hand, fully implicit methods (such as the Newton-Raphson and the arc-length methods [130]) can address this problem but often exhibit stability issues, especially in the context of the present strain softening material response [127]. We take here a different strategy by presenting a semi-implicit predictor-corrector approach, whose salient features can be explained as follows. Consider an initial material state, denoted by index i for which the displacement of nodes and damage in lattice elements are respectively represented by vectors $\mathbf{u}^i$ and $\mathbf{D}^i$. Starting from this state, an incremental boundary condition $\Delta\bar{\mathbf{u}}$ is applied and a solution is sought in the form $\mathbf{u}^{i+1}$ and $\mathbf{D}^{i+1}$. To determine this solution, an iterative scheme is performed in two steps. **(a) predictor step:** an elastic prediction of the displacement fields $\bar{\mathbf{u}}_p^{i+1}$ is determined by assuming that all existing lattice elements behave in an elastic manner (D=0). **(b) corrector step:** The uniaxial strain ε in lattice elements is evaluated and the previous solution is corrected by assigning a damage $D = 1$ to elements

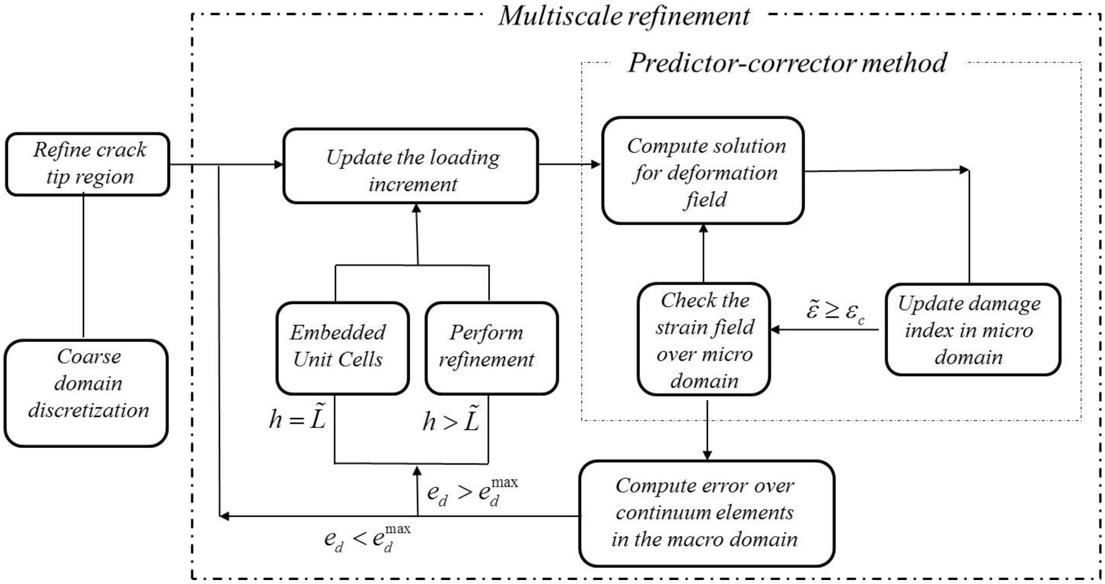

Figure 4.11: *Algorithm of the incremental formulation for multiscale refiement and damage evolution in brittle materials.*

exceeding the critical strain ε_c. A new elastic solution (predictor) is then recomputed from the newly determined damaged state and subsequently modified via the corrector step. This iterative process continues until the elastic predictor solution converges; i.e., all undamaged elements display a sub-critical strain level.

b- Multiscale refinement in the deformed configuration We now discuss some important points pertaining to the incremental refinement procedure. For this, let us consider that after N load increments, a macroscopic element e (in a deformed state) is characterized with a large computational error (both discretization and homogenization) and must undergo a transition to the unit cell description. A challenge in this situation is that the embedded unit cells must be inserted in a deformed state. This issue may be addressed in the following manner [152]. First, the nodal displacements of the macro-element are extracted and imposed on the unit cell, independent of the global simulation. A macroscopically conforming unit cell deformation can then be obtained through quasi-periodic boundary conditions developed in section 4.3.3. This deformed unit cell may then substitute the continuum element, as part of the refinement procedure. It is important to note that upon substitution of unit cells in the macroscopic domain, the force equilibrium at the boundary between the new and the pre-existing unit cells is not satisfied. This issue can be addressed by solving an intermediate elastic problem to cause forces to relax and meet global equilibrium. The details of this procedure were discussed in [152]. In addition, when the macroscopic element undergoing the transition to the microscale intersects with the crack patch, it is particularly useful to establish the relation between enriched degrees of freedom, **a** (at the macroscale) and the crack opening δ_c (in the unit cell) through the formula:

$$\delta_c = \sum_{i=1}^{9} N_i a_i, \tag{4.21}$$

where δ_c is the crack opening, N_i are the standard finite element shape functions and a_i are the values of enriched degrees of freedom. This equation follows from the X-FEM approximation of displacement fields in a macroscopic element introduced in (4.8). For more details, readers are reffed to [152].

4.5.2 Computational investigation of the role of microstructure in material toughness

The performance and predictions of the multiscale methodology are now investigated for crack propagation. Similar to the model introduced in section 4.4.3a, we consider here a single horizontal edge crack in an infinite domain, subjected to mode I (crack opening) conditions. Once again, the infinite domain is represented by a rectangular domain with dimension that are significantly larger than the size of a unit cell and subjected to incremental displacement boundary conditions that mimic the displacement fields around a crack predicted by LEFM and presented in (4.17) (Fig. 4.12a). These boundary conditions are applied incrementally by increasing the value of the stress intensity factor by amounts ΔK_I until it reaches its final value K_I^f. We also note that, although the coordinate of the crack tip changes during propagation, it is negligible compared to the size of the macroscopic domain. Consequently, we assume changes in the radial distance r appearing in (4.17) can be neglected throughout all simulations.

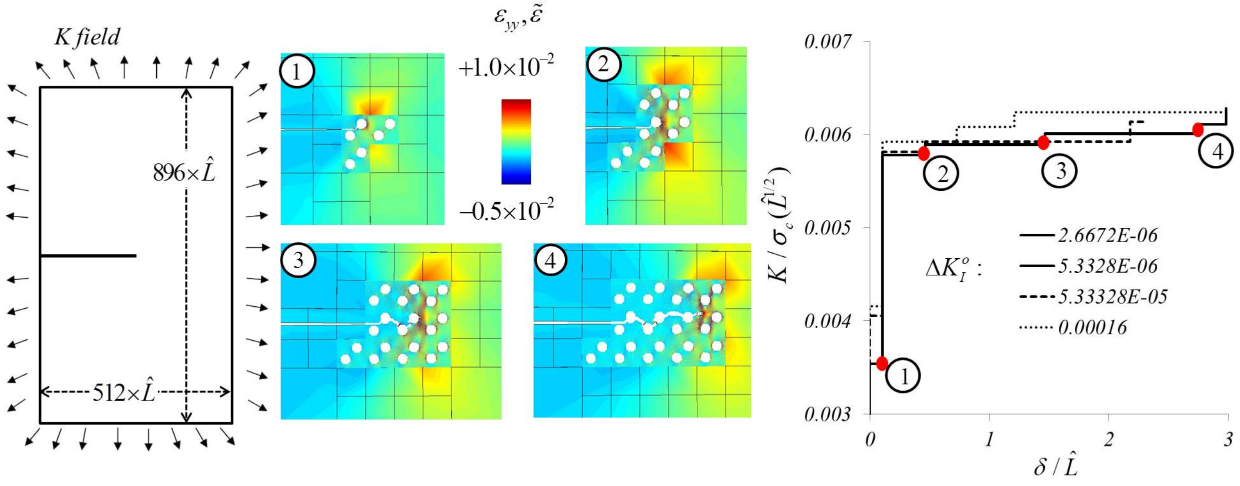

(*a*) (*b*) (*c*)

Figure 4.12: *(a) Rectangular domain with an edge crack subjected to displacement K-fields (mode I). (b) Longitudinal strain, $\tilde{\varepsilon}$, for lattice elements at the microscale and strain in yy direction at the macroscale for the different stages of crack growth shown in the R-curve. (c) Resistance curves for different increment size $\Delta K_I^o = \Delta K_I/\sigma_c\sqrt{\hat{L}}$.*

Fig. 4.12b shows the evolution of the local damage and the overall crack propagation for four distinct values of the stress intensity factor shown by circles in Fig. 4.12c. It is clear here that as the crack advances, the large strain gradients associated with the crack tip move to the right, inducing a refinement of the material description (to the microscopic level) ahead of the crack. It is therefore possible, with the proposed method, to investigate the mechanisms of crack growth over relatively long distances without knowing the crack path a priori. For such simulations, however, one sees that the size of the microscopic domain increases with crack growth, rendering the method computationally costly. This aspect can be addressed in future studies by noticing that strain gradients become small in the wake of the crack. In other words, it is potentially possible to incorporate a “coarsening” algorithm that can revert the microscopic domains to macrocopic elements in the wake of a crack. Such simulations would thus only contain a microscopic region at the crack tip, regardless of the extent of crack growth. The effect of increment size on model predictions was investigated by plotting the resistance curve (or R-curve), representing the crack extension δ with respect to the applied K_I field (Fig. 4.12c), for different values of ΔK_I. As expected, we notice that refining the increment size improves the model's accuracy until an optimal value $\Delta K_I^o = \Delta K_I/\sigma_c\sqrt{\hat{L}}$ is reached. This value is used for the remaining simulations presented in this paper.

Interestingly, the simulations predict a rising R-curve, in spite of the fact that the matrix material is brittle. This implies that the presence of voids in a brittle matrix has the capacity to change the material behavior from brittle to fracture resistant. To better understand the mechanisms at play, we show in Fig. 4.12c, the relationship between the R-curve and the state of microstructural damage ahead of the tip. We observe three interesting features: (a) the crack propagates in a step-by-step fashion by linking individual voids, (b) crack propagation between two adjacent voids occurs in an unstable brittle manner, i.e., it propagates without increasing its driving force and (c) the associated zig-zag pattern of the crack results in an increasing resistance of the material to crack propagation. These phenomena are responsible for both the overall rise of the R-curve as well as its discontinuous, stair-case aspect. To further investigate the effects of the microtructure on fracture toughness, we then propose to assess the R-curve for materials distinguished by three types of unit cells (Fig. 4.13a): (a) a matrix with large voids (volume fraction = 17.5%), (b) a matrix with small voids (volume fraction = 4.4%) and (c) a matrix with no voids. Fig. 4.13 shows the damage and stresses in the evolving microscopic domain at various stages of crack growth. As expected, the material without voids exhibits brittle, unstable fracture, typically characterized by a straight and smooth crack pattern and a flat R-curve. When small voids are present, we observe that the crack path is originally deflected by voids, a phenomenon that contributes to increasing the slope of the R-curve. Eventually, the slope decreases and fracture switches to brittle behavior. This transition can be observed on the microstructural level as the crack path becomes smoother and only connects to voids that are present in its trajectory. Finally, the material with larger voids displays a similar trend but is able to deflect the crack for a longer period. This phenomenon arises from the fact that microstructural voids display larger mechanical interactions amongst themselves and with the crack at larger volume fraction. Ultimately this contributes to delaying the onset of unstable crack propagation and thus increasing toughness.

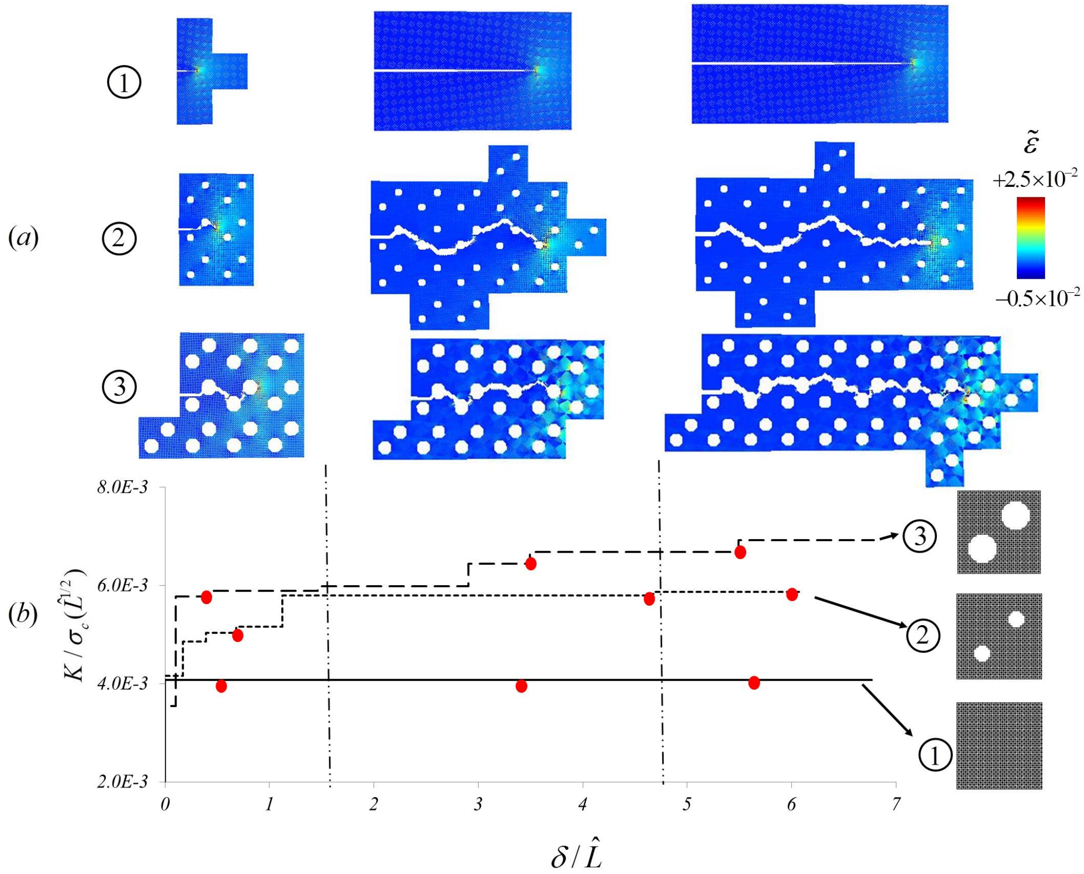

Figure 4.13: *(a) Crack growth pattern and longitudinal strain at the microscale for three different voided microstructures and (b) associated resistance curves.*

4.5.3 Crack interactions and microstructural effects

This final example aims at illustrating the potential of the ACM^2 in predicting crack growth in mixed mode conditions and capturing the interaction mechanisms between multiple growing cracks. For this, we consider the problem of two horizontal edge cracks in a rectangular domain, whose geometry is depicted in Fig. 4.9. Boundary conditions then consist of applying a vertical displacement on both top and bottom boundaries (Fig. 4.9) in an incremental manner with increment size $|\Delta_y|$. We investigate here a material whose matrix behavior follows the brittle constitutive relation introduced in (4.19) and more specifically examine two types of microstructures: (a) a matrix with no voids and (b) a porous material with larger voids (as shown in Fig. 4.10).

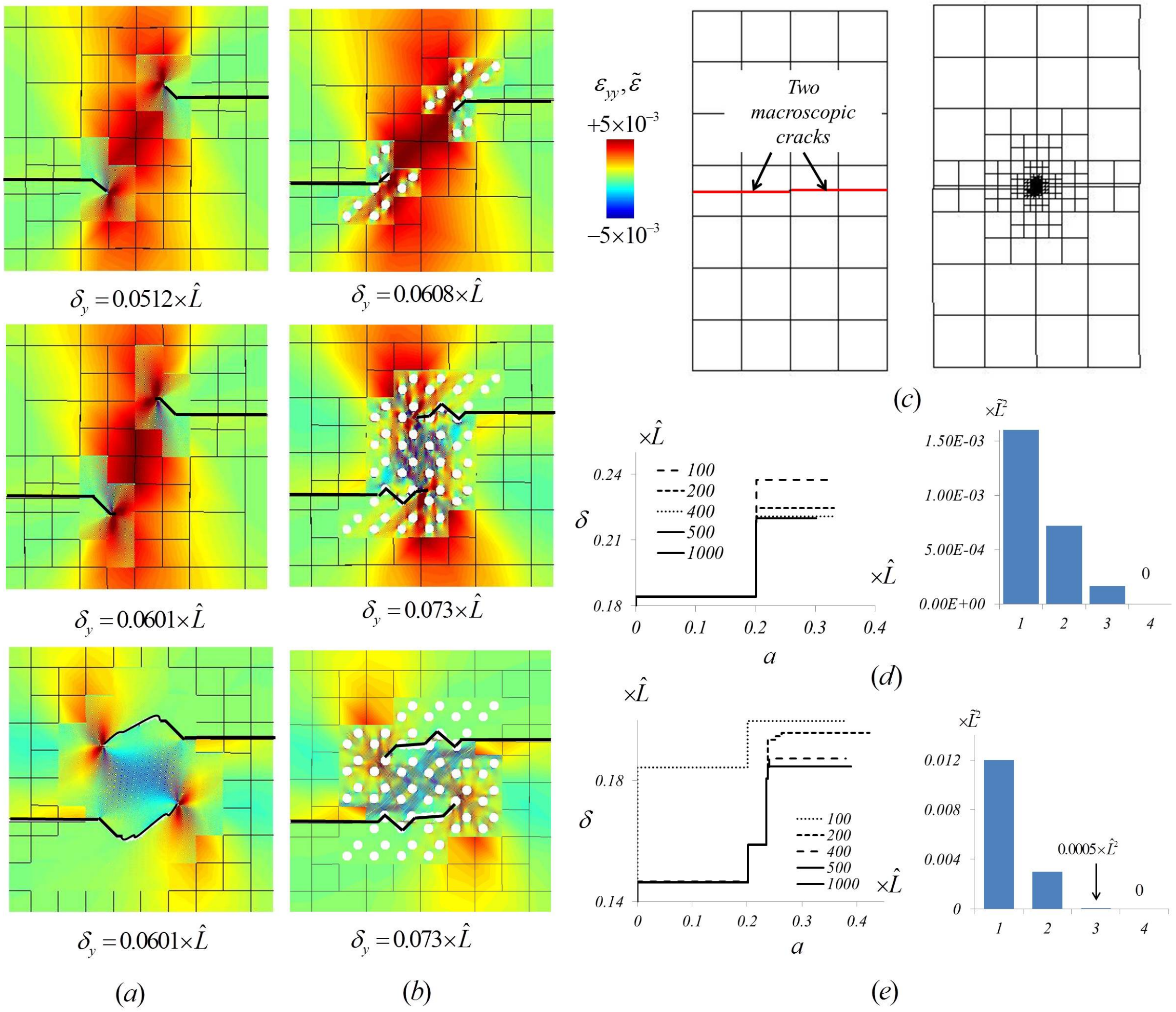

Figure 4.14: *Crack growth pattern, tensile (vertical) component of macroscopic strain fields and lattice strain in the microscopic domain, for (a) a material with no voids and (b) a voided material. (c) Initial and final discretizations. (d) and (e): Imposed displacement, δ, versus crack growth, a, and the error measure defined in (4.22) for different increment size. Plots in (d) are for a matrix with no voids and plots in (e) are for a voided matrix.*

Before we analyze the model's predictions, it is first important to present a study of the effect of incremental size on the accuracy of the solution provided by the quasi-explicit framework presented in section 4.5.1. To achieve this, we first characterized the macroscopic behavior of the system by evaluating the variation of crack growth a with an increase in external loading magnitude δ, producing a curve shown in Fig. 4.14. We then measured the convergence of the solution by evaluating how this curve changed as the size of the incremental loading $|\Delta_y|$ was refined. More specifically, we introduced an error measure e_i, in the form:

$$e_i = \int_0^{a_f} (\delta_i(a) - \delta_{i+1}(a))da \tag{4.22}$$

where the index $i = 1 : 4$ denotes the increment size ranging from 100, 200, 400, 500 and 1000, respectively, and a_f is the final crack length. The curve of variations in e with increment size (Fig. 4.14d and e), exhibits fast convergence and displays a relatively small error if 400 increments is chosen, regardless of the microstructure considered. This value was therefore used for our study.

Let us now focus on the model's predictions. Fig. 4.14 illustrates the crack growth pattern and the contours of microscopic longitudinal strain (in lattice elements) and macroscopic tensile strain ε_{yy} (in 2D continuum elements) around the crack tips. We observe that for small applied loads, the microscopic regions remain centered around the tip of each crack but do not connect into a single region. However, as the loading increases, crack growth induces an enlargement of the refined regions, which eventually connect as cracks become closer to one-another. It is interesting to note that the crack growth prediction in the uniformly brittle matrix is in excellent agreement with other (macroscopic) numerical studies on brittle materials [161]. For the alternate microstructure, however, the crack progression is affected by a variety of features including macroscopic loading conditions, the presence of adjacent cracks and the existence of micro-voids. As observed earlier, the presence of voids tend to delay the propagation of the crack by decreasing the stress intensity factor and by deflecting the trajectory of the crack.

4.6 Summary and concluding remarks

To recapitulate, we introduced an adaptive concurrent multiscale method (ACM^2) to model fracture and crack propagation in heterogeneous media. This class of phenomena have been challenging to model since their behavior depends on both macroscopic loading and microscopic damage mechanisms occurring in the crack process zone. The traditional large scale separation between these levels necessitates the introduction of new classes of multiscale approach that can maximize modeling accuracy (at both macro and micro-scales) while minimizing the computational demand. The proposed ACM^2 addresses this need by relying on a few important concepts:

- **Multiscale adaptive refinement.** To minimize the approximation error arising from discretization and homogenization procedures, an adaptive technique is presented which does not only refine macroscopic elements, but also substitutes them by a more detailed microstructural description (the unit cell) when they reach a critical size. This feature endows the ACM^2 with the capability to automatically detect and refine the material description based on the heterogeneity of the deformation.

- **Domain coupling conditions that enable the incorporation of unit cells into macroscopic FEM simulations.** A set of coupling conditions are introduced at the boundary between unit cells and macroscopic elements, enabling the existence of microscopic fluctuations at the edge of the microscopic domain. These conditions are critical to circumvent the appearance of an artificially stiff boundary at the limit between micro- and macro-scale.

- **Coupling with the extended finite element method (X-FEM) to model fracture.** We used the X-FEM enrichment functions to naturally enable the transition between the discontinuous displacement fields along a macroscopic crack and their more complex form at the microscale.

The combination of these features enables a dual description of fracture in the form of a detailed microstructural modeling of a material in the complex and highly heterogeneous process zone ahead of the crack and a coarse grained continuum description in regions that undergo homogeneous deformation. The paper also introduced a nonlinear finite deformation formulation of the mechanical problem in order to investigate, with high accuracy, the large deformations arising in the neighborhood of a loaded cracks. The proposed strategy is based on a nested incremental procedure that alternates between finding a solution for the mechanical problem and minimizing the approximation error via multiscale refinement. We showed, through examples, that adaptivity is critical in the context of fracture as it enables the microscopic domain to naturally evolve with material's deformation and damage. We finally presented a number of examples that illustrated the accuracy, the computational cost and the ability of ACM^2 to capture crack growth in different microstructures. Although the paper did not aim at predicting the behavior of real materials, the generality of the results proved that the method can be later used to capture realistic material behavior such as nanoscale effects [188], plastic deformation [145] and the effects of interstitial fluid flow in cracks [183, 182], for instance. Furthermore, while not addressed in our study, the problem of crack nucleation in a macroscopic specimen could be implemented using global microstructural statistical information and the associated stress/strain at nucleation. Such methods have been investigated in [151], for instance.

Besides the numerical aspect, it is worth mentioning that the development of methods such as the ACM^2 is an important step toward reconciling the fields of damage and fracture mechanics, which have been traditionally separated by their disparate length-scales. More particularly, since the explicit microstructure is considered ahead of a crack, the existence of a complex process zone and the associated size effects can be accurately captured. Such methods may therefore provide a better understanding of fracture size effects in ductile and quasi-brittle materials in a near future. To illustrate this point, we presented examples of a porous material whose matrix was represented with a lattice model characterized by a simplistic damage model. We have shown that the ACM^2 was capable of predicting the fracture resistance curve associated with these materials and thus predict fracture toughness based on microstructural arguments. It should be noted, however, that the assumption of structural periodicity may be unrealistic at this point and that the extension to the concept of ”Representative Volume Element” for fully random microstructures is still an open question. Nevertheless, with further developments, this class of methods can potentially be used to investigate and optimize the effect of microstructure on fracture toughness, which, in the longer term should make “in-silico” material design a reality.

Chapter 5

ACM^2 for size effect problem in microstructured material

5.1 Introduction

Understanding the mechanical behavior of materials during fracture is vital for explaining the observed size effect problem and also necessary to formulate an appropriate numerical framework. In this part we aim to mainly focus on the behavior of structural materials such as concrete. The fracture process and failure of concrete strongly depends on its internal structure. In fact, at the nanoscale failure of the mortar matrix is associated with voids and fine particles and at the microscopic length scale, it is generally accepted that fracture of concrete is due to the micro-cracking process. At this length scale, prior to failure micro cracks form in the region ahead of the crack tip, that is known as fracture process zone (FPZ), and from this point, the material dissipates its internal strain energy that is induced by external loading via two mechanisms. One possible scenario is to dissipate energy through new micro cracking procedure, and the other possible mechanism is deformation or propagation of existing micro cracks. As a result micro cracks link together to form macro cracks in the FPZ during the failure of the material. By increasing the external loading this procedure continues until one or more macro cracks become unstable and tend to propagate without increasing the external loading.

Transition between micro cracking and macro cracking involves different damage processes, and controls the fracture behavior of concrete. It is important to understand such

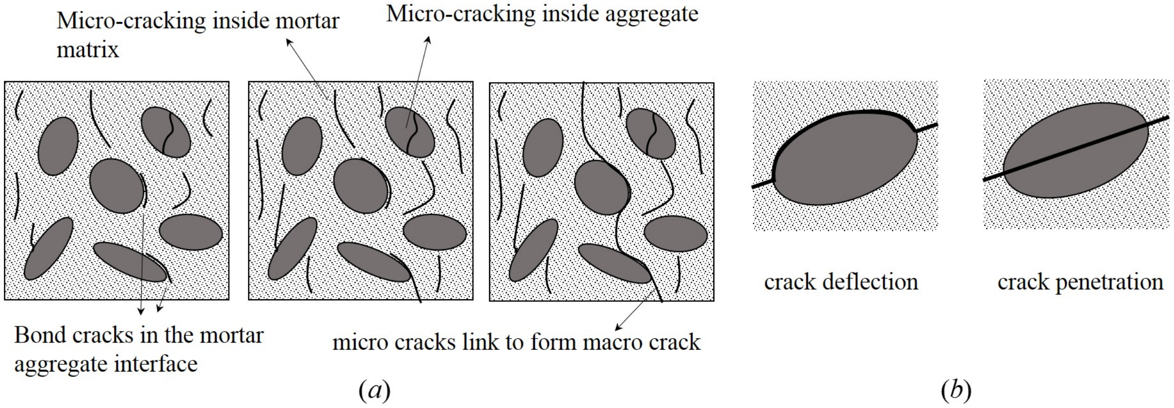

Figure 5.1: *(a) Micro cracks spread and form macro cracks in composite material, (b) deflection and penetration of cracks when impinging to an aggregate.*

mechanisms in order to design an appropriate numerical model. In microscopic scale (which refers to the length scale that material heterogeneities reside) concrete should be seen as a three phase material which consists of mortar, aggregate and the bond between mortar and aggregate. Prior to the failure of the material, at this length scale the micro cracking could happen in each phase individually, as shown in Fig. 5.1a. In the internal structure of normal strength concrete, which is is known as quasi brittle material and mostly used in structural elements, the mortar aggregate bond is known to be the "weakest link". This attribute strongly affects the size of FPZ and crack propagating path as discussed in the following. Due to relatively weak bond between mortar and aggregate in this type of concrete micro cracking occur over a relatively large region ahead of the crack tip. Based on the same reason when a propagating crack impinges an aggregate instead of cracking the aggregate the crack links to the micro cracks that already exist in the interfacial zone. That is, the crack finds its propagating path by deflecting around the aggregate and therefore, takes a *zig-zag* pattern to propagate. These two characteristics of normal strength concrete explain its quasi brittle behavior. On the other hand, in high strength concrete the mortar-aggregate interface is much stronger than the aggregate and also the mortar material. Therefore, a propagating crack will intersect everything on its path and tend to propagate on a straight path which results in brittle fracture.

The objective of this discussion is to highlight the effect of the microstructural properties of materials, especially concrete-like material, on their overall fracture behavior. Typically, concrete-like material are characterized by a nonlinear response with a softening post peak behavior. To investigate this behavior we aim to model the failure of a concrete-like heterogeneous material that consists of mortar, aggregate and interface phases. The material is also assumed to be periodic at the micosopic level and its basic building blocks is represented by a unit cell of side length $\hat{L}$. The geometry and configuration of aggregates are shown in Fig. 5.2a. Both mortar and aggregate material are modeled by a lattice that consists of beam elements with the pattern that is shown in Fig. 5.2a. The fracture of each phase could then be modeled as follows; For each phase the physical state of individual lattice elements is described by the quantity of damage D, as:

$$D = 0 \ \text{ if } \ \sigma_{eff} < \sigma_c \quad \text{ and } \quad D = 1 \ \text{ if } \ \sigma_{eff} > \sigma_c \tag{5.1}$$

where σ_{eff} denotes the effective tensile stress and σ_c is maximum allowable tensile stress. For beam element σ_{eff} is written as:

$$\sigma_{eff} = \frac{N}{A} + \alpha \frac{|M|}{W}, \qquad 0 < \alpha < 1. \tag{5.2}$$

where N, M and W are respectively, tensile force, bending moment and cross section modulus of individual beam elements (Fig. 5.2b). Also, α is a coefficient that limits the effect of bending on the damage index. Fig. 5.2b shows the load carrying capacity and damage index of individual elements. In addition, the mortar-aggregate interface, is modeled via zero thickness interface elements, the geometry of which is shown in Fig.5.2c. The interface elements are characterized by linear stress-displacement relation in normal and tangential directions as shown in Fig. 5.2c. The physical state of each interface element can also be

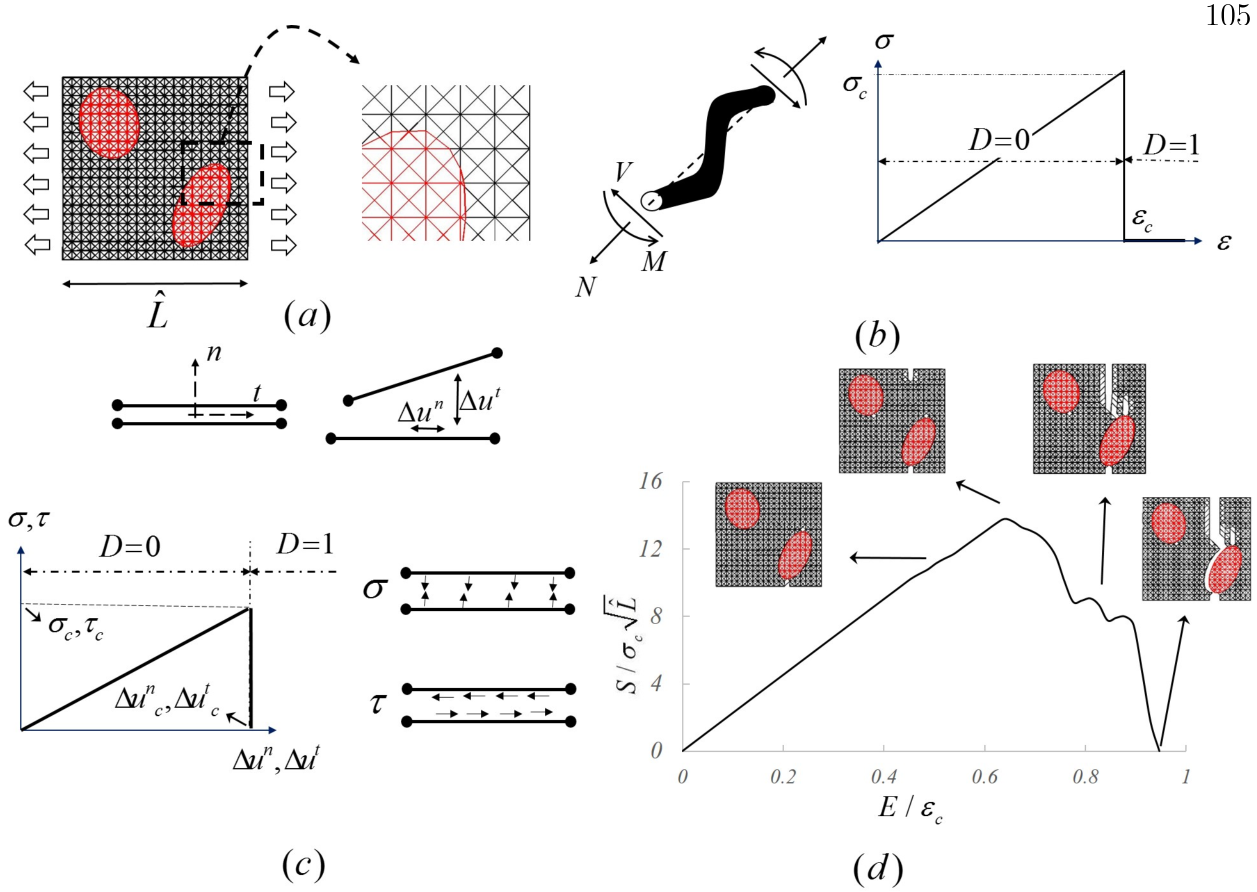

Figure 5.2: *(a) Unit cell of three phase material consists of brittle matrices and interface. The mortar and aggregate material are represented by lattice model that is characterized by brittle fracture shown in (b). The mortar-aggregate interface is represented by zero thickness elements with stress displacement relation shown in (c). (d) The macroscopic behavior of the material under tension displaying a strain-softening region.*

described as:

$$D = 0 \ \text{ if } \ \left(\Delta u^n < \Delta u^n_c,\ \Delta u^t < \Delta u^t_c\right) \quad \text{and} \quad D = 1 \ \text{ if } \ \left(\Delta u^n > \Delta u^n_c \text{ or } \Delta u^t > \Delta u^t_c\right) \quad (5.3)$$

Where Δu^n and Δu^t define opening of interface element in normal and tangential directions. Also Δu^n and Δu^t are critical opening of interface when the bonding between mortar and aggregates fails. One should note that once $D = 1$ for any individual element, the load carrying capacity of such element vanishes and it may not be returned to 0. This is equivalent to eliminating that element from the lattice structure. It may not return to

$D = 0$ and load carrying capacity of element vanishes. This is equivalent to eliminating these elements from lattice structure that represents damage nucleation and crack propagation. The macroscopic stress strain response of this unit cell is also shown in Fig. 5.2.d. Based on this figure, nucleation of damage starts when $E_{11}/\epsilon_c \approx 0.45$. Prior to this point the macroscopic response is linear and elastic. After this point the micro cracking procedure continues. As a result the material responds nonlinearly until it reaches to its ultimate load carrying capacity. At this time the macro cracks have already formed inside the unit cell and propagate until the material fail to response to external loading. In this example it is also shown how the weak link interface can deflect the crack propagation path.

Understanding the failure mechanism at this length scale in quasi-brittle material, such as concrete, also helps to explain the observed size effect phenomenon. As discussed in (1.4) the size effect problem is related to the existing characteristic length that is associated to the size of FPZ. In fact, the size of heterogeneities such as aggregate size in concrete, controls the FPZ size. For instance, it is well known that the width of FPZ in concrete is equal to $3d_A$, where d_A is the average aggregate size [110]. This has been verified by abundant experimental test results in the literature. One may note that when the specimen's size is large compared to the internal heterogeneities, the FPZ occupies a relatively small region in front of the crack tip. This is in good agreement with the LEFM assumption that the FPZ is infinitesimally small and attached to the crack tip. Therefore, when the structure size is very large compared to the aggregates size the nominal strength follows the rule that is proposed by LEFM and the material's response is brittle. On the other hand, when the structure size is comparable to the aggregates size, the FPZ occupies a relatively large region which violates the LEFM assumption. In fact, for such structure the micro cracks extend into a relatively large domain which is in good agreement with the assumptions of plasticity theory and justifies the ductile behavior of material. Finally, when the structure size is nor large neither small, compared to the size of the aggregates, the material shows a quasi-brittle behavior and its nominal strength follows the function that is previously shown in Chapter one.

The main purpose of this chapter is to study the size effect problem in concrete-like heterogeneous material by means of ACM^2. The suitability and accuracy of the method for investigating such problems has been illustrated in previous chapters. In the next section we recapitulate the basic formulation of the method. Next we demonstrate the size effect problem via a numerical example. We also discuss about the potential of the method for future research in last section.

5.2 Recapitulation of ACM^2 and stress driven refinement

The main idea underlying the ACM^2 is to split the material domain into two regions with different resolution of description, namely, macroscopic(continuum) and microscopic (lattice, continuum or molecular dynamic or *etc*) domains. Formulated in a finite element framework, this method combines adaptive refinement and embedded unit cell concepts to satisfy the efficiency and the accuracy of numerical model. In this section we aim to recapitulate these concepts briefly and introduce a new idea for transition from macroscopic scale to microscopic scale. For this let us consider a three point bending specimen with a crack in the middle of the specimen, Fig. 5.3a. The material is assumed to be heterogeneous and periodic at the microscopic scale. For simplicity, it is assumed that a symmetric unit cell with a circular inclusion, with 15% volume fraction, at its center with side length of $\hat{L} = \frac{1}{16}$ represent the building blocks of material in the microscopic scale, Fig. 5.3b. The ACM^2 suggests that the continuum assumption is valid and accurate in regions far from ahead of the crack tip and for such material the constitutive relation can be found by performing first order homogenization technique. The method then proposes to embed the unit cells in the fracture process zone to accurately capture the heterogeneous deformation field in the microscopic scale.

In this method the transition from continuum approximation to the exact microscopic description of material relies on evaluating certain types of error in element level and subsequently refining the finite element mesh if certain condition is met [185, 152, 119]. If the refinement is not possible, that is the finite element side length has reached a certain length, the method proposes to replace the finite element with a unit cell. The basic idea of this procedure is built upon the fact that two types of error exist in any finite element model that is based on continuum description of material. The first type of error, known as discretization error e_d, defines the difference between exact and approximate numerical solution. In [185], it is shown that e_d directly depends on the size of an element and second gradient of deformation field over its domain, $\|\nabla\nabla u\|$, *i.e.* $e_d \propto h\|\nabla\nabla u\|$. Based on this definition when the deformation field is highly heterogeneous, the finite element size should be small enough to preserve numerical accuracy. Accordingly, when a sharp discontinuity such as a crack tip exists, since the second gradient of the displacement field is singular, the finite element size should asymptotically reach to zero at the crack tip. A disparity then arises since, the continuum assumption, for a microstructurally heterogeneous material, is not valid at every length scales based on following explanations. A continuum assumption for material is based on a constitutive relation that is derived from homogenization theory. A homogenized model relies on the truncated Taylor series of strain energy approximation. Therefore, when the deformation gradient field deviates from unity, that is the higher order strain terms become comparable to the first order strain term, the accuracy of the continuum approximation becomes questionable. The homogenization error e_h, quantifies the loss of accuracy of continuum theory for such material. In [185] it is shown that e_h depends on characteristic length of material micro structure, the side length of unit cell element $\hat{L}$ which is also related to the size of material heterogeneities, and second gradient of displacement, $\nabla\nabla u$, *i.e.* $e_h \propto \hat{L}\|\nabla\nabla u\|$. By defining maximum allowable discretization and homogenization errors e_d^{max} and e_h^{max}, one can calculate the critical continuum element size as below

[185]:

$$h^c = \alpha \hat{L}, \qquad \text{where} \qquad \alpha = \frac{\sqrt{12} e_d^{max}}{e_h^{max}}. \tag{5.4}$$

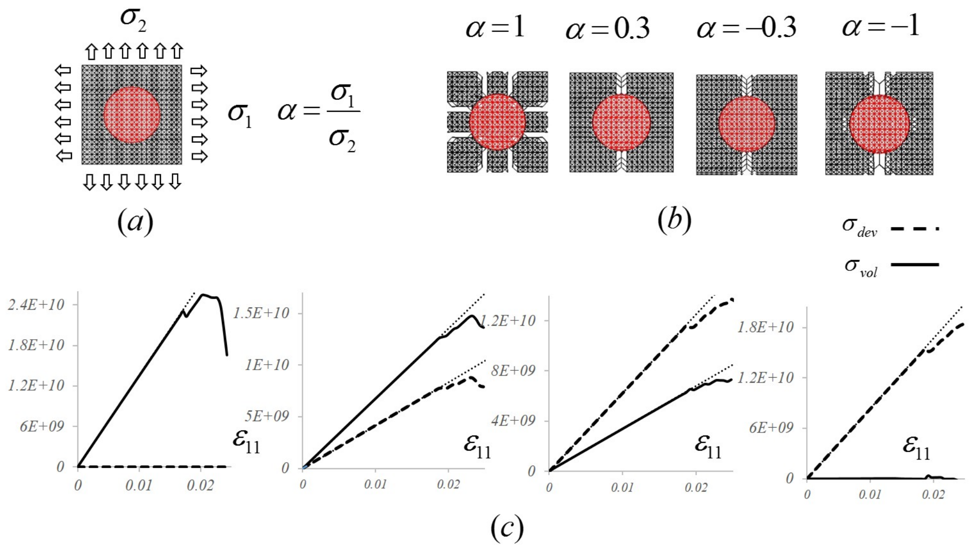

Figure 5.3: *(a) The symmetric unit cell and applied loading (b) configuration of localized damage at when unit cell has completely lost the load carrying capacity for different stress states, (c) the macroscopic volumetric and von-misses stress versus macroscopic strain.*

One can then interpret the above discussion as follows; once an element size becomes equal or less than critical element size, as a result of local mesh refinement, the continuum assumption is not valid and the element should be replaced by a unit cell. Consequently, the material domain consists of unit cells that are embedded in macroscopic finite elements region. The issue here is that the unit cells and macro scale elements represent the material at two different length scales and appropriate coupling conditions should be formulated. These conditions should satisfy the kinematic and force equilibrium between two domains. Readers are referred to [185, 119] for details of possible coupling conditions and pros and cons of each of them. In previous chapters, a detailed discussion about the numerical implementation including elastic crack model, iterative solution associated with finite deformation model and most importantly modeling localized damage and crack propagation for history dependent material is given. In this part we would like to introduce a new refinement criteria which plays an important role in the accuracy of local mesh refinement and transition between continuum and exact description of the material. As discussed above, in ACM^2 the local mesh refinement is based on evaluating the discretization error, $\|\nabla\nabla u\|$, over a macroscopic element domain and comparing it to a critical value to ensure numerical accuracy. However, this type of error only quantifies the accuracy of the numerical methodology and does not guarantee the soundness and validity of continuum assumption. In addition, defining the maximum allowable discretization error is not a trivial work as shown in previous chapter. Let us consider a unit cell of a heterogeneous material with side length of $\hat{L}$. Based on homogenization theory this unit cell can be replaced by a continuum element of the same size if the deformation field over the continuum domain is uniform. However, it should be noted that there are some situations that the material undergoes uniform displacement but the continuum assumption could not be valid due to the nucleation of localized damage in the microstructure of the material. Some examples of this situation are shown in Fig. 5.3 where the unit cell is superimposed on a continuum element and a deformation field such that $\|\nabla\nabla u\| = 0$, is applied on it. The deformation is applied in an incremental manner through 1000 increments. Fig. 5.3c shows the variation of macroscopic volumetric and deviatoric components of 2nd Piola-Kirchhoff stress tensor versus the xx component of Green-Lagrange strain tensor for each case. For each case the material response has three important characteristic: 1) initially the material is linear, 2) after first damage nucleation at the microscopic level the material responses non-linearly until it reaches to its maximum load carrying capacity, 3) post peak softening softening behavior that is due to the unstable crack propagation before failure. These examples clearly shows that the continuum assumption cannot be valid if the stress state in an element is beyond a critical value. An appropriate criteria might be written in the form of stress envelope that defines all possible stress states that result in nucleation of damage in microstructure. To obtain such envelope we propose to perform several different case that satisfies $\|\nabla\nabla u\| = 0$ and find out the $(\sigma_{dev}, \sigma_{vol})$ pair that shows the initiation of crack nucleation in the microstructure. The failure envelope is then defined by interpolating a function from these sampling point in $(\sigma_{dev}, \sigma_{vol})$ plane. Fig.5.4a shows these values for the simulations in Fig. 5.3b and c. For this material we found:

$$f(\sigma_{vol}, \sigma_{dev}) = \frac{1.504}{2.306}\sigma_{vol} + \sigma_{dev} - 1.504 \times 10^{12} \tag{5.5}$$

This envelope can then be used as a criteria for refining macroscopic elements as follows: once the stress state at any sampling point over the continuum element domain, such as integration points, meets the failure criteria (that is $f(\sigma^s_{dev}, \sigma^s_{vol}) \geq 0$) the constitutive relation derived from first order homogenization theory loses its validity, and therefore, the element should be refined or replaced by a unit cell, if its side length is equal to that of unit cell. It should also be noted that for material with random heterogeneities such as concrete, it is possible to define several unit cells with random distribution of heterogeneities and derive the failure envelope $f_1, f_2, ...$ that shows the micro damage nucleation for each case. The final failure envelope f, can then be defined by averaging out these functions. This is shown schematically in Fig. 5.4.

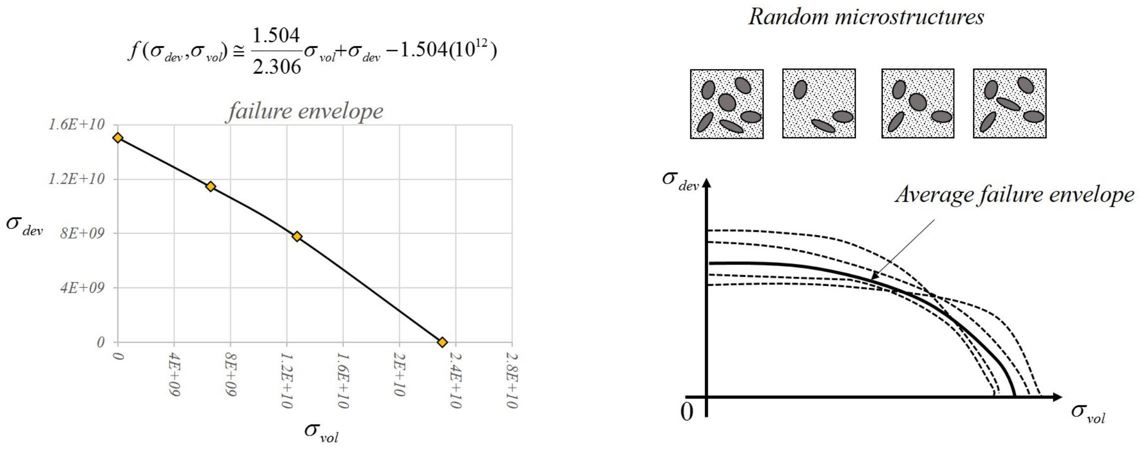

(*a*) (*b*)

Figure 5.4: *(a) The failure envelope for symmetric unit cell shown in Fig 4, (b) For material with random heterogeneities, the failure envelope is the average of different unit cells failure envelope.*

5.3 Numerical simulation

In this section we use the proposed methodology as a tool to investigate the effect of macroscopic structure's size on the fracture of a material. Here we consider a microstructurally heterogeneous material that consists of three different phases including mortar, aggregate and interface between mortar and aggregate. For simplicity we also assume that the material is periodic, in the microscopic length scale, and a unit cell of side length $\hat{L} = \frac{1}{16}$ representing the material's microstructure is shown in Fig. 5.6. A lattice model is used to describe the material structure at this length scale. Each unit cell consists of two aggregates that are equal in size that are centered at $(+0.16\hat{L}, -0.25\hat{L})$ and $(-0.20\hat{L}, +0.25\hat{L})$. Both aggregates are elliptical with major and minor axis of $0.25 \times \hat{L}$ and $0.13 \times \hat{L}$ with volume fraction of 0.15%. At mesocopic scale a lattice based model is used to describe the material. The mortar and aggregate material are represented by microscopic beam elements with the properties given in Fig. 5.6. Also zero thickness interface elements were used to model the mortar aggregate interface zone. The location of interface is defined by means of level set method. To model damage nucleation and crack propagation we utilized the damage model described in Fig. 5.6 with $\sigma_c = 10^{11}$, $\alpha = 0.5$ for beam elements and $\Delta u_c = \Delta u_t = \hat{L}/60$ for interface elements. On macroscopic scale the material is continuum and its lame constants derived from the first order homogenization technique are equal to $\tilde{\lambda} = 3.3 \times 10^{11}$ and $\tilde{\mu} = 8.86 \times 10^{10}$.

5.3.1 Accuracy of the method:

Let us first asses the accuracy of the proposed method for predicting crack propagation path and estimating ultimate load carrying capacity of a structure compared to a fully microstructured analysis (BF). For this we consider a three point bending specimen of size $(8\hat{L} \times 4\hat{L})$ that is constrained at the bottom corners and a concentrated load is applied at the middle of the top edge in downward direction, FIg. 5.5a. The plate is also characterized with a vertical crack of length $2 \times \hat{L}$ that is located with a tiny offset of $\delta_{offset} = 10^{-5}$ from the symmetry line. This offset is chosen to prevent intersecting the crack and macroscopic elements nodes, which is crucial in XFEM framework. The external load is applied trough 300000 predictor-editor loading increments that is explained in details in [119]. Fig. 5.6 shows formation and evolution of localized damage until the ultimate load carrying capacity is reached for both simulations at different stages of simulation. Both methods predict that the nucleation of damage, on the mesoscopic scale from the tip of the preexisting crack, takes place at $262,500$th increment. At this load increment the predictor-editor solution method is enabled to capture the correct crack propagation path and as a result the crack continues to propagate until failure of the structure is reached without any change at the macroscopic force. This implies that the material cannot resist to the propagation of the crack after its initiation which means that the material is brittle such as its mesoscopic scale constituents matrix material, inclusions and interface between matrix and inclusions. It is also obvious from this The relation between the material resistance and the situation of damage that is known as R-curve is shown in Fig. 5.7a with solid line.

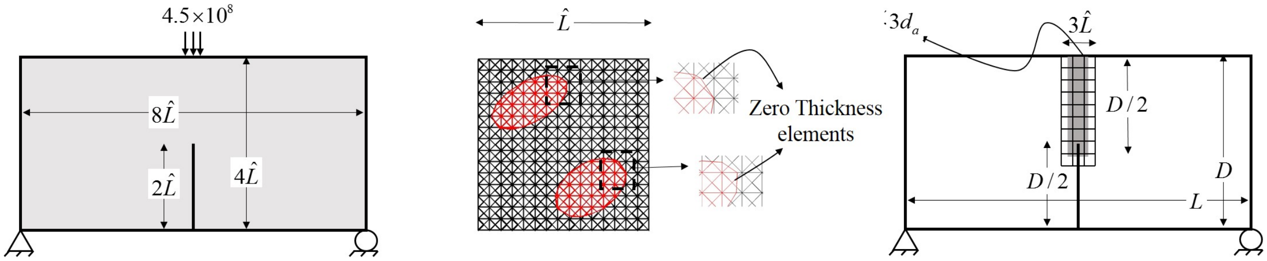

(a) (b) (c)

Figure 5.5: *(a) Three point bending specimen characterized by a vertical crack on the symmetry line, (b) Unit cell representing the microstructure of the material, (c) The geometry of the process zone in front of the crack tip.*

During the cracking procedure, the localized damage first inclines toward the inclusion ahead of the preexisting crack tip and links to the interface zone around it. As shown in Fig 5.6c, micro cracks also initiate around the other inclusion and link to the crack at next step.

After this point the crack tends to branch into two parts and propagates to eventually reach to the top edge of the specimen that results in the failure of the structure. Obviously this propagation pattern is due to the presence of heterogeneities on the mesoscopic scale which enables material to dissipate the external energy in a larger area that is called process zone. It is important to note that although the material shows brittle behavior, the non-straight propagation pattern as well as crack branching are characteristics of ductile material. This illustrates the capability of material to alter its behavior from brittle to ductile, if certain conditions are met.

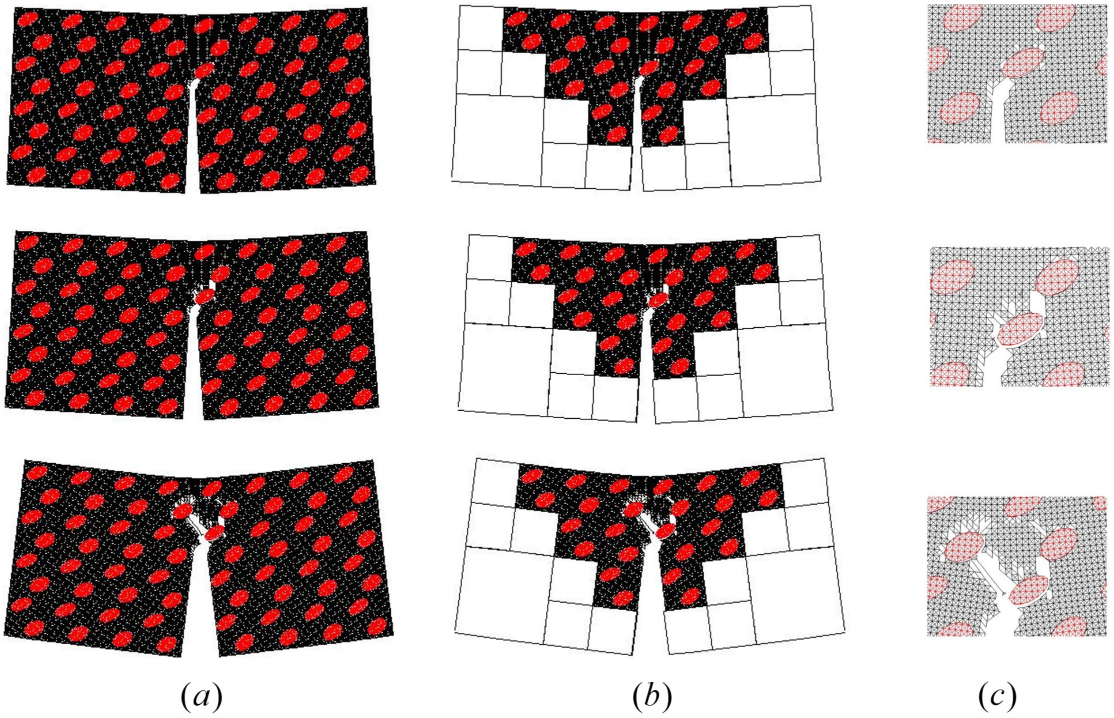

Figure 5.6: *Initiation and propagation of crack in point bending specimen predicted by: (a) brute force analysis and (b) ACM*^{2}*, (c) damage distribution in microscale near the crack tip.*

Let us now asses the efficiency of the ACM^2 method. For this we define the computational gain as the ratio of the number of degrees of freedom in a BF analysis to that of ACM^2 analysis, $n_{dof}^{BF}/n_{dof}^{ACM^2}$. Approximately this ratio is equal to $n_{uc}^{BF}/n_{uc}^{ACM^2}$, where n_{uc}^{BF} and $n_{uc}^{ACM^2}$ are number of unit cells that exist in a BF and ACM^2 analysis, respectively.

For this example, the computational gain of the ACM^2 method is equal to $11/27 \approx 2.45$, which means that the ACM^2 reproduces exactly the results obtained by BF analysis but at approximately 2.5 times lower cost. Let us now asses how the numerical efficiency will change for larger specimens. Based on crack band theory [101], for a concrete-like heterogeneous material the width of the crack band, where the micro mechanisms that lead to the failure of material takes place, is limited to $3d_a$, d_a being the average aggregate size. In the context of ACM^2, the microscopic domain will then looks like a strip of size $3\hat{L} \times l_{pz}$, where l_{pz} is the length of process zone ahead of the preexisting crack and is equal to $D/2$. Therefore, for any ACM^2 simulation the computational cost could roughly be approximated by $3D/2\hat{L}$. In addition, the computational cost for each BF analysis is approximately equal to $LD/\hat{L}^2$. The efficiency of the method based on above definition is then equal to $3\hat{L}/2L$. When the structure's size becomes very large compared to the characteristic length of the mesostructure, that is when $\hat{L}/L << 1$, the tractability of the BF analysis becomes questionable. However, the ACM^2 method reproduces the same results by incorporating just a tiny fraction of the BF simulation computational cost. This feature enables us to study the size effect problem at a reasonable cost when the structure size is much larger than the heterogeneities characteristic length.

5.3.2 Size effect on the strength of the material:

The main objective of this example is to illustrate the effect of structure size on the nominal strength of a heterogeneous material. For this we consider three structures with similar geometry (Fig. 5.7) and different sizes consisting $4\hat{L}\hat{L}$, $6\hat{L}\hat{L}$ and $8\hat{L}\hat{L}$. The material is assumed to be periodic and heterogeneous on the mesoscopic level with properties that is described in previous example. For each case the external load is applied through $300,000$ increments. The variation of external load versus crack length (R-curve) are shown for each simulation in Fig. 5.7a. The ultimate load carrying capacity P^N, which is the maximum value of each R-curve, is reached when the crack unstably grows without any change in external loading. The nominal strength of the material is then defined as $\sigma^N = \frac{P^N}{D}$. Fig. 5.7b shows the variation of the nominal strength versus the characteristic length of the specimen, D. This graph is in good agreement with experimental data reported in [101], that is the nominal strength of the material degenerates by increasing the characteristic length of the structure.

For each structure Fig.5.8 shows the formation and evolution of the damage in different stages that are shown with red circle in Fig. 5.7.

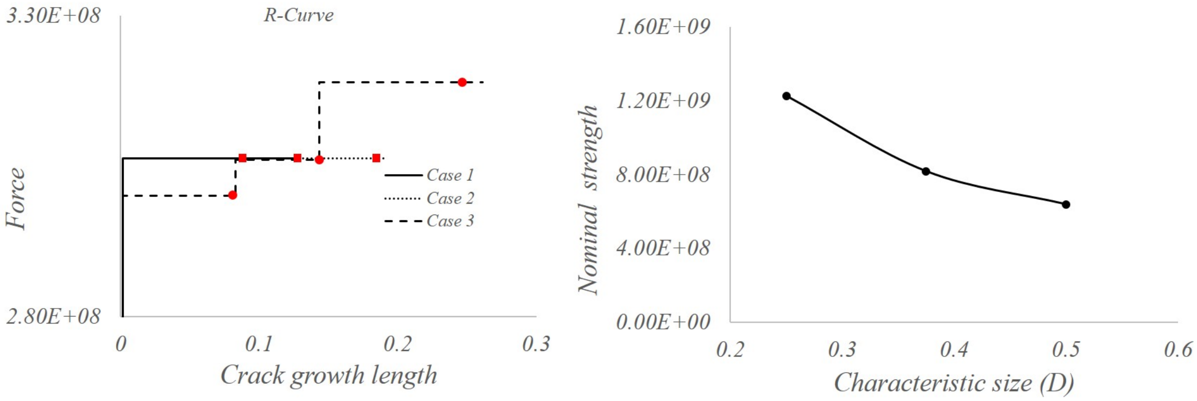

(a) (b)

Figure 5.7: *(a) R-curve of the material for different cases, (b) Variation of nominal strength versus the characteristic size of structure (D).*

For the smallest specimen the evolution of damage is shown in different stages in Fig. 5.6. For the two other cases, Fig. 5.8 shows the microscopic damage situation at different stages that are shown with red circles in Fig. 5.7a. The materials R-curve for the small specimen is a step function, that is by reaching the ultimate load capacity the driving force is enough to initiate damage nucleation and propagation until the structure fails. As discussed in previous examples this means that the material is brittle such as its constituents, matrix material, inclusions and the interface between these two phases. The R-curve for the second specimen is the same as the first one but it should be noted that for this case the nominal strength is different than that of the first case since the size of structure is different. Interestingly, the R-curve for the third specimen is a stair-step type function which is a prominent characteristic of ductile failure. In this case, to locally dissipate energy, in each step the crack propagates in a brittle manner until the material gains resistance against driving force or the ultimate failure is reached. This phenomena is again due to the presence of heterogeneities on the mesoscopic scale which ensures that the crack propagates in a "zig-zag" pattern also by linking to aggregates interfacial zones and going around the aggregates in order to raise the resistance of material against crack driving force. However, it should be noted that this characteristic of material is enabled when the structure is large enough. This example clearly illustrates how the behavior of material fracture could transit from brittle to ductile failure by varying the size of the structure. It should also be noted that since the strength of interfacial zone is lower than that of inclusions or mortar material, when the crack impinges an inclusion it tends to link to the interfacial zone rather than penetrating into it. In fact, the property of the interfacial zone plays and important role on the overall behavior of the material.

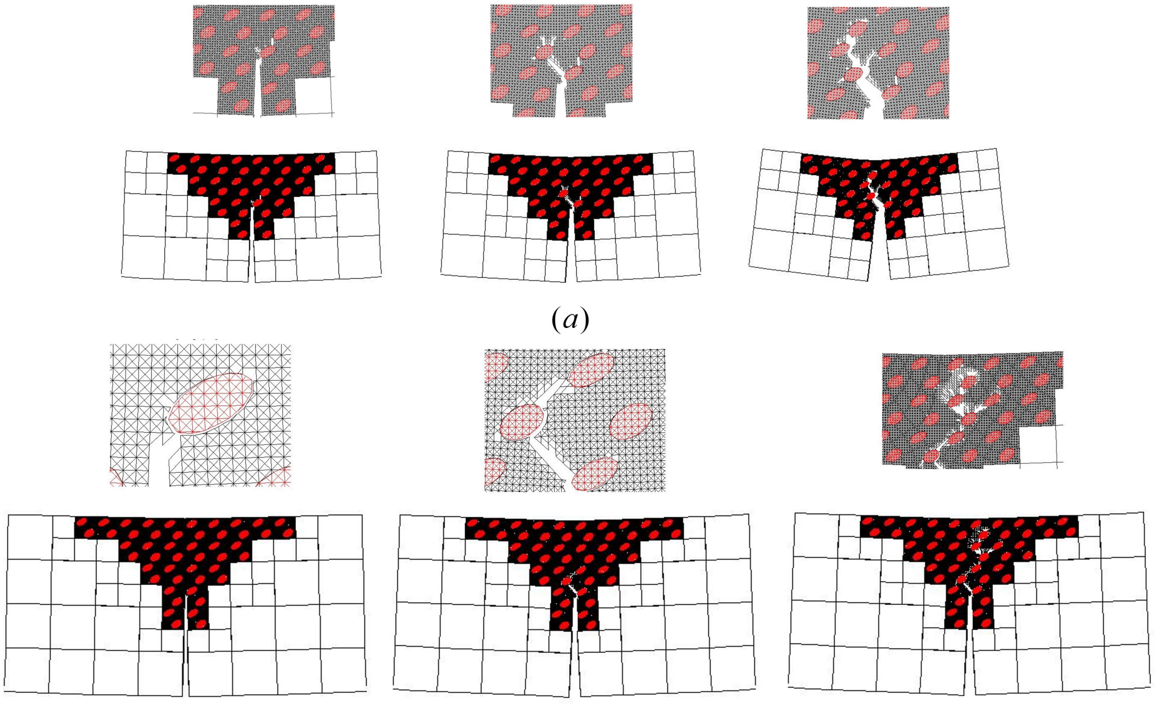
(*a*)

(*b*)

Figure 5.8: *The initiation and propagation of crack for two different size: (a)* $6\hat{L}\hat{L}$*, (b)* $8\hat{L}\hat{L}$*.*

5.4 Summary and concluding remarks

The main idea of this chapter was to propose a suitable numerical framework to model the fracture of material in order to study the well known size effect problem. The key challenge here is that the size effect problem is due to the presence of a characteristic length that is associated with the internal heterogeneities of the material which reside in a length scale that is very small compared to the physical domain size. Therefore, a suitable numerical method should be able to precisely model the microstructures of the material while maintaining the computational efficiency. To do so, we recapitulated the basic concepts of the ACM^2 and explained how the combination of these concepts provide a framework that aims at efficiently and accurately modeling the fracture process zone which is essential for capturing the size effect problem. Basically, this method relies on two main concepts, namely, the adaptive refinement and the domain coupling method. The adaptive refinement is responsible for accurate description of the material when the deformation field is highly heterogeneous. In fact, this concept proposes to refine the mesh to improve the numerical solution and when the mesh size becomes comparable to that of the unit cell this method proposes to replace the continuum elements with the unit cells. In this paper we also proposed a new method for adaptive refinement. In this method a failure envelope is derived based on the homogenized behavior of the material which is useful for precisely predicting the initiation of the damage at the microscopic scale. The adaptive refinement procedure was then modified such that when the size of a finite element becomes comparable to that of unit cell, ans the failure envelope on any sampling point (such as gauss points) becomes negative, the element should be replaced by a unit cell to precisely capture the damage nucleation that takes place on the microscopic length scale. As a consequence of applying this concept the computational domain is split into two domains with different resolution of material description, the macroscopic domain, which is based on the continuum description of the material and the microscopic domain that consists of unit cells which explicitly carry the information of the microscopic structure of the material. The second concept then deals with the coupling of these two different domains. This concept actually guarantees force and displacement equilibrium at the boundary between two domains. Among all coupling methods, the quasi-periodic coupling method is shown to be the most accurate and permits the existence of fluctuating field on the boundary between the macroscopic and microscopic domains which prevents emerging an artificial boundary in this region. In this paper we also discussed about the nonlinear finite element formulation as well as a nested incremental solution approach to accurately model the large deformation in front of a loaded crack.

In this paper we mainly focused on the fracture of a specific type of microscopically heterogeneous material, that is reminiscent of concrete-like composites, which is associated with a simple damage model that describes the failure of material on the microscopic length scale. The accuracy and the efficiency of the method was illustrated through the first example. Next, we modeled the fracture of similar structures with different sizes and showed the capability of the method to capture the associated resistance curve of the material for each case. We then showed how the method achieves to capture the size effect phenomena that naturally exists for concrete-like materials. It should also be noted that although the material in this paper is not real and the assumption that the material is periodic at microscopic scale is very simplistic, the generality of method to predict the fracture behavior of material is not questionable. Nevertheless, by further improvement such as extending the simplistic linear damage models to realistic nonlinear models or considering a weibul distribution of microstructural material properties, the method has the capacity to be used as an efficient tool to design and optimize the material microstructure to build structures with higher safety at lower cost.

Chapter 6

Summary, concluding remarks and suggestion for future works

In summary, this thesis presented a new class of numerical multiscale methodology to precisely model the fracture of materials based on their microstructure. In reality the fracture of material is a multiscale procedure that is triggered by the nucleation of damage at the lower length scale. Based on this fact formulating an efficient method to precisely model the this phenomenon has always been a challenging issue. On the one hand, fully microstructural description of material for a macroscopic problem is not computationally tractable. On the other hand, macroscopic models based on coarse-grained continuum description of material are not accurate enough when the deformation field is highly heterogeneous. Despite many improvements such as theory of cosserat, micromorphics and non-local formulation, these methods are not capable of modeling the materials local response when the deformation field is highly heterogeneous. This is due to the fact that these methods are based on the concept of separation of scales upon which the macroscopic behavior is obtained by averaging the microscopic response on a representative volume element. To overcome these obstacles concurrent multiscale methods, which rely on enabling coexistence of different descriptions of material at various length scales. To achieve high accuracy while maintaining low computational cost these methods propose to split the macroscopic problem into different domains with different resolution of solution in each domain. Bridging scale methods, for example, aim at defining the microscopic domain a priori, such that the fracture process zone is captured at the microscopic level, while other parts of structures are modeled on macroscopic length scale. VCFEM based concurrent multiscale method is another technique in which the microscopic domain, which is detected automatically, coexist with the macroscopic domain and a transition domain that provides proper coupling of macroscopic and microscopic domains. Our methods contribution is however, many folds that are described in the following.

In the second chapter, under the assumption of finite elasticity, the formulation of the method was developed for elasticity problem based on few concepts. The first concept is adaptive refinement that is responsible for detecting numerical and modeling errors and improving the solution by either refining the finite element mesh or replacing macroscopic description of material by its exact microscopic definition. Based on the definition of discretization error, at the macroscopic level the finite element solution lacks accuracy when the deformation field is highly heterogeneous. When this condition is met, such as in the vicinity of sharp corners or crack tips, the adaptive refinement then proposes to locally refine the finite element mesh to improve the accuracy of the numerical model. However, the mesh refinement at the macroscopic level induces another type of error, homogenization error. Based on homogenization theory, under certain circumstances, at the macroscopic level a continuum model is sufficient to describe a microstructurally heterogeneous material. The constitutive relation of such model is then derived by averaging out the response of the material microstructure over a certain domain, that is called unit cell. In fact, the homogenization error quantifies the lack of preciseness of continuum model. In order to ensure that this type of error does not exceed its maximum allowable value the size of continuum(macroscopic) elements should not be smaller than a certain size. The adaptive refinement, then proposes to replace the finite elements by explicit unit cells if their size, as result of refinement, become equal or smaller than the critical size. Consequently, the computational domain is split into two parts; 1) A macroscopic domain with continuum description of material. 2) A microscopic domain that is automatically captured and explicitly describes the material at the microscopic level. The challenge here was to formulate proper bridging methods between the macroscopic and microscopic domains which should satisfy the kinematic condition between the two domains. Next we proposed three different types of coupling methods that satisfy the above mentioned condition in different senses. The first coupling method, aims at strongly satisfying the kinematic condition. In other words, after deformation the microscopic nodes on the edge of microscopic domain, are bond to their neighbor points in the macroscopic domain before and after deformation. In contrary, to weakly satisfy the coupling condition, the second coupling condition is being formulated based on least-square averaging technique. After applying this coupling condition, the microscopic nodes on the edge between two domains, follow the deformation of adjacent macroscopic edge in average sense, that is they are freely fluctuate around the exact macroscopic deformation field along this edge. Finally we introduced the quasi-periodic boundary coupling method that combines the constrains that are introduced in second method and a set of extra constrains to enforce the periodic boundary condition. In this method after deformation the microscopic nodes follow the macroscopic deformation in average sense but the overall deformation field is periodic. Compared to the weak coupling method in this method the fluctuation fields are more constrained and the microscopic nodes smoothly fluctuate on the edge of microscopic domain. Although, all methods satisfy the required kinematic conditions, we illustrated that the quasi-periodic boundary coupling method reproduces the exact same results as if the entire domain was modeled at microscopic level. The ACM^2 then combines these concepts to assure exact numerical results while preserving the computational cost low.

In chapter three, in order to study fracture of microscopically heterogeneous material we take the advantage of XFEM and extended our multiscale formulation to obtain solution for elasticity problems that contain displacement discontinuity such as cracks. For this we reformulated our coupling condition, to account for preexisting cracks and discussed the details about implementing different coupling conditions and incremental loading procedure that is vital for modeling crack propagation. Although this chapter was limited to the small strains theory and linear elasticity assumptions, it lays ground for more complex problems that were introduced in next chapter.

To reconcile the concepts of damage mechanics to those of fracture mechanics, an efficient approach should be able to account for macroscopic loading while accurately modeling the fracture process zone in front of the crack. This includes modeling finite deformation field in front of the loaded crack tip as well as damage models that describe the failure of the material in the microscopic level. In chapter four, we introduced a nonlinear finite strain formulation of the method, in order to accurately model the large deformation and rotations that exist in front of a loaded crack. We also presented examples of heterogeneous materials whose matrix were described with lattice model and characterized by a simple damage model. In addition, the aforementioned incremental procedure was improved to accurately capture the damage propagation by incorporating a predictor-corrector algorithm. We illustrated that our method was capable of predicting the resistance curve associated with these materials. Indeed, the dual description of the material in this method provides a ground to describe the fracture in two forms: a) a detailed microstructured form, in the process zone where the deformation is highly heterogeneous and b) coarse grained continuum form, where the deformation field is homogeneous. Accuracy and efficiency of the method were also discussed in through several examples. We also illustrated how the adaptivity is critical for reducing computational cost in the case of evolving fracture. In addition, we investigated the effect of micro structural properties, void volume fraction in the case of porous heterogeneous material, on the fracture resistance curve of the material. We demonstrated that increasing the volume fraction of the voids results in the rise of associated R-curve and eventually delaying the unstable crack growth and rendering its matrix brittle material to microscopically ductile behavior. This chapter, clearly shows the most important application of the presented method that is to formulate a relation between the material microstructural properties on the macroscopic fracture behavior.

Due to the well known size effect problem, it is generally accepted that the behavior of a material in large scale might be different than its behavior in small scales, when the material is microscopically heterogeneous. Predicting the size effect problem and quantifying a relation between the properties of the materials microstructure on the size effect problem is not possible experimentally and should be carried out through numerical modeling and computer simulation. Among all theories the crack band theory has been successfully formulated to model and capture this effect based on continuum description of material. The key concept in this method is that the fracture process zone is a priori introduced to the model and the material in this region is modeled based on a softening constitutive model that represents its failure. In chapter four, we discussed about the mechanical aspect of the size effect problem and the underlying concepts of the crack band theory for concrete. We then described a heterogeneous concrete-like material that consists of three phases in the mesoscopic scale which is characterized by simplistic damage models to describe the failure of each phase. Through an example, we showed how the proposed method aims at predicting the size effect on the martial nominal strength. Although the material in this part was not realistic and the microscopic damage models were based on very simplistic assumptions, the generality of results and the efficiency of the method is not questionable. In this chapter we also improved the adaptive refinement procedure to accurately capture the fracture process zone. This method is based on introducing a failure envelope for material, that is derived by performing damage analysis on materials unit cell and indicates nucleation of the damage at microscopic scale. This method then proposes to replace the continuum description of the material by its exact microscopic description when the macroscopic stress state meets the criteria defined by material's failure envelope.

In general, this dissertation proposed a new class of multiscale method that is based on accurately modeling the process zone in front of the crack tip and concurrently describes the material at different length scales. The main contributions of this method, can be summarized as follows:

- An adaptive refinement concept that is responsible for automatic detection of the fracture process zone in front of preexisting crack or evolving localized damage.

- A macro micro coupling methods that ensure proper interaction of the different descriptions of material. These conditions allow fluctuation of the microscopic field on the edge of microscopic domain that is essential to circumvent the effect of artificial boundaries. Also these coupling conditions are such that any microscopic model, such as atomistic, continuum or lattice could be utilized in the model.
- The XFEM concept was invoked to model the fracture and the discontinuous displacement field along cracks in each domains.

Beside developing the formulation of the method, this dissertation also presented some examples that shows the method is a useful tool to investigate the relation between the microscopic features of materials and the overall macroscopic behavior. By further development the method can be used to investigate and optimize the microstructure to design material with high fracture resistance capacity. Some suggestions are as follows:

- Mesh coarsening algorithm that can revert the microscopic to macroscopic domain in the wake of crack. When crack propagation is modeled this feature will improve the computational efficiency of the method, since it proposes to have the microsopic domain just at the crack tip.
- Extension of the concept of periodic structure to that of random structures to mimic more realistic material.
- Random distribution of material properties at the microscopic level, in order to mimic a real material for which the fracture behavior is governed with random distribution of the weak links at the microscopic level, such as concrete. The general behavior of such material can then be derived based on monte carlo simulations and averaging out the results.

Bibliography

[1] M. Ainsworth and B. Senior. Aspects of an adaptive hp-finite element method: adaptive strategy, conforming approximation and efficient solvers. Computer Methods in Applied Mechanics and Engineering, 150:65–87, 1997.

[2] W. B. Anderson and R. S Lakes. Size effects due to cosserat elasticity and surface damage in closed-cell polymethacrylimide foam. Journal of Materials Science, 29:6413–6419, 1994.

[3] Z. P. Bazant and G. Pijaudier-Cabot. Nonlocal continuum damage, localization instability and convergence. ASME Journal of Applied Mechanics, 57:287–293, 1988.

[4] Z.P. Bazant and M. Jirasek. Nonlocal integral formulations of plasticity and damage: survey of progress. ASME Journal of Applied Mechanics, 128(11):1119–1149, 2002.

[5] Z.P. Bazant and J. Ozbolt. Nonlocal microplane model for fracture, damage and size effect in structures. ASME Journal of Applied Mechanics, 116(11):2484–2504, 1990.

[6] T. Belytschko and S.P. Xiao. Coupling methods for continuum model with molecular model. International Journal of Multiscale Engineering, 1(1):115–126, 2003.

[7] R. Borst, J. Pamin, R. H. J. Peerlings, and L. J. Sluys. On gradient-enhanced damage and plasticity models for failure in quasi-brittle and frictional materials. Computational Mechanics, 17(1):130–141, 1995.

[8] E. Cosserat and F. Cosserat. Theorie des corps deformables. Hermann, Paris, 1909.

[9] E. F. DAzevedo. Optimal triangular mesh generation by coordinate transformation. SIAM Journal on Scientific Computing, 12(4):755–786, 1991.

[10] R. de Borst. Simulation of strain localization: a reappraisal of the cosserat continuum. Engineering Computations, 8(4):317–332, 1991.

[11] W.J. Drugan and J.R. Willis. A micromechanics-based nonlocal constitutive equation and estimates of representative volume element size for elastic composites. Journal of the Mechanics and Physics of Solids, 44(4):497–524, 1996.

[12] N.A. Fleck and J.W. Hutchinson. A phenomenological theory for strain gradient effects in plasticity. Journal of the Mechanics and Physics of Solids, 41(12):1825–1857, 1993.

[13] N.A. Fleck, G.M. Muller, M.F. Ashby, and J.W. Hutchinson. Strain gradient plasticity: theory and experiment. Acta Metallurgica et Materialia, 42(2):475–487, 1994.

[14] S. Forest and K. Sab. Cosserat overall modeling of heterogeneous materials. Mechanics research communications, 25(4):449–454, 1998.

[15] T.P. Fries, A. Byfut, A. Alizada, K.W. Cheng, and A. Schröer. Hanging nodes and xfem. International Journal for Numerical Methods in Engineering, 86:404–430, 2011.

[16] S. Ghosh, J. Bai, and P. Raghavan. Concurrent multi-level model for damage evolution in microstructurally debonding composites. Mechanics of Material, 39:241–266, 2007.

[17] S. Ghosh, K. Lee, and S. Moorthy. Multiple scale analysis of heterogeneous elastic structures using homogenisation theory and voronoi cell finite element method. International Journal of Solids and Structures, 32(1):27–62, 1995.

[18] S. Ghosh, K. Lee, and S. Moorthy. Two scale analysis of heterogeneous elasticplastic materials with asymptotic homogenisation and voronoi cell finite element model. Computer Methods in Applied Mechanics and Engineering, 132:63–116, 1996.

[19] S. Ghosh, K. Lee, and P. Raghavan. A multi-level computational model for multi-scale damage analysis in composite and porous materials. International Journal of Solids and Structures, 38:2335–2385, 2001.

[20] P.R. Guduru, A.J. Rosakis, and G. Ravichandran. Dynamic shear bands: an investigation using high speed optical and infrared diagnostic. Mechanics of Material, 33:371–402, 2001.

[21] J.M. Guedes and N. Kikuchi. Preprocessing and postprocessing for materials based on the homogenization method with adaptive finite element methods. Computer Methods in Applied Mechanics and Engineering, 83(2):143–198, 1990.

[22] AK. Gupta. A finite element for transition from a fine grid to a coarse grid. International Journal for Numerical Methods in Engineering, 12:35–45, 1978.

[23] M. E. Gurtin and A. Needleman. Boundary conditions in small-deformation, single-crystal plasticity that account for the burgers vector. Journal of the Mechanics and Physics of Solids, 53(1):1, 2005.

[24] D. Guzman, M.S. Neubauer, G. Flinn, and Nix W.D. The role of indentation depth on the measured hardness of materials. Materials Research Symposium Proceedings, 308:613–618, 1993.

[25] R. Hill. Elastic properties of reinforced solids: some theoretical principles. Journal of the Mechanics and Physics of Solids, 11:357–372, 1963.

[26] Y. Huang, L. Zhang, T.F. Guo, and K.C. Hwang. Mixed mode near-tip fields for cracks in materials with strain-gradient effects. Journal of the Mechanics and Physics of Solids, 45:439–465, 1997.

[27] Vernerey F. J., McVeigh C., Liu W. K., Moran B., Tewari D., Parks D., and Olson G. The 3d computational modeling of shear dominated ductile failure of steel. JOM, The Journal of The Minerals, Metals and Materials Society, 2006.

[28] T. Kanit, S. Forest, I. Galliet, V. Mounoury, and D. Jeulin. Determination of the size of the representative volume element for random composites: statistical and numerical approach. International Journal of Solids and Structures, 40:3647–3679, 2003.

[29] V. Kouznetsova, W. A. M. Brekelmans, and FPT Baaijens. An approach to micromacro modelling of heterogeneous materials. Computational Mechanics, 27:37–48, 2001.

[30] V. Kouznetsova, M. G. D. Geers, and W. A. M. Brekelmans. Multi-scale constitutive modelling of heterogeneous materials with a gradient-enhanced computational homogenization scheme. International Journal for Numerical Methods in Engineering, 54:1235–1260, 2002.

[31] W.K. Liu, E.G. Karpov, S. Zhang, and H.S. Park. An introduction to computational nanomechanics and materials. Computer Methods in Applied Mechanics and Engineering, 193:1529–1578, 2004.

[32] Q. Ma and D.R. Clarke. Size dependent hardness in silver single crystals. Journal of Materials Research, 10:853–863, 1995.

[33] S. Mohammadi. Extended finite element method: for fracture analysis of structures. Blackwell Publishing Ltd,, Oxford, 2008.

[34] S. Moorthy and S. Ghosh. a model for analysis of arbitrary composite and porous microstructures with voronoi cell finite elements. ijnme, 39:2363–2398, 1996.

[35] J.W. Hutchinson M.R. Begley.1. The mechanics of size-dependent indentation. Journal of the Mechanics and Physics of Solids, 4(10):2049–2068, 1998.

[36] S. Nemat-Nasser and M. Hori. Micromechanics: overall properties of heterogeneous materials. Elsevier, Amsterdam, 1993.

[37] H.S. Park and W.K. Liu. An introduction and tutorial on multiple-scale analysis in solids. Computer Methods in Applied Mechanics and Engineering, 193:201–217, 2004.

[38] P. Raghavan and S. Ghosh. Adaptive multi-scale computational modeling of composite materials. Science, 5(2):151–170, 2004.

[39] P. Raghavan and S. Ghosh. Concurrent multi-scale analysis of elastic composites by a multi-level computational model. Mechanics of Material, 193:497–538, 2007.

[40] Sh.I. Ranganathan and M. Ostoja-Starzewski. Scaling function, anisotropy and the size of rve in elastic random polycrystals. Journal of the Mechanics and Physics of Solids, 53:2773–2791, 2008.

[41] K. Subbaraj and M.A. Dokainish. Side-node transition quadrilateral finite elements for mesh-grading. Computers & Structures, 30(5):117–118, 1988.

[42] P.M. Suquet. Local and global aspects in the mathematical theory of plasticity. Elsevier Applied Science Publishers, London., 1985.

[43] F. J. Vernerey and M. Farsad. An eulerian/xfem formulation for the large deformation of cortical cell membrane. Computer Methods in Biomechanics and Biomedical Engineering, 14(5):433–445, 2011.

[44] F. J. Vernerey, W. K. Liu, and B. Moran. Multi-scale micromorphic theory for hierarchical materials. Journal of the Mechanics and Physics of Solids, 55(12):2603–2651, 2007.

[45] F. J. Vernerey, W. K. Liu, B. Moran, and G. B. Olson. A micromorphic model for the multiple scale failure of heterogeneous materials. Journal of the Mechanics and Physics of Solids, 56(4):1320–1347, 2008.

[46] F. J. Vernerey, W. K. Liu, B. Moran, and G. B. Olson. Multi-length scale micromorphic process zone model. Computational Mechanics, 44:433–445, 2009.

[47] F.J. Vernerey and F. Barthelat. On the mechanics of fish-scale structures. International Journal of Solids and Structures, 47(17):2268–2275, 2010.

[48] F.J. Vernerey and M. Farsad. A constrained mixture approach to mechano-sensing and force generation in contractile cell. Journal of the Mechanical Behavior of Biomedical Materials, accepted for publication.

[49] F.J. Vernerey, L. Foucard, and M. Farsad. Bridging the scales to explore cellular adaptation and remodeling. BionanoScience, accepted for publication.

[50] G.J. Wagner and W.K. Liu. Coupling of atomistic and continuum simulations using a bridging scale decomposition. Computational Materials Science, 190:249–274, 2003.

[51] A.A. Yazdani, A.Gakwaya, and G. Dhatt. A posteriori error estimator based on the second derivative of the displacement field for two-dimensional elastic problems. Computers & Structures, 62(2):317–338, 1997.

[52] A.M. Gokhale Z. Shan. Representative volume element for non-uniform micro-structure. Computational Materials Science, 24:361–379, 2002.

[53] D. Zhu, C. Ortega, R. Motamedi, L. Szewciw, F.J. Vernerey, and F. Barthelat. Structure and mechanical performance of a modern fish scale, advanced biomaterials. Advances Biomaterials, accepted for publication.

[54] T.I. Zohdi, J.T. Oden, and G.J. Rodin. Hieratchical modeling of heterogeneous bodies. Computer Methods in Applied Mechanics and Engineering, 138:273–298, 1996.

[55] N. Moës J. Dolbow T. Belytschko. A finite element method for crack growth without remeshing. International Journal for Numerical Methods in Engineering, 46:131150, 1999.

[56] T. Belytschko and S.P. Xiao. Coupling methods for continuum model with molecular model. International Journal of Multiscale Engineering, 1(1):115–126, 2003.

[57] E. Cosserat and F. Cosserat. Theorie des corps deformables. Hermann, Paris, 1909.

[58] E. F. DAzevedo. Optimal triangular mesh generation by coordinate transformation. SIAM Journal on Scientific Computing, 12(4):755–786, 1991.

[59] R. de Borst. Simulation of strain localization: a reappraisal of the cosserat continuum. Engineering Computations, 8(4):317–332, 1991.

[60] R. de Borst. On gradient-enhanced coupled plastic damage theories. COMPUTATIONAL MECHANICS New Trends and Applications, 1998.

[61] M. Farsad, F. J. Vernerey, and H. S. Park. An extended finite element/level set method to study surface effects on the mechanical behavior and properties of nanomaterials. International Journal for Numerical Methods in Engineering, 84(12):1466–1489, 2010.

[62] N.A. Fleck and J.W. Hutchinson. A phenomenological theory for strain gradient effects in plasticity. Journal of the Mechanics and Physics of Solids, 41(12):1825–1857, 1993.

[63] N.A. Fleck, G.M. Muller, M.F. Ashby, and J.W. Hutchinson. Strain gradient plasticity: theory and experiment. Acta Metallurgica et Materialia, 42(2):475–487, 1994.

[64] S. Forest and K. Sab. Cosserat overall modeling of heterogeneous materials. Mechanics research communications, 25(4):449–454, 1998.

[65] T.P. Fries, A. Byfut, A. Alizada1, K.W. Cheng, and A. Schröer. Hanging nodes and xfem. International Journal for Numerical Methods in Engineering, 86:404–430, 2011.

[66] S. Ghosh, J. Bai, and P. Raghavan. Concurrent multi-level model for damage evolution in microstructurally debonding composites. Mechanics of Material, 39:241–266, 2007.

[67] S. Ghosh, K. Lee, and S. Moorthy. Multiple scale analysis of heterogeneous elastic structures using homogenisation theory and voronoi cell finite element method. International Journal of Solids and Structures, 32(1):27–62, 1995.

[68] S. Ghosh, K. Lee, and S. Moorthy. Two scale analysis of heterogeneous elasticplastic materials with asymptotic homogenisation and voronoi cell finite element model. Computer Methods in Applied Mechanics and Engineering, 132:63–116, 1996.

[69] S. Ghosh, K. Lee, and P. Raghavan. A multi-level computational model for multi-scale damage analysis in composite and porous materials. International Journal of Solids and Structures, 38:2335–2385, 2001.

[70] J.M. Guedes and N. Kikuchi. Preprocessing and postprocessing for materials based on the homogenization method with adaptive finite element methods. Computer Methods in Applied Mechanics and Engineering, 83(2):143–198, 1990.

[71] A. L. Gurson. Continuum theory of ductile rupture by void nucleation and growth: Part iyield criteria and flow rules for porous ductile media. Journal of Engineering Materials and Technology, 97(1,2):2–15, 1977.

[72] R. Hill. Elastic properties of reinforced solids: some theoretical principles. Journal of the Mechanics and Physics of Solids, 11:357–372, 1963.

[73] B. Hiriyur, H. Waisman, and G. Deodatis. Uncertainty quantication in homogenization of heterogeneous microstructures modeled by xfem. International Journal for Numerical Methods in Engineering, 88:257–278, 2011.

[74] Vernerey F. J. and Kabiri M. An adaptive concurrent multiscale method for microstructured elastic solids, "accepted for publication". Computer Methods in Applied Mechanics and Engineering, 2012.

[75] H. Kadowaki and W.K. Liu. Bridging multi-scale method for localization problems. CMAME, 193:3267–3302, 2004.

[76] V. Kouznetsova, WAM Brekelmans, and FPT Baaijens. An approach to micromacro modelling of heterogeneous materials. 27:37–48, 2001.

[77] W.K. Liu, E.G. Karpov, S. Zhang, and H.S. Park. An introduction to computational nanomechanics and materials. Computer Methods in Applied Mechanics and Engineering, 193:1529–1578, 2004.

[78] N. Moës M. Stolarska, D.L. Chopp and T. Belytschko. Modelling crack growth by level sets in the extended finite element method. International Journal for Numerical Methods in Engineering, 51:943–960, 2001.

[79] S. Moorthy and S. Ghosh. a model for analysis of arbitrary composite and porous microstructures with voronoi cell finite elements. International Journal for Numerical Methods in Engineering, 39:2363–2398, 1996.

[80] A. Needleman and V. Tvergaard. An analysis of ductile rupture in notched bars. Journal of the Mechanics and Physics of Solids, 32(6):461–490, 1984.

[81] S. Nemat-Nasser and M. Hori. Micromechanics: overall properties of heterogeneous materials. Elsevier, Amsterdam, 1993.

[82] H.S. Park, E.G. Karpov, W.K. Liu, and P.A. Klein. The bridging scale for two dimensional atomistic/continuum coupling. Philosophical Magazine, 85(1):79–113, 2005.

[83] H.S. Park and W.K. Liu. An introduction and tutorial on multiple-scale analysis in solids. Computer Methods in Applied Mechanics and Engineering, 193:201–217, 2004.

[84] P. Raghavan and S. Ghosh. Adaptive multi-scale computational modeling of composite materials. sci, 5(2):151–170, 2004.

[85] P. Raghavan and S. Ghosh. Concurrent multi-scale analysis of elastic composites by a multi-level computational model. mm, 193:497–538, 2007.

[86] J.R. Rice and D. M. Tracey. On the ductile enlargement of voids in triaxial stress fields. Journal of the Mechanics and Physics of Solids, 17:1733–1772, 1969.

[87] P.M. Suquet. Local and global aspects in the mathematical theory of plasticity. Elsevier Applied Science Publishers, London., 1985.

[88] F. J. Vernerey. A microstructure-based continuum model for multiphase solids "accepted for publication". Mechanics of Advanced Materials and Structures.

[89] F. J. Vernerey and T. Chevalier. A multiscale micro-continuum model to capture strain localization in composite materials "accepted for publication". International Journal of Multiscale Engineering, 2006.

[90] F. J. Vernerey, W. K. Liu, and B. Moran. Multi-scale micromorphic theory for hierarchical materials. Journal of the Mechanics and Physics of Solids, 55(12):2603–2651, 2007.

[91] F. J. Vernerey, W. K. Liu, B. Moran, and G. B. Olson. A micromorphic model for the multiple scale failure of heterogeneous materials. Journal of the Mechanics and Physics of Solids, 56(4):1320–1347, 2008.

[92] F. J. Vernerey, W. K. Liu, B. Moran, and G. B. Olson. Multi-length scale micromorphic process zone model. 44:433–445, 2009.

[93] F.J. Vernerey. The effective permeability of cracks and interfaces in porous media "accepted for publication". Transport in Porous Media, 2006.

[94] F.J. Vernerey. A theoretical treatment on the mechanics of interfaces in deformable porous media. International Journal of Solids and Structures, 48(22,23):3129–3141, 2011.

[95] G.J. Wagner and W.K. Liu. Coupling of atomistic and continuum simulations using a bridging scale decomposition. Computational Materials Science, 190:249–274, 2003.

[96] A.A. Yazdani, A.Gakwaya, and G. Dhatt. A posteriori error estimator based on the second derivative of the displacement field for two-dimensional elastic problems. Computers & Structures, 62(2):317–338, 1997.

[97] T.I. Zohdi, J.T. Oden, and G.J. Rodin. Hieratchical modeling of heterogeneous bodies. Computer Methods in Applied Mechanics and Engineering, 138:273–298, 1996.

[98] N. A. Fleck B. Budiansky and J. C. Amazigo. On kink-band propagation in fiber composites. J. Mech. Phys. Solids, 46(9):1637:1635, 1997.

[99] G. I. Barenblatt. The mathematical theory of equilibrium cracks in brittle fracture. Advanced Appl. Mech, 7:55:129, 1962.

[100] G. I. Barenblatt. Similarity, self-similarity and intermediate asymptotics. Consultants Bureau, New York, 1979.

[101] Z. P. Bažant. Instability, ductility, and size effect in strain-softening concrete. J. Eng. Mech. Div., Am. Soc. Civil Engrs., 103:357:358, 1976.

[102] Z. P. Bažant. Size effect in blunt fracture: Concrete, rock, metal. J. Eng. Mech. ASCE, 110:518:535, 1984.

[103] Z. P. Bažant. Large-scale thermal bending fracture of sea ice plates. J. Geophys. Res., 97:739:751, 1992.

[104] Z. P. Bažant. Size effect on structural strength: a review. Archive of Applied Mechanics, 69:703:725, Springer-Verlag 1999.

[105] F. M. Beremin. A local criterion for cleavage fracture of a nuclear pressure vessel steel. Metallurgy Transactions A, 1983.

[106] D. S. Dugdale. Yielding of steel sheets containing slits. J. Mech. Phys. Solids, 8(49):100:108, 1960.

[107] A. G. Evans. A general approach for the statistical analysis of multiaxial fracture. J. of the American Ceramic Soc., 61:302:308, 1978.

[108] A. A. Griffith. he phenomena of rupture and flow in solids. Phil. Trans., 1921.

[109] D. Gross and T. Seelig. Fracture mechanics: with an introduction to micromechanics. Springer, 2011.

[110] Z. P. Bažant; M. Jirásek. R-curve modeling of rate and size effects in quasibrittle fracture. International Journal of Fracture, 62:355:373, 1993.

[111] F.J. Vernerey; M. Kabiri. An adaptive concurrent multiscale method for microstructured elastic solids, “accepted for publication”. Computer Methods in Applied Mechanics and Engineering, 2012.

[112] Z. P. Bažant; M. T. Kazemi. Size effect on diagonal shear failure of beams without stirrups. ACI Structural Journal, 88(3):268:276, 1991.

[113] Z.P. Bažant; M. T. Kazemi. Size effect in fracture of ceramics and its use to determine fracture energy and effective process zone length. J. American Ceramic Society, 73(7):1841:1853, 1990.

[114] R. H. Leicester. The size effect of notches. Proc., 2nd Australasian Conf. Mech. Struct. Mater., 1969 Melbourne.

[115] Z. P. Bažant; I. M. Daniel; Z. Li. Size effect and fracture characteristics of composite laminates. ASME J. Eng. Mat. Tech., 118(3):317:324, 1996.

[116] M. Ostoja-Starzewski. Lattice models in micromechanics. Applied Mechanics Reviews, 55(1):35–60, 2002.

[117] A. Hillerborg; M. ModeÂer; P. E. Petersson. Analysis of crack formation and crack growth in concrete by means of fracture mechanics and finite elements. Cement and Concrete Research, 6:773:782, 1976.

[118] E. Schlangen and J. G. M. Mier. Simple lattice model for numerical simulation of fracture of concrete materials and structures. Materials and Structures, 25(9):534–542, November 1992.

[119] M. Kabiri; F.J. Vernerey. Adaptive concurrent multiscale model for fracture and crack propagation in heterogeneous media, "submitted". Computer Methods in Applied Mechanics and Engineering, 2013.

[120] M. Kabiri; F.J. Vernerey. An xfem based multiscale approach to fracture of heterogeneous media, "in press". International Journal of Multiscale Computational Engineering, 2013.

[121] P. F. Walsh. Fracture of plain concrete. Indian Concrete J., 46(11):4.1::4.20, 1972.

[122] P. F. Walsh. Crack initiation in plain concrete. Magazine of Concrete Research, 28:37:41, 1976.

[123] W. Weibull. The phenomenon of rupture in solids. Proc. Royal Swedish Inst. Eng. Res., 1939.

[124] W. Weibull. A statistical representation of fatigue failures in solids. Proc. Roy. Inst. Techn., 1949.

[125] W. Weibull. A statistical distribution function of wide applicability. J. Appl. Mech. ASME, 1951.

[126] W. Weibull. Basic aspects of fatigue. Proc. Colloquium on Fatigue., Springer-Verlag: Stockholm 1956.

[127] K.A. Atkinson. An Introduction to Numerical Analysis (2nd ed.). John Wiley & Sons, New York, 1989.

[128] Z.P. Bazant. Determination of fracture energy, process zone length and brittleness number from size effect, with application to rock and concrete. International Journal of Fracture, 44:111–131, 1990.

[129] N. Moës J. Dolbow T. Belytschko. A finite element method for crack growth without remeshing. International Journal for Numerical Methods in Engineering, 46:131150, 1999.

[130] T. Belytschko, W.K. Liu, and B. Moran. Nonlinear finite elements for continua and structures. Wiley and Sons, 2000.

[131] T. Belytschko and J. H. Song. Coarse-graining of multiscale crack propagation. International Journal for Numerical Methods in Engineering, 81:537–563, 2010.

[132] T. Belytschko and S.P. Xiao. Coupling methods for continuum model with molecular model. International Journal of Multiscale Computational Engineering, 1(1):115–126, 2003.

[133] B. Budiansky, J. C. Amazigo, and A. G. Evans. Small scale crack bridging and the fracture toughness of particulate-reinforced. J. Mech. Physc. Solids, 36(2):167–187, 1988.

[134] M. A. Guti errez C. V. Verhoosel, J. J. C. Remmers and R. de Borst. Computational homogenisation for adhesive and cohesive failure in quasi-brittle solids. International Journal for Numerical Methods in Engineering, 83:1155–1179, 2010.

[135] E. Cosserat and F. Cosserat. Theorie des corps deformables. Hermann, Paris, 1909.

[136] B. N. COX. Extrinsic factors in the mechanics of ridged cracks. Acta metall. mater., 39(6):1189–1201, 1991.

[137] B N Cox and D B Marshall. The determination of crack bridging forces. International Journal of Fracture, 49:159–176, 1991.

[138] E. F. DAzevedo. Optimal triangular mesh generation by coordinate transformation. SIAM Journal on Scientific Computing, 12(4):755–786, 1991.

[139] R. de Borst. Simulation of strain localization: a reappraisal of the cosserat continuum. Engineering Computations, 8(4):317–332, 1991.

[140] R. de Borst. On gradient-enhanced coupled plastic damage theories. Computer Methods in Applied Mechanics and Engineering, 1998.

[141] P.D. Zavattieri C.M. Li F. Barthelat, H. Tang and H.D. Espinosa. On the mechanics of mother-of-pearl: a key feature in the material hierarchical structure. Journal of the Mechanics and Physics of Solids, 55(2):225–444, 2007.

[142] M. Farsad, F.J. Vernerey, and H. S. Park. An extended finite element/level set method to study surface effects on the mechanical behavior and properties of nanomaterials. International Journal for Numerical Methods in Engineering, 84(12):1466–1489, 2010.

[143] J. Fish and V. Belsky. Multi-grid method for periodic heterogeneous media part 2: Multiscale modeling and quality control in multidimensional case. Computer Methods in Applied Mechanics and Engineering, 126, 1995.

[144] Vernerey F.J., McVeigh C., Liu W. K., Moran B., Tewari D., Parks D., and Olson G. The 3d computational modeling of shear dominated ductile failure of steel. The Journal of The Minerals, Metals and Materials Society, 2006.

[145] N. A. Fleck and J. W. Hutchinson. Strain gradient plasticity. Advances in Applied Mechanics, 33:295–361, 1997.

[146] N.A. Fleck and J.W. Hutchinson. A phenomenological theory for strain gradient effects in plasticity. Journal of the Mechanics and Physics of Solids, 41(12):1825–1857, 1993.

[147] N.A. Fleck, G.M. Muller, M.F. Ashby, and J.W. Hutchinson. Strain gradient plasticity: theory and experiment. Acta Metallurgica et Materialia, 42(2):475–487, 1994.

[148] S. Forest and K. Sab. Cosserat overall modeling of heterogeneous materials. Mechanics research communications, 25(4):449–454, 1998.

[149] S. Ghosh, J. Bai, and P. Raghavan. Concurrent multi-level model for damage evolution in microstructurally debonding composites. Mechanics of Material, 39:241–266, 2007.

[150] S. Ghosh, K. Lee, and P. Raghavan. A multi-level computational model for multi-scale damage analysis in composite and porous materials. International Journal of Solids and Structures, 38:2335–2385, 2001.

[151] S. Ghosh H. Bhatnagar and M.E. Walter. A parametric study of damage initiation and propagation in eb-pvd thermal barrier coatings. Mechanics of Materials, 42(1):96–107, 2010.

[152] M. Kabiri and F.J. Vernerey. An xfem based multiscale approach to fracture of heterogeneous media, “in press”. International Journal of Multiscale Computational Engineering, 2013.

[153] M. Kachanov, E.L.E. Montagut, and J.P. Laures. Mechanics of crackmicrocrack interactions. Mechanics of Materials, 10(1-2):59–71, November 1990.

[154] H. Kadowaki and W.K. Liu. Bridging multi-scale method for localization problems. Computer Methods in Applied Mechanics and Engineering, 193:3267–3302, 2004.

[155] V. Kouznetsova, W. A. M. Brekelmans, and F. P. T. Baaijens. An approach to micro-macro modelling of heterogeneous materials. 27:37–48, 2001.

[156] W.K. Liu, E.G. Karpov, S. Zhang, and H.S. Park. An introduction to computational nanomechanics and materials. Computer Methods in Applied Mechanics and Engineering, 193:1529–1578, 2004.

[157] X Liu, J Luo, and J Zhu. Size effect on the crystal structure of silver nanowires. Nano Letters, 6(3):408–412, 2006.

[158] M.A. Meyers, A.Y.M. Lin, Y. Seki, P.Y. Chen, B.K. Kad, and S. Bodde. biological composites: an overview. The Journal of The Minerals, Metals and Materials Society, 58(7):35, 2006.

[159] S. Mohammadi. Extended Finite Element Method. Blackwell, 2008.

[160] S. Moorthy and S. Ghosh. a model for analysis of arbitrary composite and porous microstructures with voronoi cell finite elements. International Journal for Numerical Methods in Engineering, 39:2363–2398, 1996.

[161] S. E. Mousavi and N. Sukumar. Generalized gaussian quadrature rules for discontinuities and crack singularities in the extended finite element method. Computer Methods in Applied Mechanics and Engineering, (49-52):3237–3249, 199.

[162] S. Nemat-Nasser and M. Hori. Micromechanics: overall properties of heterogeneous materials. Elsevier, Amsterdam, 1993.

[163] M. Ostoja-Starzewski. Lattice models in micromechanics. Applied Mechanics Reviews, 55(1):35–60, 2002.

[164] T. Pardoen and J.W. Hutchinson. Micromechanics-based model for trends in toughness of ductile metals. Acta Materialia, 51:133–148, 2003.

[165] H.S. Park, E.G. Karpov, W.K. Liu, and P.A. Klein. The bridging scale for two dimensional atomistic/continuum coupling. Philosophical Magazine, 85(1):79–113, 2005.

[166] H.S. Park and W.K. Liu. An introduction and tutorial on multiple-scale analysis in solids. Computer Methods in Applied Mechanics and Engineering, 193:201–217, 2004.

[167] A.E. Huespea P.J. Sncheza, P.J. Blancoc and R.A. Feijoc. Failure-oriented multi-scale variational formulation: Micro-structures with nucleation and evolution of softening bands. Computer Methods in Applied Mechanics and Engineering, 257:221–247, 2013.

[168] P. Raghavan and S. Ghosh. Adaptive multi-scale computational modeling of composite materials. sci, 5(2):151–170, 2004.

[169] P. Raghavan and S. Ghosh. Concurrent multi-scale analysis of elastic composites by a multi-level computational model. mm, 193:497–538, 2007.

[170] J. R. Rice and D. M. Tracey. On the ductile enlargement stress of voids in triaxial. J. Mech. Physc. Solids, 17:201–217, 1969.

[171] E. Schlangen and J. G. M. Mier. Simple lattice model for numerical simulation of fracture of concrete materials and structures. Materials and Structures, 25(9):534–542, November 1992.

[172] D. Sen and M.J. Buehler. Atomistically-informed mesoscale model of deformation and failure of bioinspired hierarchical silica nanocomposites. International Journal of Applied Mechanics, 02(04):699–717, 2010.

[173] W.K. Wilson S.K. Chan, I.S. Tuba. on the finite element method in linear fracture mechanics. Engineering Fracture Mechanics, 2:1–17, 1970.

[174] F. V. Souza and D. H. Allen. Modeling the transition of micro cracks into macro cracks in heterogeneous viscoelastic media using a two-way coupled multi scale model. International Journal of Solids and Structures, 48:3160–3175, 2011.

[175] V. Tvegard. material failure by void coalescence inlocalized shear bands. Int. J. Solids Structures, 18(8):5690672, 1982.

[176] V. Tvegard. Numerical study of localization in a void-sheet. Int. J. Solids Structures, 25(10):1143–1156, 1988.

[177] V. Tvegard and A. Needleman. An analysis of the brittlc ductile transition in dynamic crack growth. International Journal of Fracture, 59:53–67, 1993.

[178] Viggo Tvergaard. Influence of void nucleation on ductile shear fracture at a free surface. J. Mech. Physc. Solids, 34(6):399–425, 1982.

[179] Viggo Tvergaard. Effect of ductile particle debonding during crack bridging in ceramics. Int. J. Mech. Sci, 34(8):635–649, 1992.

[180] M. Stroeven V. P. Nguyen, O. Lloberas-Valls and L. J. Sluys. Homogenization-based multiscale crack modelling: From micro-diffusive damage to macro-cracks. Computer Methods in Applied Mechanics and Engineering, 200:1220–1236, 2011.

[181] F.J. Vernerey. A microstructure-based continuum model for multiphase solids "accepted for publication". Mechanics of Advanced Materials and Structures.

[182] F.J. Vernerey. The effective permeability of cracks and interfaces in porous media "accepted for publication". Transport in Porous Media, 2006.

[183] F.J. Vernerey. A theoretical treatment on the mechanics of interfaces in deformable porous media. International Journal of Solids and Structures, 48(22,23):3129–3141, 2011.

[184] F.J. Vernerey and T. Chevalier. A multiscale micro-continuum model to capture strain localization in composite materials "accepted for publication". International Journal of Multiscale Computational Engineering, 2006.

[185] F.J. Vernerey and M. Kabiri. An adaptive concurrent multiscale method for microstructured elastic solids, "accepted for publication". Computer Methods in Applied Mechanics and Engineering, 2012.

[186] F.J. Vernerey, W. K. Liu, and B. Moran. Multi-scale micromorphic theory for hierarchical materials. Journal of the Mechanics and Physics of Solids, 55(12):2603–2651, 2007.

[187] F.J. Vernerey, W. K. Liu, B. Moran, and G. B. Olson. A micromorphic model for the multiple scale failure of heterogeneous materials. Journal of the Mechanics and Physics of Solids, 56(4):1320–1347, 2008.

[188] F.J. Vernerey, W. K. Liu, B. Moran, and G. B. Olson. Multi-length scale micromorphic process zone model. 44:433–445, 2009.

[189] G.J. Wagner and W.K. Liu. Coupling of atomistic and continuum simulations using a bridging scale decomposition. Computational Materials Science, 190:249–274, 2003.

Appendix A

Element subdivision and shape functions

As depicted in Fig. 6, local mesh refinement causes the appearance of *so-called "irregular nodes"* (or *"hanging nodes"*) [65] on the boundaries between refined and unrefined domains. Subsequently, unrefined elements, which hold these types of nodes, are known as *"irregular elements"*. Two different approaches have been introduced in literature [65] in order to deal with this kind of irregularity:

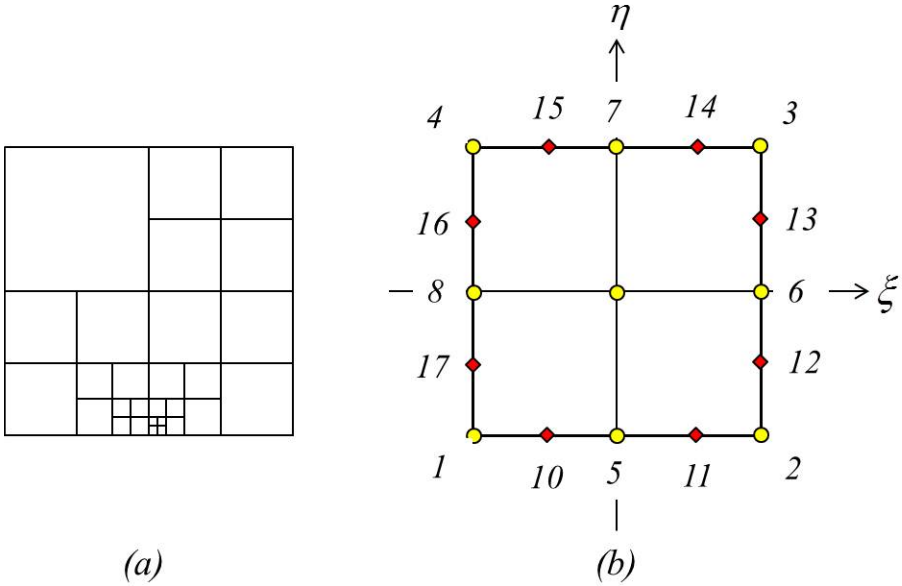

Figure A.1: *(a) 1-irregular mesh, (b) possible hanging nodes positions in an irregular element*

1) *Constrained approximation*: In this method [1], no degrees of freedom are associated with *hanging nodes* and the stiffness matrix is assembled using the standard shape functions. However, since standard shape functions do not satisfy conformity of displacement on the element's boundaries, it is assumed that the displacement of such nodes is the average of two adjacent regular nodes. Therefore, a pair of constraints are applied on each *hanging node* to enforce that their displacement remains in between adjacent regular nodes. These constraints can be applied by means of the *Lagrange-Multipliers* method or by multiplying the global stiffness matrix by a *so-called* connectivity matrix.

2) *Conforming shape functions*: This method [22] consists of assembling the global stiffness matrix by introducing new shape functions, which satisfy both partition of unity and conformity of displacement on the edges of *irregular elements*.

Since in our method, the macro-micro bridging is accomplished by constraining micro nodes to macro nodes, for the ease of implementation, we adopted the second approach. We also restricted ourself to *1-irregular* mesh (the definition for which can be found in [65]). As shown in Fig. 15b, for the case of *1-irregular* mesh, the method permits the incorporation of two additional *hanging nodes* on each edge of 9-node quadrilateral *irregular element*. Sbaraj and Dokainsh [41] presented an approach to formulate new shape functions for transition quadrilateral finite element for mesh grading. Following a similar approach, we introduced new sets of shape functions for 9-node quadrilateral elements. In what follows, shape functions are defined on quadrilateral 9-node parent element defined be Ω^* (Fig. 15). In order to satisfy the conformity of displacement, shape functions associated with all possible hanging nodes, (Fig. 15b), for all $\xi, \eta \in \Omega^*$, can be written as:

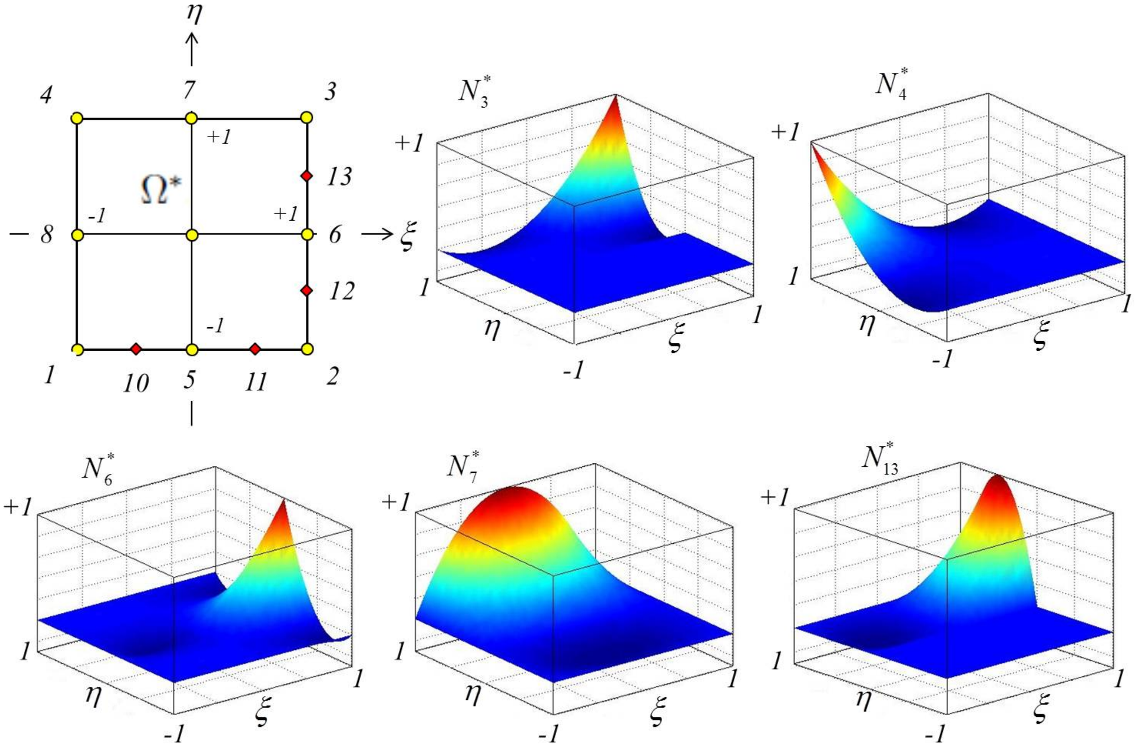

Figure A.2: *An irregular element with four hanging nodes on two edges and associated shape functions.*

$$
\begin{aligned}
N_{10}^* &= (-4\xi(1+\xi).H(-\xi)).(-0.5\eta(1-\eta))\\
N_{11}^* &= (+4\xi(1-\xi).H(+\xi)).(-0.5\eta(1-\eta))\\
N_{12}^* &= (+0.5\xi(1+\xi)).(-4\eta(1+\eta).H(-\eta))\\
N_{13}^* &= (+0.5\xi(1+\xi)).(+4\eta(1-\eta).H(+\eta))\\
N_{14}^* &= (+4\xi(1-\xi).H(+\xi)).(+0.5\eta(1+\eta))\\
N_{15}^* &= (-4\xi(1+\xi).H(-\xi)).(+0.5\eta(1+\eta))\\
N_{16}^* &= (-0.5\xi(1-\xi)).(+4\eta(1-\eta).H(+\eta))\\
N_{17}^* &= (-0.5\xi(1-\xi)).(-4\eta(1+\eta).H(-\eta)).
\end{aligned}
\tag{A.1}
$$

In this definition H is heaviside function defined by:

$$H(\chi) = \begin{cases} +1 \quad for \quad \chi > 0 \\ 0 \quad for \quad \chi < 0 \end{cases} \tag{A.2}$$

Once an *irregular node* i ($i = 10, 11, .., 17$) (Fig. 15b) exists, it takes the value N_i^* in (A.1), otherwise, it vanishes for all $\xi, \eta \in \Omega^*$. In addition, the standard quadratic shape functions, N_i ($i = 1, 2, ..., 9$), are modified as:

$$\begin{gathered} N_1^* = N_1 - 0.375(N_{10}^* + N_{17}^*) + 0.125(N_{11}^* + N_{16}^*) \\ N_2^* = N_2 - 0.375(N_{11}^* + N_{12}^*) + 0.125(N_{10}^* + N_{13}^*) \\ N_3^* = N_3 - 0.375(N_{13}^* + N_{14}^*) + 0.125(N_{12}^* + N_{15}^*) \\ N_4^* = N_4 - 0.375(N_{15}^* + N_{16}^*) + 0.125(N_{14}^* + N_{17}^*) \\ N_5^* = N_5 - 0.75(N_{10}^* + N_{11}^*) \\ N_6^* = N_6 - 0.75(N_{12}^* + N_{13}^*) \\ N_7^* = N_7 - 0.75(N_{14}^* + N_{15}^*) \\ N_8^* = N_8 - 0.75(N_{16}^* + N_{17}^*) \\ N_9^* = N_9 \end{gathered} \tag{A.3}$$

This method satisfies both the partition of unity and conformity of displacement between adjacent elements. Fig. 16 shows an *irregular element* with four *hanging nodes*, and some of its shape functions.

Appendix B

Total Lagrangian formulation

In this appendix, we provide details on the material and geometrical stiffness matrices in the Total-Lagrangian framework presented in section 4.4.1. We expressed the internal force vectors as:

$$\mathbf{f}^{int} = \int_{\Omega_0} \mathbf{B}_0^T \{\mathbf{S}\} d\Omega_0 \quad \Omega_0 \in \Omega, \tag{B.1}$$

in which the superscripts $\tilde{}$ and $\bar{}$ are dropped for simplicity. The matrix $\mathbf{B}_0$ in this formula is equal to:

$$\mathbf{B}_0 = \begin{bmatrix} \mathbf{B}_0^1 & \mathbf{B}_0^2 & ... & \mathbf{B}_0^{nne} \end{bmatrix} \tag{B.2}$$

where

$$\mathbf{B}_0^I = \begin{bmatrix} \frac{\partial N^I}{\partial x} F_{11} & \frac{\partial N^I}{\partial x} F_{21} \\ \frac{\partial N^I}{\partial y} F_{12} & \frac{\partial N^I}{\partial y} F_{22} \\ \frac{\partial N^I}{\partial x} F_{12} + \frac{\partial N^I}{\partial y} F_{11} & \frac{\partial N^I}{\partial x} F_{22} + \frac{\partial N^I}{\partial y} F_{21} \end{bmatrix} \quad I = 1,\ 2,\ ...,\ nne, \tag{B.3}$$

where *nne* denotes the number of nodes in each element of the macro- or micro-domains and $\mathbf{F} = \partial \mathbf{u}/\partial \mathbf{x}$ is the deformation gradient tensor. The matrix $\mathbf{B}_0$ consists of the derivatives of shape functions and the deformation gradient which reflects the effect of deformation in the stiffness of the domain. In this context one can show that:

$$\frac{\partial \mathbf{f}^{int}}{\partial \mathbf{u}} = \mathbf{K} = \mathbf{K}_{mat} + \mathbf{K}_{geo}, \tag{B.4}$$

in which $\mathbf{K}_{mat}$ and $\mathbf{K}_{geo}$ are the so-called material and geometrical tangent matrices, respectively. The material stiffness matrix for an element is written as:

$$\mathbf{K}_{mat} = \int_{\Omega_e} \mathbf{B}_L^T \mathbf{C} \mathbf{B}_L d\Omega_e, \tag{B.5}$$

where $\mathbf{B}_L$ is the matrix containing shape functions derivatives, Ω_e denotes the domain occupied by the element and $\mathbf{C}$ denoted the material's stiffness (or elasticity matrix). For the Saint Venant-Kirchhoff material considered in this paper, this matrix has the form (in Voigt notation):

$$\mathbf{C} = \frac{\partial \mathbf{S}}{\partial \mathbf{E}} = \begin{bmatrix} \lambda + 2\mu & \lambda & 0 \\ \lambda & \lambda + 2\mu & 0 \\ 0 & 0 & 2\mu \end{bmatrix}. \tag{B.6}$$

In addition the geometric (nonlinear) stiffness of an element is written as:

$$\mathbf{K}_{geo} = \int_{\Omega_e} \mathbf{B}_{NL}^T \mathbf{S} \mathbf{B}_{NL} d\Omega_e \tag{B.7}$$

where $\mathbf{B}_{NL}$ is:

$$\mathbf{B}_{NL} = \begin{bmatrix} \mathbf{B}_{NL}^1 & \mathbf{B}_{NL}^2 & ... & \mathbf{B}_{NL}^{nne} \end{bmatrix}. \tag{B.8}$$

and where for each node $I = 1,\ 2\ ...\ nne$, we have:

$$\mathbf{B}_{NL}^I = \begin{bmatrix} \frac{\partial N^I}{\partial x}\frac{\partial u_x^I}{\partial x} & \frac{\partial N^I}{\partial x}\frac{\partial u_y^I}{\partial x} \\ \frac{\partial N^I}{\partial y}\frac{\partial u_x^I}{\partial y} & \frac{\partial N^I}{\partial y}\frac{\partial u_y^I}{\partial y} \\ \frac{\partial N^I}{\partial y}\frac{\partial u_x^I}{\partial x} + \frac{\partial N^I}{\partial x}\frac{\partial u_x^I}{\partial y} & \frac{\partial N^I}{\partial y}\frac{\partial u_y^I}{\partial x} + \frac{\partial N^I}{\partial x}\frac{\partial u_y^I}{\partial y} \end{bmatrix}, \tag{B.9}$$

where u_x^I and u_y^I denote the x and y components of deformation field at node I, respectively.